Development of Optical Diagnostics for Performance Evaluation of Arcjet Thrusters

Final Report

Grant # NAG3-1040
Covering the period 08/01/89 - 03/24/94
(no cost to 09/24/94)

Prepared for

Dr. Frank Curran, c/o
Ms. Lori Albergotti, MS 500-315
NASA Lewis Research Center
21000 Brookpark Road
Cleveland, OH 44135

Submitted by

Mark A. Cappelli, Principal Investigator

August, 1995

HIGH TEMPERATURE GASDYNAMICS LABORATORY
Mechanical Engineering Department
Stanford University

TABLE OF CONTENTS

1.0 EXECUTIVE SUMMARY

Laser and optical emission-based measurements have been developed and implemented for use on low-power hydrogen arcjet thrusters and xenon-propelled electric thrusters. In the case of low power hydrogen arcjets, these laser induce fluorescence measurements constitute the first complete set of data that characterize the velocity and temperature field of such a device. The research performed under the auspices of this NASA grant includes laser-based measurements of atomic hydrogen velocity and translational temperature, ultraviolet absorption measurements of ground state atomic hydrogen, Raman scattering measurements of the electronic ground state of molecular hydrogen, and optical emission based measurements of electronically excited atomic hydrogen, electron number density, and electron temperature. In addition, we have developed a collisional-radiative model of atomic hydrogen for use in conjunction with magnetohydrodynamic models to predict the plasma radiative spectrum, and near-electrode plasma models to better understand current transfer from the electrodes to the plasma. In the final year of the grant, a new program aimed at developing diagnostics for xenon plasma thrusters was initiated, and results on the use of diode lasers for interrogating Hall accelerator plasmas has been presented at recent conferences.

The research is presented in detail in a total of 32 full length technical papers, 10 of which are in peer-reviewed journals. All of these reference the support provided by NASA Lewis, either through this grant, or, through donated equipment.

2.0 PUBLICATIONS

The following is a brief synopsis of the publications included in the Appendices of this report. The reader is also referred to the complete list of publications stemming from the research funded under this grant presented in Section 2.4.

2.1 Near-Electrode Plasma Structure

The need to better understand the structure and stability of a diffuse arc attachment at the anode of an arcjet thruster spawned a modelling effort on our part which focuses on the problem of current transfer between an electrode and a near-thermal plasma. This research culminated into two publications. In the first publication, we formulated a model for the case of a multi-fluid, single temperature, flowing thermal plasma impinging onto a plane anode, and identified two operating modes that were strongly influenced by the free-stream conditions. In the second paper (Meeks and Cappelli, 1993, see Appendix A), we extended the model to account for finite electron-ion recombination kinetics at the anode, and for the case of a multi-fluid, two temperature free stream condition.

2.2 LIF Measurements of Temperature and Velocity

We have used laser induced fluorescence to excite the Balmer-alpha transition in atomic hydrogen at 656 nm. By tuning the narrow bandwidth output of an argon-ion pumped ring-dye laser across the n = 3 -> n = 2 transition multiplet, we were able to resolve the Doppler-broadened and Doppler shifted lineshape to extract both translational temperature and velocity. The diagnostic strategy and first results were presented in Liebeskind et al., 1993 (see Appendix B). In order to understand weather there is a significant slip between species comprising the flow in a hydrogen arcjet, LIF was performed on both atomic hydrogen and helium in a helium-seeded hydrogen arcjet. These results are presented in Liebeskind et al., 1995 (see also Appendix B). Finally, a comprehensive comparison of

the LIF data to MHD predictions of arcjet performance is presented in a paper co-authored by our laboratory, and engineers from Olin Aerospace Co., manufacturers of flight-qualified thrusters (Cappelli et al., 1995 in Appendix B).

2.3 Raman Scattering Measurements of Molecular Hydrogen

The Raman scattering diagnostic was motivated by the need to better understand performance limitations associated with frozen flow losses in arcjet thrusters. It provides the means of directly measuring the electronic ground state concentrations of molecular hydrogen. Measurements were performed for both cold-flow (see Boyd et al, Appendix C) and arc-heated flow conditions. In the cold-flow studies, experiments were in excellent agreement with the results of Monte Carlo simulations of Iain Boyd at Cornell University. Arc-heated flow studies were compared to both Monte Carlo and MHD predictions of the flow structure (see for example, AIAA 95-1956, Appendix C). The results support the conjecture that mass diffusion is an important transport mechanism which strongly influences the nozzle flow behavior.

2.4 Complete List of Publications

Peer-reviewed Publications

1. "The Non-Equilibrium Region of an Electrode in Contact with a Flowing Thermal Plasma," M.A. Cappelli, IEEE Trans. Plasma Sciences **21**, pp.194-201, 1993.

2. "Two-Temperature Fluid Model for High Pressure Plasmas in Contact with Cooled Electrodes," E. Meeks and M.A. Cappelli, J. Appl. Phys. **73**, pp. 3172-3182, 1993.

3. "LIF Diagnostic of Temperature and Velocity in a Hydrogen Arcjet," J.G. Liebeskind, R.K. Hanson, and M. A. Cappelli, Applied Optics **32**, pp.6117-6127, 1993.

4. "Numerical and Experimental Investigations of Low-Density Supersonic Jets of Hydrogen," I.D. Boyd, D.R. Beattie, and M.A. Cappelli, J. Fluid Mech. **280**, pp. 41-67, 1994.

5. "Experimental Investigation of Velocity Slip Near an Arcjet Exit Plane," J.G. Liebeskind, R.K. Hanson, and M.A. Cappelli, AIAA Journal **33**, pp. 373-375, 1995.

6. "Comparison of Hydrogen Arcjet Thruster Properties to Single-Fluid Model Predictions," M.A. Cappelli, J.G. Liebeskind, R.K. Hanson, G.W. Butler, and D.Q. King, submitted to Journal of Propulsion and Power, October, 1994.

7. "Interior Plasma Diagnostics of Arcjet Thrusters," M.A. Cappelli and P.V. Storm, Journal of Propulsion and Power, in press, 1995.

8. "Radiative Emission Analysis of an Expanding Hydrogen Arc Plasma I: Arc Region Diagnostics Through Axial Emission," P.V. Storm and M.A. Cappelli, submitted to JQSRT, 1995.

9. "Radiative Emission Analysis of an Expanding Hydrogen Arc Plasma II: Plume Region Diagnostics Through Radial Emission," P.V. Storm and M.A. Cappelli, submitted to JQSRT, 1995.

10. "Raman Scattering Measurements of Molecular Hydrogen in an Arc-Heated Flow," D.R. Beattie and M.A. Cappelli, submitted to Applied Optics.

Conference Papers

1. "Velocity Measurements in a Hydrogen Arcjet using LIF," J.G. Liebeskind, R.K. Hanson, and M.A. Cappelli, AIAA 91-2112, 27th Joint Propulsion Conference, June 24-26, Sacramento, California, 1991.

2. "Optical Diagnostics of a Low Power Hydrogen Arcjet," M.A. Cappelli, R.K. Hanson, J.G. Liebeskind, and D.H. Manzella, IEPC 91-091, 22nd International Electric Propulsion Conference, October 14-17, Viareggio, Italy, 1991.

3. "Laser-Induced Fluorescence of Atomic Hydrogen in an Arcjet Thruster," J.G. Liebeskind, R.K. Hanson, and M.A. Cappelli, AIAA 92-0678, 30th Aerospace Sciences Meeting, January 6-9, Reno, NV 1992.

4. "Vacuum Ultraviolet Absorption Measurements in a Hydrogen Arcjet," D.H. Manzella and M.A. Cappelli, AIAA 92-3564, 28th Joint Propulsion Conference, July 6-8, Nashville, TN, 1992.

5. "Modeling the Near-Electrode regions of Arcjets I: Coupling of the Flowfield to the Non-Equilibrium Boundary Layer," M.A. Cappelli, AIAA 92-3109, 28th Joint Propulsion Conference, July 6-8, Nashville, TN, 1992.

6. "Flow Diagnostics of an Arcjet Using Laser-Induced Fluorescence,", J.G. Liebeskind, R.K. Hanson, and M.A. Cappelli, AIAA 92-3243, 28th Joint Propulsion Conference, July 6-8, Nashville, TN, 1992.

7. "Molecular Hydrogen Raman Scattering in a Low Power Hydrogen Arcjet Thruster," D.R. Beattie and M.A. Cappelli, AIAA 92-3566, 28th Joint Propulsion Conference, July 6-8, Nashville, TN, 1992.

8. Predictions," M.A. Cappelli, J.G. Liebeskind, R.K. Hanson, G.W. Butler, and D.Q. King, AIAA 93-0820, 31st Aerospace Sciences Meeting, January 11-14, Reno, NV, 1993.

9. "Monte Carlo and Experimental Studies of Nozzle Flow in a Low Power Hydrogen Arcjet," I.D. Boyd, M.A. Cappelli, and D.R. Beattie, AIAA 93-2529, 29th Joint Propulsion Conference, June 28-30, Monterey, CA, 1993.

10. "Plume Characteristics of an Arcjet Thruster," J.G. Liebeskind, R.K. Hanson, and M.A. Cappelli, AIAA 93-2530, 29th Joint Propulsion Conference, June 28-30, Monterey, CA, 1993.

11. "Axial Emission Diagnostics of a Low Power Hydrogen Arcjet Thruster," P.V. Storm and M.A. Cappelli, IEPC-93-219, Proceedings of the 23rd International Electric Propulsion Conference, Seattle, WA, September 13-16, 1993.

12. "Chamber Effects on Plume Expansion for a Low- Power Hydrogen Arcjet," I.D. Boyd, D.R. Beattie, and M.A. Cappelli, IEPC-93-126, Proceedings of the 23rd International Electric Propulsion Conference, Seattle, WA, September 13-16, 1993.

13. "A Direct Comparison of Hydrogen Arcjet Thruster Properties to Model Predictions," M.A. Cappelli, J.G. Liebeskind, R.K. Hanson, W.G. Butler, and D.Q. King, Proceedings of the IEPC-93-220, 23rd International Electric Propulsion Conference, Seattle, WA, September 13-16, 1993.

14. "LIF Measurements of Species Velocities in an Arcjet Plume," J.G. Liebeskind, R.K. Hanson, and M.A. Cappelli, IEPC-93-131, Proceedings of the 23rd International Electric Propulsion Conference, Seattle, WA, September 13-16, 1993.

15. "Interior Plasma Diagnostics of Arcjet Thrusters," M.A. Cappelli and P.V. Storm , AIAA-94-2654, 25th AIAA Plasmadynamics and Lasers Conference, Colorado Springs, CO, June 20-23, 1994.

16. "Semiconductor Laser Diagnostics Development for Xenon Plasmas," R.J. Cedolin, R.K. Hanson, and M.A. Cappelli, AIAA 94-2739, 30th Joint Propulsion Conference, Indianapolis, IN, June 27-29, 1994.

17. "Axial Emission Measurements on a Medium Power Hydrogen Arcjet Thruster," P.V. Storm and M.A. Cappelli, AIAA 94-2743, 30th Joint Propulsion Conference, Indianapolis, IN, June 27-29, 1994.

18. "Spectral Imaging of the Arcjet Electrode Region," D. Berns, P.V. Storm, and M.A. Cappelli, AIAA-95-1957, 26th AIAA Plasmadynamics and Lasers Conference, San Diego, CA, June 19-23, 1995.

19. "High Spectral Resolution Emission Study of a Low Power Hydrogen Arcjet Plume," P.V. Storm and M.A. Cappelli, AIAA-95-1960, 26th AIAA Plasmadynamics and Lasers Conference, San Diego, CA, June 19-23, 1995.

20. "Raman Scattering Measurements of Molecular Hydrogen in an Arcjet Thruster Plume," D.R. Beattie and M.A. Cappelli, AIAA-95-1956, 26th AIAA Plasmadynamics and Lasers Conference, San Diego, CA, June 19-23, 1995.

21. "Laser-Induced Fluorescence Measurements within an Arcjet Thruster Nozzle," P.V. Storm and M.A. Cappelli, AIAA-95-2381, 31st AIAA Joint Propulsion Conference, San Diego, CA, July 10-12, 1995.

22. "Pressure Measurements in the Plume of a Low power Arcjet Nozzle," W. Hargus Jr. and M.A. Cappelli, AIAA-95-2818, 31st AIAA Joint Propulsion Conference, San Diego, CA, July 10-12, 1995.

3.0 GRADUATES STUDENTS FUNDED UNDER THIS GRANT

John Liebeskind, "Temperature and Velocity Diagnostic for an Arcjet Plume Using Laser Induced Fluorescence." Ph.D. April, 1994.

Douglas Beattie, "Raman Scattering Measurements of Molecular Hydrogen in an Arcjet Thruster Plume." Ph. D. April, 1995.

Renato Cedolin, "Laser Diagnostics for Xenon Thrusters." Ph.D. expected 1996.

David Manzella, "Laser and Emission Spectroscopy of Hall Accelerator Plumes." Ph.D. expected 1996.

APPENDIX A

Page Intentionally Left Blank

NIS

Two-temperature fluid model for high-pressure plasmas in contact with cooled electrodes

E. Meeks
Sandia National Laboratories, Livermore, California 945551-0969, and Department of Mechanical Engineering, Stanford University, Stanford, California 94305

M. A. Cappelli
Department of Mechanical Engineering, Stanford University, Stanford, California 94305

(Received 3 August 1992; accepted for publication 11 December 1992)

A detailed continuum model of a weakly ionized plasma in stagnation flow against an electrically biased surface is presented. The model includes bulk fluid motion as well as electron and ion momentum and continuity equations in both general and quasineutral formulations. The inclusion of both electron and bulk energy equations allows for the determination of electron temperature and deviations from local thermodynamic equilibrium. Results for the quasineutral model demonstrate the importance of considering thermal nonequilibrium in the evaluation of plasma properties in the presheath region. The evaluation of transport properties is self-consistent with properties for the charged species depending on the calculated electric field and neutral number density. In addition to investigating thermal boundary layer and fluid flow effects, a finite electron-ion recombination rate at the electrode surface is employed and the consequences of varying this boundary condition are explored.

I. INTRODUCTION

The widespread use of plasma enhancement in materials processing has sparked new interest in the development of both glow-discharge and arc-jet plasma models. With few exceptions, most existing plasma models describe quiescent systems with uniform or decoupled bulk (neutral) properties. In many plasma-processing reactors, however, ionized gases impinge against cooled substrates in a stagnation-point flow geometry. In such cases, there may be significant coupling between fluid-dynamic and thermal boundary-layer development, plasma electrical properties, and chemical kinetics. Unraveling these complex interactions is essential to understanding and predicting the effects of plasma enhancement and electrical biasing of substrates. This article outlines the theoretical treatment of a weakly ionized, chemically reacting plasma in stagnation flow against a cooled, electrically biased substrate. The equations are then solved for a simplified case of a quasineutral argon plasma, to explore the effects of thermal and fluid boundary layers on plasma properties in the presheath region.

Over the past 30 years there has been much work on the analysis and characterization of plasma systems with a variety of applications considered. Early studies were primarily concerned with the interaction of diagnostic probes and the plasma surrounding them (see, for example, Refs. 1–5). Continuum probe models have usually focused on predicting current-voltage characteristics and have been reviewed by Chung, Talbot, and Touryan.[6] Interest in arc modes and arc jet operation has also generated much work in plasma modeling near electrode surfaces.[7–10] These models are directed toward understanding the principles behind diffuse and constricted arc modes and in predicting the potential fall in the vicinity of electrodes. Magnetohydrodynamic (MHD) generators are often analyzed in a similar manner with further attention to current-voltage characteristics and the effect of hydrodynamic boundary layers on plasma properties.[5,11,12] Numerous models have emerged recently to describe dc and rf glow discharges. These models attempt to capture the characteristics of a self-sustained plasma, predict voltage drops near the electrodes, and provide insight into various modes of discharge behavior.[11,13–18] While most models of plasma chemistry are limited to ionization and excitation reactions,[8,12,17,19,20] Kushner[21] presented results for a quiescent, radio-frequency etching plasma that included an extensive chemical kinetic mechanism. We combine many of the physical details that have been introduced through these previous analyses to describe a comprehensive, consistent theory for a fluid continuum plasma in contact with a reactive electrode. In addition, we draw upon prior theoretical work in the area of neutral chemical-vapor-deposition modeling (see, for example, Refs. 22–28) which provides the groundwork for inclusion of multiple species in reacting, fluid systems.

Among the many features common to the broad spectrum of plasma analyses, it is generally recognized that the plasma region close to an electrode can be subdivided into several overlapping subregions in which different processes dominate. In particular, there usually exists[12] (a) an outer, quasineutral region in which net space charge is negligible but bulk properties such as velocity, temperature, number densities, and species fluxes may change significantly; (b) a sheath of length on the order of the plasma Debye length, where space charge dominates; and (c) a Knudsen sublayer of thickness on the order of the electron or ion mean

 0021-8979/93/073172-11$06.00

free path, where continuum assumptions are no longer strictly valid. Several self-consistent models are reported that include the plasma sheath[15,16,18,19,20,29–32] with coupling of electric-field and space-charge effects. The quasineutral analysis presented here accounts for detailed nonequilibrium processes within the presheath region (a). This model can later be expanded to include solution of Poisson's equation throughout the domain, coupling the space-charge-dominated sheath with presheath process interactions.

One important drawback of previous plasma analyses is the almost exclusive use of a perfectly absorbing electrode boundary condition on the ions and electron number densities. The use of this boundary condition often introduces singularities causing numerical difficulties[6,12] and imposing unrealistic constraints on the bulk plasma behavior. Even for a highly catalytic surface, a more appropriate condition would be a very high rate of recombination at the electrode, rather than a zero-density condition. Chung provided some guidance in evaluating the effect of electron emission at an electrode,[33] but still maintained that the electrode is first perfectly absorbing. Graves[17] recently employed a unity sticking coefficient, which provides a more appropriate formula for a surface with a high probability of recombination. In this work we include a finite reaction rate for electron-ion recombination and treat the rate coefficient as a variable parameter.

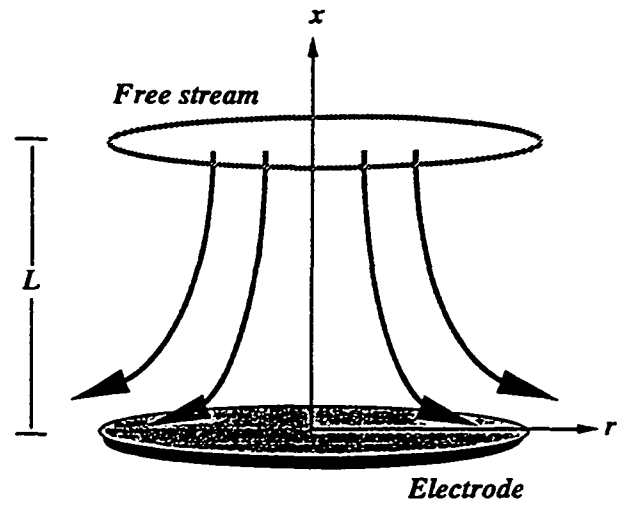

FIG. 1. Schematic of stagnation-flow geometry.

II. MODEL FORMULATION

A. Governing equations

The following governing equations provide a complete self-consistent formulation for a weakly ionized, continuum plasma in stagnation-point flow against an electrically biased substrate. Our numerical model includes solution of fully coupled electron and neutral energy equations. In addition we calculate net electron production rates by electron-impact ionization and electron third-body recombination with electron-temperature dependence. We derive the continuum equations by taking moments of the Boltzmann equation and applying a stagnation-point flow similarity transformation to obtain the final one-dimensional set of continuity, momentum, and energy equations for both individual species and the bulk. The stagnation-flow geometry is illustrated in Fig. 1. Further assumptions include thermalization between positive ions and neutral species and the application of Chapman–Enskog theory[34] for determination of neutral transport properties. Transport properties of charged species derive from swarm data for drift velocities as functions of E/n, where E is the calculated electric field, and n the neutral number density. The assumption of a quasineutral plasma then reduces the number of equations for the simplified calculation presented in Sec. III.

Equations (1)–(6) below describe the bulk fluid motion with nonuniform temperature and pressure:

$$\frac{1}{\rho}\frac{\partial \rho}{\partial t}+\frac{\partial u}{\partial x}+2V+\frac{u}{\rho}\frac{\partial \rho}{\partial x}=0, \tag{1}$$

$$\rho\frac{\partial V}{\partial t}-\frac{\partial}{\partial x}\left(\eta\frac{\partial V}{\partial x}\right)+\rho u\frac{\partial V}{\partial x}+\rho V^2+\Lambda=0, \tag{2}$$

$$\rho\frac{\partial u}{\partial t}+\rho u\frac{\partial u}{\partial x}-2\eta\frac{\partial V}{\partial x}-\frac{\partial}{\partial x}\left(\frac{4}{3}\eta\frac{\partial u}{\partial x}\right)+\frac{\partial}{\partial x}\left(\frac{4}{3}\eta V\right)+\frac{\partial P}{\partial x}=0, \tag{3}$$

$$P=\sum_{\substack{k=1\\k\neq e}}^{K_t} n_k k_B T+n_e k_B T_e, \quad \rho=\sum_{k=1}^{K_t} m_k n_k, \tag{4}$$

$$\Lambda\equiv=\frac{1}{r}\frac{\partial P}{\partial r}=\text{const}, \tag{5}$$

$$\rho c_p\frac{\partial T}{\partial t}+\rho u c_p\frac{\partial T}{\partial x}+\sum_{\substack{k=1\\k\neq e}}^{K_t} c_{pk} m_k\Gamma_k\frac{\partial T}{\partial x}+\sum_{\substack{k=1\\k\neq e}}^{K_t} m_k h_k\dot{n}_k-\frac{\partial}{\partial x}\left(\lambda\frac{\partial T}{\partial x}\right)-u\frac{\partial}{\partial x}(P-n_e k_B T_e)-\sum_{i=1}^{K_i} Z_i e\Gamma_i E-3k_B n_e(T_e-T)\sum_h\frac{m_e}{m_h}\overline{\nu_{eh}}-\dot{R}_{\text{inel}}-\frac{5}{2}k_B\dot{n}_e(T_e-T)=0. \tag{6}$$

These equations can be derived either from Navier–Stokes relations or from the summation of species conservation equations as derived from moments of the Boltzmann equation. In either case, a similarity transformation has been introduced for the stagnation-flow geometry. This transformation begins with the assumption of axisymmetry, where u and v are the mean-mass axial and radial velocities. Instead of the traditional stagnation flow formulation[35] in which a potential-flow solution determines the

pressure-gradient term in the radial momentum equation, we employ the finite-domain transformation described by Kee *et al.*[36] This method introduces a stream function of the form $\psi(x,r)=U(x)r^2$, which exactly satisfies mass continuity. In neglecting edge effects, we assume that the radii of the substrate surface and flow inlet are infinitely large. Substituting the stream function into the axial and radial momentum equations results in a constant radial pressure gradient as indicated by Eq. (5). Also we note that $u=2U/\rho$ and we can define $V\equiv(1/\rho)dU/dx=v/r$, where ρ is the mixture mass density. In an ideal stagnation flow, temperature and concentration gradients occur only in the axial direction, precluding density variations in the radial direction. The dependent variables ρ, u, and V are therefore only functions of the axial coordinate x. For convenience we choose to solve the continuity equation (1) along with the radial and axial momentum equations (2) and (3), rather than maintaining the stream-function notation. In the equations below, η is the mixture viscosity. The average thermodynamic pressure P is assumed to be much larger than the radial contribution $\Lambda r^2/2$. The ideal gas law (4) relates pressure to density and temperature, with k_B denoting the Boltzmann constant. Here n_k is the number density and m_k is the molecular mass of species k. The subscript e depicts electrons while i depicts electropositive ions. There are a total of K_t species including electrons and K_i positive ions. Although we are interested in the steady-state solution, we include transient terms in each equation to facilitate the description of time-stepping techniques in our numerical solution scheme.

Equation (6) describes the bulk energy equation where neutrals and ions are in thermal equilibrium and their temperature is a function of the axial coordinate only. It is important to note that the bulk energy equation represents the summation of species energy equations over all species except electrons, which are allowed to depart from thermal equilibrium. The energy equation includes convection, diffusion, production, conduction, flow work, and Joule heating terms. The last three terms describe energy gain due to elastic and inelastic collisions with electrons, followed by an electron production term. These three terms appear in the bulk energy equation due to the separate treatment of the electron energy and are described in more detail below. If the electrons were equilibrated at the bulk temperature T, and the electron energy equation added to Eq. (6), these terms would no longer appear in the bulk energy equation. In the ion Joule-heating term, the product $Z_i e$ is the charge of the ith electropositive ion, where $-e$ denotes the charge of an electron. Also, h_k is the specific enthalpy of species k, c_{pk} is the species' constant-pressure specific heat, and $\dot{n}_k$ is the net species' production rate. c_p represents the mixture-averaged specific heat, while λ is the bulk thermal conductivity.

Equations (7) and (8) describe continuity and conservation of momentum, respectively, for individual species within the plasma bulk:

$$\frac{\partial n_k}{\partial t}+\frac{\partial}{\partial x}(n_k u+\Gamma_k)+2Vn_k-\dot{n}_k=0, \quad k=1,\ldots,K_t, \tag{7}$$

$$\Gamma_k=\frac{\rho}{\bar{m}^2}\sum_{j\neq k}^{K_t} m_j D_k d_j-\frac{D_k^T}{m_k}\frac{1}{T}\frac{dT}{dx}, \quad k=1,\ldots,K_t,\ k\neq e \text{ or } i, \tag{8a}$$

$$\frac{\partial}{\partial t}(\Gamma_i+n_i u)+\frac{k_B}{m_i}\frac{\partial}{\partial x}(n_i T)+\left(u\frac{\partial \Gamma_i}{\partial x}+n_i u\frac{\partial u}{\partial x}+2\Gamma_i\frac{\partial u}{\partial x}+2V\Gamma_i\right)-\left(n_i Z_i\frac{e}{m_i}E+\Gamma_i\overline{\nu_{iN}}\right)=0, \quad i=1,\ldots,K_i, \tag{8b}$$

$$\frac{\partial}{\partial t}(\Gamma_e+n_e u)+\frac{k_B}{m_e}\frac{\partial}{\partial x}(n_e T_e)+\left(u\frac{\partial \Gamma_e}{\partial x}+n_e u\frac{\partial u}{\partial x}+2\Gamma_e\frac{\partial u}{\partial x}+2V\Gamma_e\right)+\left(n_e\frac{e}{m_e}E+\Gamma_e\overline{\nu_{eH}}\right)=0, \tag{8c}$$

$$\frac{dE}{dx}=\frac{e}{\epsilon_0}\left(\sum_{i=1}^{K_i} n_i-n_e\right) \tag{9}$$

Again, the similarity transformation results appear in the bulk convection terms. We have introduced the variable Γ_k to describe the diffusive flux of species k, where $\Gamma_k\equiv n_k U_k$ and U_k is diffusion velocity. Equation (9) represents Poisson's equation, relating the electric field gradient to the local net space charge. Here ϵ_0 is the free-space permittivity. We can relate the total current density J to the ion and electron fluxes, as follows:

$$J=e\left(\sum_{i=1}^{K_i} Z_i\Gamma_i-\Gamma_e\right)+eu\left(\sum_{i=1}^{K_i} Z_i n_i-n_e\right).$$

For neutral species the general form of the diffusive fluxes result from a multicomponent formulation including thermal diffusion as shown in Eq. (8a).[34] Here d_j is the concentration gradient with respect to x. D_{kj} is the ordinary diffusion coefficient while D_k^T is the thermal diffusion coefficient. The mean molecular mass of the mixture is given by $\bar{m}$. We note that Eq. (8a) is an explicit relation that could be substituted directly into Eq. (7) for the neutral species. However, we choose to keep Γ_k as a separate dependent variable for consistency with the treatment of ions and electrons. For ions and electrons, the full species momentum equations must be solved as indicated by Eq. (8b) for ions and Eq. (8c) for electrons. The ion and electron momentum equations include balance between forces due to pressure, inertia, and electric field as well as momentum loss due to collisions with other species. Viscous forces on electrons and ions are neglected. For the ions, we assume that charge-neutral collisions dominate momentum transfer, consistent with the assumption of a weakly ionized plasma. The parameter $\overline{\nu_{iN}}$ represents the momentum-averaged momentum-transfer collision frequency summed over all neutral species. For electrons, we consider all heavy species (i.e., all species besides electrons) and introduce the parameter $\overline{\nu_{eH}}=\Sigma_h\overline{\nu_{eh}}$ to repre-

sent the momentum-averaged momentum-transfer collision frequency summed over all heavy species. The collision frequencies are derived from swarm data for drift velocities with electric-field dependence, as further discussed below.

Equation (10) is the electron energy equation in which $\frac{3}{2}k_B T_e$ represents the average energy of an electron:

$$\frac{3}{2}n_e k_B \frac{\partial T_e}{\partial t} - k_B T_e \frac{\partial n_e}{\partial t} + \frac{3}{2}n_e k_B u \frac{\partial T_e}{\partial x} - u k_B T_e \frac{\partial n_e}{\partial x} + \Gamma_e \frac{\partial}{\partial x}\left(\frac{5}{2}k_B T_e + \frac{u^2}{2}\right) - \frac{\partial}{\partial x}\left(\lambda_e \frac{\partial T_e}{\partial x}\right) + e\Gamma_e E + 3k_B n_e (T_e - T)\sum_h \frac{m_e}{m_h}\overline{\nu_{eh}} + \dot{R}_{\text{inel}} + \frac{5}{2}k_B \dot{n}_e (T_e - T) = 0. \quad (10)$$

We neglect all thermal diffusion effects on the electron energy. The steady-state equation includes convective terms, diffusion, conduction, Joule heating, energy loss due to both elastic and inelastic collisions, and a production term. From left- to right-hand sides, the first two terms in Eq. (10) are transient, followed by two terms which represent a combination of convection and flow work analogous to the second and sixth terms in the bulk energy equation (6). The next term represents diffusion of electron enthalpy analogous to the third term in Eq. (6), followed by a conduction term. Next is the electron Joule-heating contribution representing the increase in electron energy due to work by the electric field. Coupling the electron energy equation to the bulk energy equation, the next term represents the transfer of energy between electrons and heavy species through elastic collisions. Inelastic collision losses result from energy lost by electrons participating in electron third-body reactions, and take the form $\dot{R}_{\text{inel}} = \Sigma_r q_r \Delta H_r$, where q_r is the rate of progress of the rth electron third-body reaction, and ΔH_r is the heat of reaction. A positive sign for ΔH_r indicates that the reaction is endothermic in its forward direction. Finally, the production term can be interpreted as the energy loss to the electron swarm required to thermalize electrons produced through ionization of neutral species. The electron equation is included here in its most general form, although some terms may prove to be insignificant under the conditions considered below.

B. Quasineutral assumptions

We now modify the set of governing equations for the case of a quasineutral plasma,[6] neglecting space-charge effects in the thin-sheath limit:

$$n_e - \sum_{i=1}^{K_i} Z_i n_i = 0, \quad (11)$$

$$\Gamma_e + \frac{J}{e} - \sum_{i=1}^{K_i} Z_i \Gamma_i = 0, \quad (12)$$

$$\frac{J}{e}\left(2\frac{du}{dx} + 2V + \overline{\nu_{eH}}\right) - \sum_{i=1}^{K_i}\left(Z_i \frac{k_B}{m_e}\frac{d}{dx}(n_i T_e) + Z_i \frac{e}{m_e} n_i E - Z_i \Gamma_i \overline{\nu_{eH}}\right) = 0. \quad (13)$$

This approach allows us to investigate thermal nonequilibrium in the presheath region of a flowing plasma. Solution of the full set of equations described above can later be used to evaluate additional interactions within the sheath. The fundamental assumption of the quasineutral formulation is that, throughout the region of interest, the local net charge is approximately zero. To this end, the electron continuity equation is replaced by the charge balance condition given by Eq. (11). In addition we assume that the production rate of electrons is always balanced by the production of ions with $\dot{n}_e = \Sigma_i Z_i \dot{n}_i$, and that the gradient of the electron number density is balanced by gradients of ions, such that $dn_e/dx = \Sigma_i Z_i (dn_i/dx)$. These assumptions result in a constant total current density J. We therefore replace the electron momentum equation (8c) with the consequent quasineutral relation (12). Finally, in order to solve for the ambipolar electric field, we subtract Eq. (8c) from the sum of the ion momentum Eq. (8b) weighted by the integer charge Z_i of each ion. The result is Eq. (13) which replaces Poisson's equation (9). We now have ten equations with ten unknowns: $u(x)$, $V(x)$, $P(x)$, $T(x)$, $\rho(x)$, Λ, $n_k(x)$, $\Gamma_k(x)$, $E(x)$, and $T_e(x)$, with Γ_k and n_k representing unknowns for each species (neutral, ion or electron).

C. Boundary conditions

Solution of the above set of equations requires boundary conditions both at the reactor inlet and at the electrode surface. At the inlet ($x = L$) we specify the freestream conditions with $u(L) = u_\infty$, $V(L) = 0$, $P(L) = P_\infty$, $T(L) = T_\infty$, $n_k(L) = n_{k\infty}$, and $T_e = T_{e\infty}$. For the results presented here, we additionally let $T_{e\infty} = T_\infty$ and set the inlet species concentrations to their equilibrium values at that temperature, although this is not required for solution of the equations.

At the electrode, the conditions are more complex. The radial velocity obeys the no-slip condition at the surface, with $V(0) = 0$. The inclusion of heterogeneous reactions that may result in a net deposit on the wall as well as a net current into or out of the wall results in a nonzero value for $u(0)$. The bulk velocity condition at the electrode becomes

$$u(0) = \frac{1}{\rho}\left(\sum_{k=1}^{K_t} \dot{s}_k m_k - \frac{J}{e} m_e\right),$$

where $\dot{s}_k$ is the net production rate of species k through heterogeneous reaction. We assume that the neutrals and ions thermally equilibrate with the electrode such that $T(0) = T_w$ and T_w is held constant. The electrons, how-

TABLE I. Electron and ion transport properties.

Symbol	Transport property	Formula
$\overline{\nu_{eh}}$	electron momentum-transfer collision frequency with species h	$\overline{\nu_{eh}}=eE/m_e w_{eh}$
D_{eh}	binary electron diffusion coefficient in heavy species h	$D_{eh}=k_B T_e/m_e\overline{\nu_{eh}}$
λ_e	electron thermal conductivity	$\lambda_e \simeq 2.4\dfrac{k_B^2 n_e T_e}{m_e \overline{\nu_{eH}}}$
$\overline{\nu_{in}}$	ion momentum-transfer collision frequency with species n	$\overline{\nu_{in}}=\dfrac{eE}{m_{in} w_{in}}, \quad m_{in}\equiv\dfrac{m_i m_n}{m_i+m_n}$
$\overline{\nu_{iN}}$	ion momentum-averaged collision frequency	$\overline{\nu_{iN}}=\int_n \overline{\nu_{in}}\left(\dfrac{2m_n}{m_i+m_n}\right)$
D_{in}	binary ion diffusion coefficient in neutral species n	$D_{in}=k_B T/m_i\overline{\nu_{in}}$
λ_i	ion thermal conductivity	$\lambda_i=\left(\dfrac{9\gamma_i-5}{\gamma_i-1}\right)k_B^2 T\dfrac{n_i}{m_i\overline{\nu_{iN}}}, \quad \gamma_i\equiv\dfrac{c_{pi}}{c_{vi}}$
η_i	ion viscosity	$\eta_i=4k_B T n/\pi\overline{\nu_{iN}}$

ever, may be sufficiently energetic to remain out of equilibrium at the electrode surface. The boundary condition on the electron energy is therefore a balance between enthalpy loss from net current flow into the surface, net destruction of electrons through surface recombination, conduction due to electron temperature gradient, and flow work. This relation is stated as

$$h_e\left(\frac{J}{e}-\dot{s}_e\right)-\lambda_e\left.\frac{dT_e}{dx}\right|_{x=0}-(un_e k_B T_e)|_{x=0}=0.$$

The boundary condition on species fluxes must also balance production rates of species through surface reaction. With a net current J specified in the electrically biased case, the electron, ion, and neutral flux conditions are as follows:

$$\Gamma_e(0)=\dot{s}_e-(J/e)-n_e u|_{x=0},$$

$$\Gamma_i(0)=\dot{s}_i-n_i u|_{x=0}, \quad i=1,\ldots,K_i,$$

$$\Gamma_k(0)=\dot{s}_k-n_k u|_{x=0}, \quad k=1,\ldots,K_n, \; k\neq e \text{ or } i.$$

Here we also require that $\dot{s}_e=\Sigma_{i=1}^{K_i} Z_i \dot{s}_i$ and assume that only electrons carry current into or out of the electrode. This completes the boundary-condition requirements for a well-posed set of governing equations.

D. Numerical solution

Through finite-difference approximations, we discretize the set of differential equations over a one-dimensional computational grid which spans the distance between the electrode and the inlet or freestream at $x=L$. Solution of the resulting algebraic equations employs a damped, modified Newton algorithm designed for boundary-value problems.[37] This numerical scheme, as first applied to premixed flame modeling,[38] has proven to be a successful method for convergence of stiff, nonlinear systems of equations. Solution begins on a coarse mesh with trial guesses for the dependent variables. The coarse-mesh solutions then provide the initial guess for adaptively refined grids, until the solution achieves the desired accuracy. In the event that the Newton algorithm fails to converge, a series of time integrations proceed from the trial estimate to gradually approach the steady-state solution. Since a successful Newton iteration is much faster than the time-integration procedure, time stepping only conditions the trial estimate until it is sufficiently good for the Newton iteration to converge. The implementation of our numerical scheme and the overall program structure derives from the neutral-gas stagnation-flow software documented as the Sandia computer code SPIN.[26]

E. Incorporation of transport properties and chemical production terms

In our general formulation for a reacting multispecies flow, we require transport properties for neutral species including thermal conductivity, diffusion coefficients, and mixture viscosity. Calculation of these properties employs a modified version of the Sandia transport package.[22] For interactions between neutral species, properties derive from standard kinetic theory where collision integrals are based on Stockmayer potentials using a Maxwellian neutral temperature and Leonard–Jones potential well depths.[39] To determine collision frequencies for charged species, this method is no longer valid and we must include electric-field dependence. In an effort designed to be parallel and analogous to the Sandia transport approach, we include the generalized capability of incorporating electron and ion transport dependence on electric field in a coupled manner. This is achieved by first mathematically fitting measured or calculated swarm parameters in the form of drift velocity, w_{ek} vs E/n_k for each charge-neutral species pair. We then access this information during numerical iteration for local values of E/n_k. The drift velocity w_{ek} determined from swarm data is the velocity at which electrons (or ions) diffuse through a uniform medium in the presence of an applied electric field. This velocity is directly related to the momentum-averaged collision frequency between electrons and the background gas for a particular value of E/n_k, as indicated in Table I. The total momentum-average collision frequency for electrons is determined by summing over all heavy species, while ion collision frequencies are summed over all neutral species. Charged species' transport properties are then determined from $\overline{\nu_{eH}}$ or $\overline{\nu_{iN}}$ as shown in Table I.[40]

Similarly, for inclusion of neutral and charged-species chemical production terms, we employ a modified version of the Sandia subroutine package CHEMKIN.[24,25] Here, assumption of Maxwellian distribution functions for neutral species allows the use of temperature-dependent rate formulas for chemical reactions that involve neutral species only. In general, electron reactions such as electron-impact ionization or electron-impact dissociation could be treated in a similar manner to electron and ion transport described above. In this case, ionization, dissociation, or recombination rate coefficients as functions of E/n could be employed. Alternatively, reaction cross sections as functions of electron energy could be integrated over an electron distribution function determined by a local field approximation. For the high-pressure conditions considered here, however, we assume that the isotropic part of the local electron distribution is close to a Maxwellian function of T_e. In this way, rates for reactions that involve electron impact depend only on the local electron temperature and species concentrations. Also, the assumption of a near-Maxwellian electron temperature simplifies the use of detailed balancing in determining reverse reaction rates. Finally, use of the Sandia Surface CHEMKIN package facilitates incorporation of finite-rate chemistry at the electrode.[28]

III. RESULTS AND DISCUSSION

For purposes of comparison, we begin by analyzing plasma conditions typical of arc-jet operation with stagnation flow against a perfectly catalytic electrode. We choose plasma free-stream conditions to be argon gas in local thermodynamic equilibrium (LTE) at 6000 K and 1 atm. In addition, we specify a free-stream velocity of $u_\infty = 570$ cm/s at a distance of 5 cm above the electrode. Approximating the perfectly catalytic condition requires a very high rate for electron-ion recombination, since we maintain a finite-rate formulation. To achieve this condition, we choose a recombination rate such that the electron generation rate, mole fraction, and flux behavior compare well with analyses that employ zero electron density at the electrode. To compare with analysis by Cappelli,[9] we employ a reaction rate coefficient of approximately 10^{15} cm^4/s mol for the recombination reaction

$$Ar^+ + e \Rightarrow Ar$$

occurring at the electrode surface. The effects of reducing this reaction rate to a more realistic value are discussed later in this section. In the gas phase, we allow both ionization and recombination through electron third-body impact. Thus, for the reaction stated as

$$Ar^+ + e + e \Leftrightarrow Ar + e,$$

we employ a forward reaction rate from Hinnov and Hirshberg,[41] with

$$k_f = 3.959 \times 10^{39} T_e^{-9/2} \text{ cm}^6/\text{s mol}^2,$$

and the reverse rate derived from detailed balancing becomes

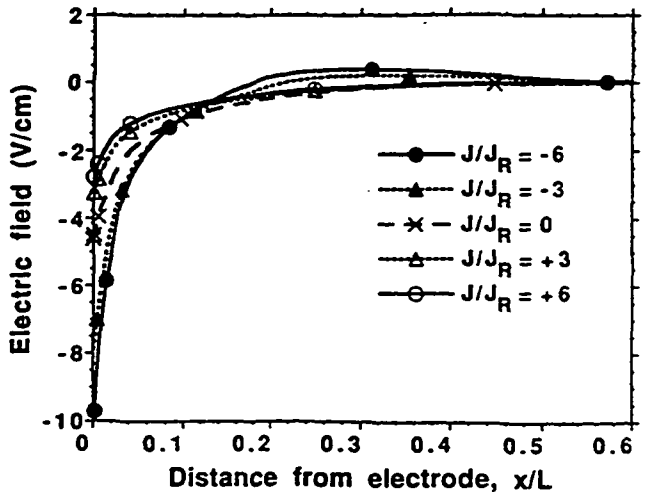

FIG. 2. Spatially varying electric field for various current values and uniform neutral temperature case.

$$k_r = 1.906 \times 10^{32} T_e^{-3} \exp\left(\frac{-183\,285}{T_e}\right) \text{ cm}^3/\text{s mol}.$$

For the results presented here, we consider no other chemical reactions in either the gas or at the surface.

We consider the three cases of electrode operation: unbiased or floating ($J=0$), anode ($J>0$) and cathode ($J<0$). It is convenient to introduce a reference value for the electrode current density for scaling purposes. We therefore let $J_R \equiv n_{e\infty}(\mu_e+\mu_i)(k_B T_{e\infty}/l_R)$, where l_R is the approximate recombination length at the inlet conditions, while μ_e and μ_i are characteristic values of the electron and ion mobilities at the inlet.[9] For the conditions described above, we use $\mu_e = 0.6$ m^2/V s, $\mu_i = 0.002$ m^2/V s, and arrive at a value of approximately 6.5 mm for l_R and 230 A/m^2 for J_R. Also, since we use the electrode current as a boundary condition, we implicitly assume that, in the case of $J<0$, the cathode is capable of providing the specified current. Here we are only interested in the effect of the net current on the plasma behavior. If we instead specified a fixed material for our electrode, we would have to restrict cathode currents to those consistent with the material work function at the specified electrode temperature.

A. Uniform neutral temperature case

If we first neglect the thermal boundary layer and set $T_w/T_\infty = 1.0$, the results of our stagnation flow analysis are as shown in Figs. 2 and 3. These results underline the importance of including a separate electron energy equation when a net current passes through the electrode, especially in the cathode case. In all cases, a sharp electrical boundary layer develops due to ambipolar diffusion, as illustrated in Fig. 2, even in the unbiased case. The magnitude of this presheath electric field is largely determined by the electron-ion recombination boundary condition, as further discussed below. Figure 3 shows the importance of electron temperature in determining electron and ion behavior. In the cathode case ($J<0$), electrons diffuse with the electric field and are thereby energized through Joule

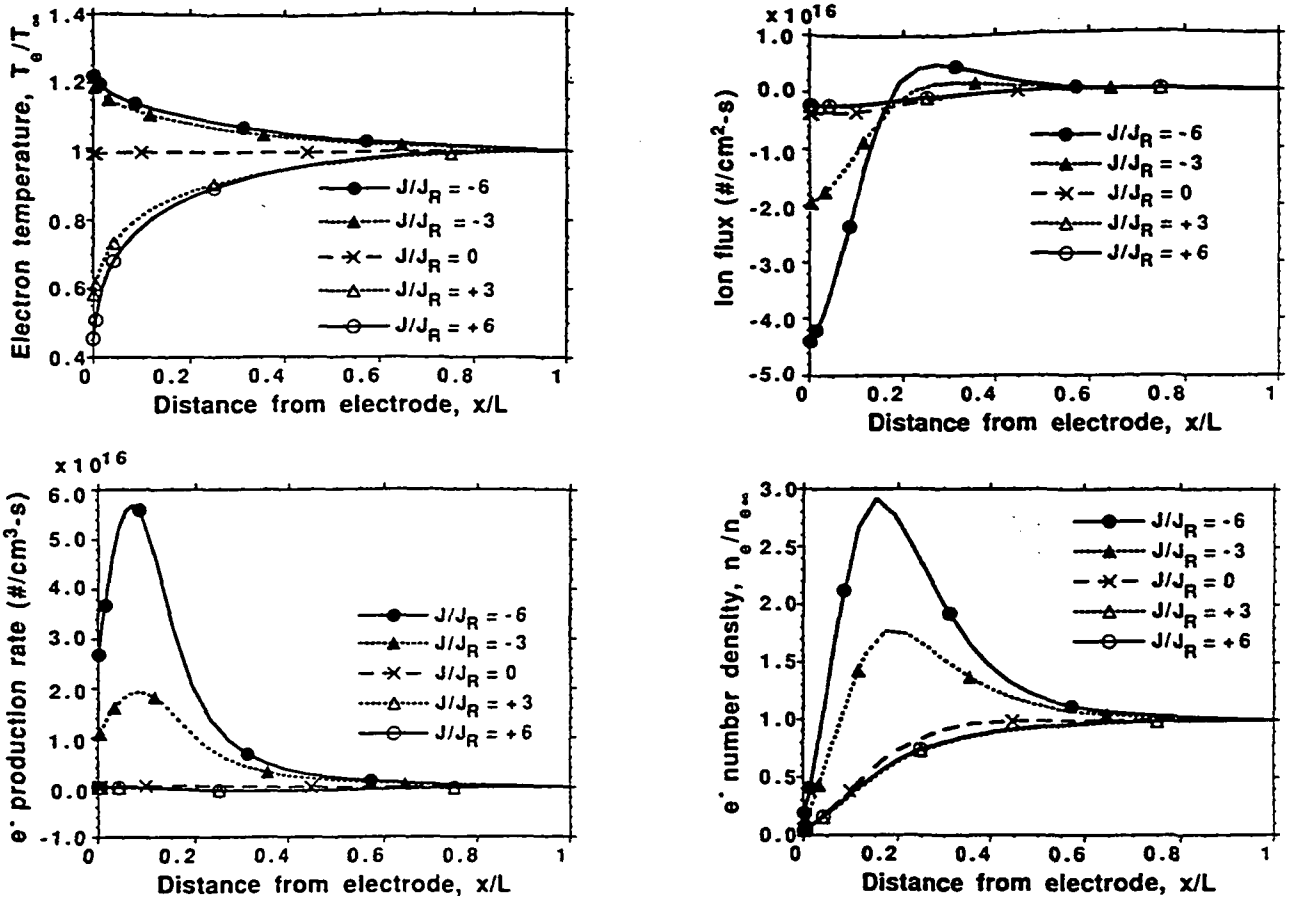

FIG. 3. Effect of varying current on plasma properties for uniform neutral temperature case.

heating. In the anode case, however, electrons diffuse against the field and thereby lose energy through diffusion cooling. In either case, the presence of the electrode causes the electron temperature to depart significantly from equilibrium with the neutral/ion temperature, even when neglecting the neutral thermal boundary layer.

The importance of thermal nonequilibrium is apparent in Figs. 3(b), 3(c), and 3(d). For the cathode case, the elevated electron temperature causes the plasma to ionize further and results in a source of electrons and ions near the surface. This source causes the ions to reverse direction midstream such that ions diffuse away from the generation location, despite the negative bias of the electrode. In the case of the anode, recombination occurs in the diffusion-cooling region, an effect that in turn reduces the electric-field value. For the anode, convection of the inlet gas mixture dominates electron dynamics, by limiting the effect of electron-ion recombination. We also note that, as the electrode is biased increasingly positive (i.e., behaves more and more like an anode), the ion flux toward the surface gradually approaches zero. As previously discussed by Self and Eskin[12] and Cappelli,[9] the point at which the ion flux reaches zero can be considered an ion-current saturation limit, since further increases in the drawn current would require ion emission from the electrode.

B. Inclusion of the neutral thermal boundary layer

Survival of a realistic electrode in the above conditions requires active cooling to a temperature well below the free-stream plasma temperature. The presence of a cooled wall results in the development of a thermal boundary layer for the bulk gas, as shown in Fig. 4(a). Here we have fixed the electrode temperature at $T_w = 1200$ K or $T_w/T_\infty = 0.2$. If there were no net flow at $x = L$, the bulk temperature profile would be linear. The magnitude of the inlet velocity and the bulk plasma transport properties determine the thermal boundary layer thickness. Although the neutral/ion temperature includes Joule heating of the ions and collisional exchange with electrons, these effects are negligible for the currents considered in Fig. 4. For the bulk temperature, convection and conduction terms dominate.

Comparison of Fig. 4(b) with Fig. 2 above demonstrates a significant influence of electrode cooling on the electric field. This effect is more easily understood by considering the results presented in Fig. 5. In Fig. 5(a) the presence of the bulk-flow thermal boundary layer suppresses the effect of Joule heating in the cathode case through increased collisional energy transfer between the electrons and the bulk. In the floating case, collision energy exchange causes the electrons to cool below their free-

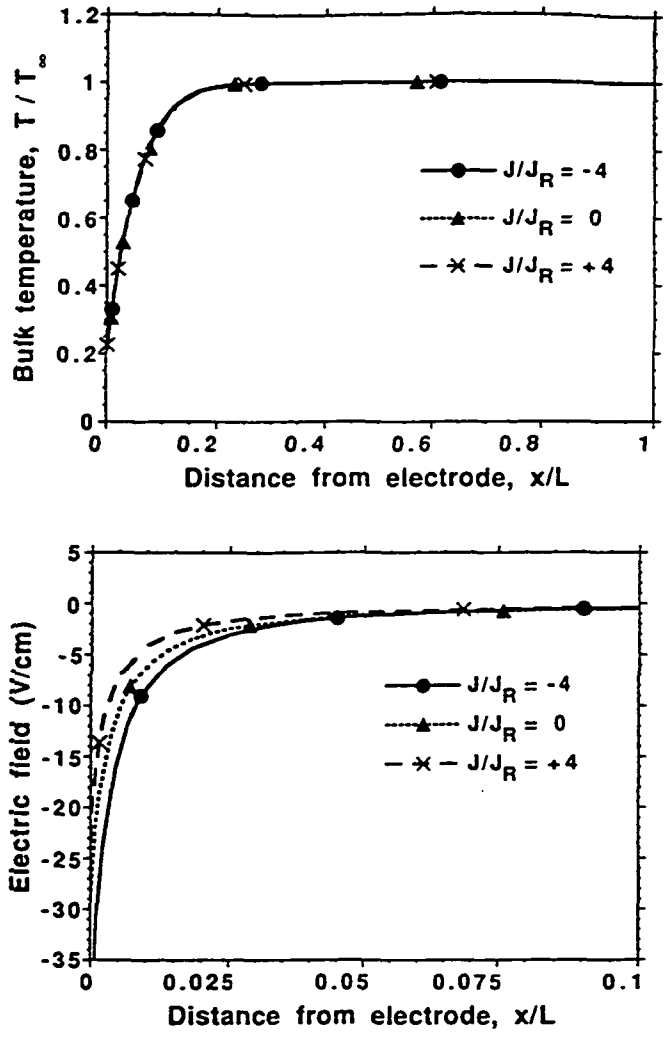

FIG. 4. (a) Neutral temperature profile for cooled electrode and (b) resulting electric field for cathode, anode, and floating cases.

stream temperature. In the anode case, however, the boundary layer has a smaller effect on electron temperature, since energy exchange with the bulk is now smaller than in Fig. 3(a). In all cases the electron temperature remains significantly out of equilibrium with the neutral species near the electrode. In the cathode and floating case, lower electron temperatures result in decreased ionization, increased recombination, and a shift of the electron production peak nearer to the electrode surface. The consequent reduction in ion flux away from the production source suppresses the tendency of the electric field to change sign midstream. In all cases, electrode cooling results in significantly larger magnitudes of the electric field near the electrode. With decreased ionization, increased recombination in the bulk and a high recombination rate at the surface, the electric field compensates for the tendency of electrons to diffuse rapidly toward the surface, maintaining overall charge neutrality.

An important issue in arc-jet modeling is the determination of the potential fall near an electrode surface. Although we cannot provide a quantitative measure of the total potential drop through the plasma sheath without inclusion of Poisson's equation, we can determine the qualitative behavior of the potential fall in the presheath region that results from the presence of the surface. We define $\Delta\varphi_{\text{quas}}$ as the integral of the electric field, excluding the field contribution arising from the net current flow, for the quasineutral formulation:

$$\Delta\varphi_{\text{quas}} \equiv \varphi|_{x=0} - \varphi|_{x=L} = \int_0^L [E(x) - E(L)]\,dx = \int_0^L E(x)\,dx - E(L)L.$$

The results for $\Delta\varphi_{\text{quas}}$ as a function of total current density are shown in Fig. 6. When the thermal boundary layer is present, a distinct transition in potential behavior occurs for both the anode and cathode cases. For anode current values less than $J/J_R \simeq 8$, the plasma has positive resistance, corresponding to a diffuse mode. For higher currents, however, the plasma behavior reverses, corresponding to a possible transition to a constricted or arc mode. For the cathode case, this transition occurs at much lower currents. Neglect of the neutral thermal boundary layer would result in no observed diffuse mode for the cathode and a transition at higher currents for the anode case.

The ion fluxes at $x=0$ for the anode cases including the thermal boundary layer are shown in Fig. 7. The ion flux towards the electrode exhibits a minimum corresponding to the transition shown in Fig. 6.

C. Varying the rate of surface recombination

In the above cases we observe that the near-catalytic boundary condition imposed at the electrode surface largely determines the magnitude of the electric field. Figure 8 illustrates the effect of reducing the surface recombination rate on the plasma behavior for the case of a floating electrode. An important result indicated in Fig. 8(a) is that the electron number density at the electrode approaches a finite nonzero value as the surface recombination rate increases from a low value to the near-catalytic value. This would suggest that the extreme condition of $n_e=0$ employed by many authors (see, for example, Refs. 9, 12, 14, and 19) is unrealistic. Also, the fact that the electron number density appears to asymptote at high surface recombination values indicates that our choice of 10^{15} cm^4/s mol was appropriate in approximating a perfectly catalytic surface. In Fig. 8(b) the magnitude of the electric field at the surface becomes very large as the rate of catalysis increases. This is consistent with the electric field's inverse relationship with the electron number density at the surface and has been the source of singularities when a zero number-density condition is employed.[12] Figure 8(c) illustrates the effect of the surface electron-loss rate to the local gas-phase production rate at the electrode. For low surface recombination, electrons recombine in the gas, consistent with the boundary-layer cooling of the electrons. At high surface-recombination rates, however, the loss of electrons drives the ionization/recombination balance toward

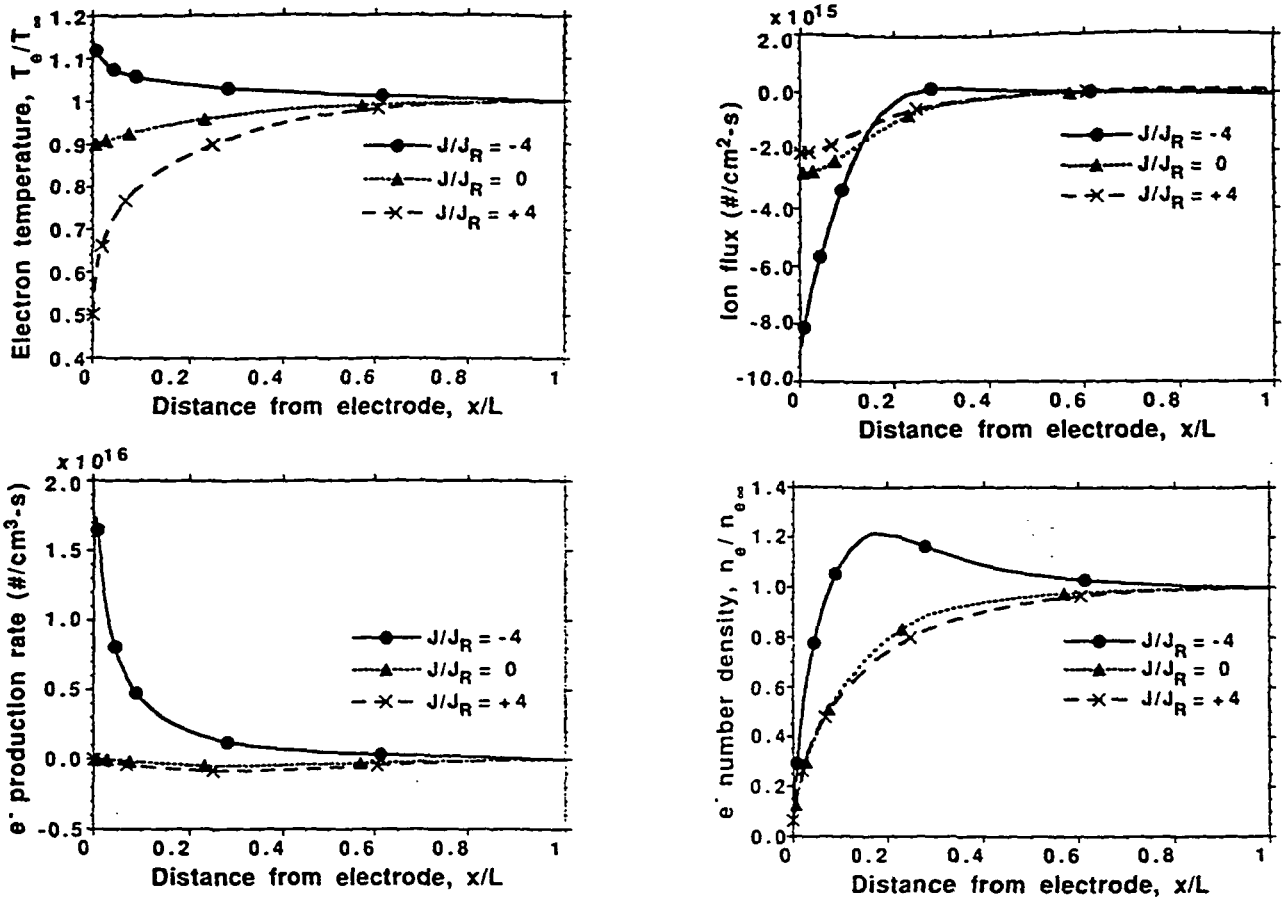

FIG. 5. Effect of varying current on plasma properties including thermal boundary layer at electrode.

ionization. Although a lower surface recombination rate reduces the electron temperature near the surface, this effect is small with the value of T_e/T_∞ at $x=0$ remaining between 0.8 and 0.9 for the electrically floating case considered here.

The above observations indicate the strong dependence of plasma behavior on the choice of a surface recombination rate. It is therefore difficult to predict quantitatively important plasma characteristics in this quasineutral formulation without first obtaining a better understanding of the surface third-body behavior in electron-ion recombination. However, inclusion of the plasma sheath in the complete formulation may significantly reduce the consequence of the rate choice. In the presence of net space charge near the surface, electrons are repelled from the sheath boundary. In this way, the electron loss may become transport limited, rather than surface-kinetic limited.

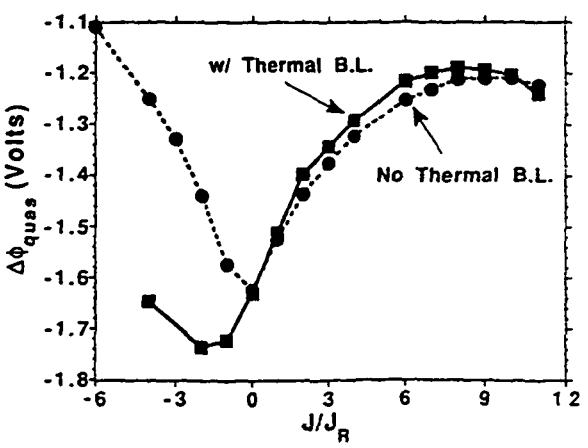

FIG. 6. Potential drop between the plasma free stream and the electrode as a function of total current density.

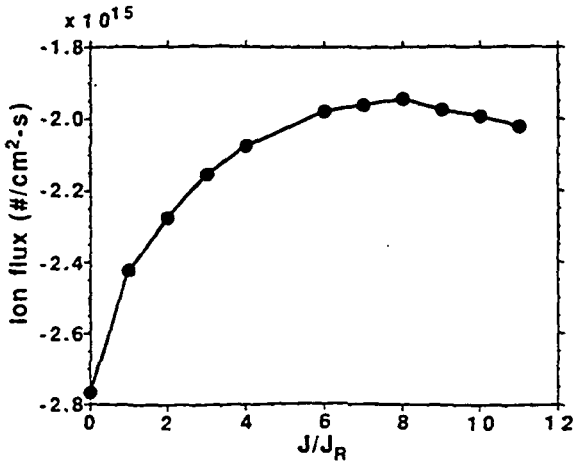

FIG. 7. Ion flux at $x=0$ as a function of total current density for the anode case.

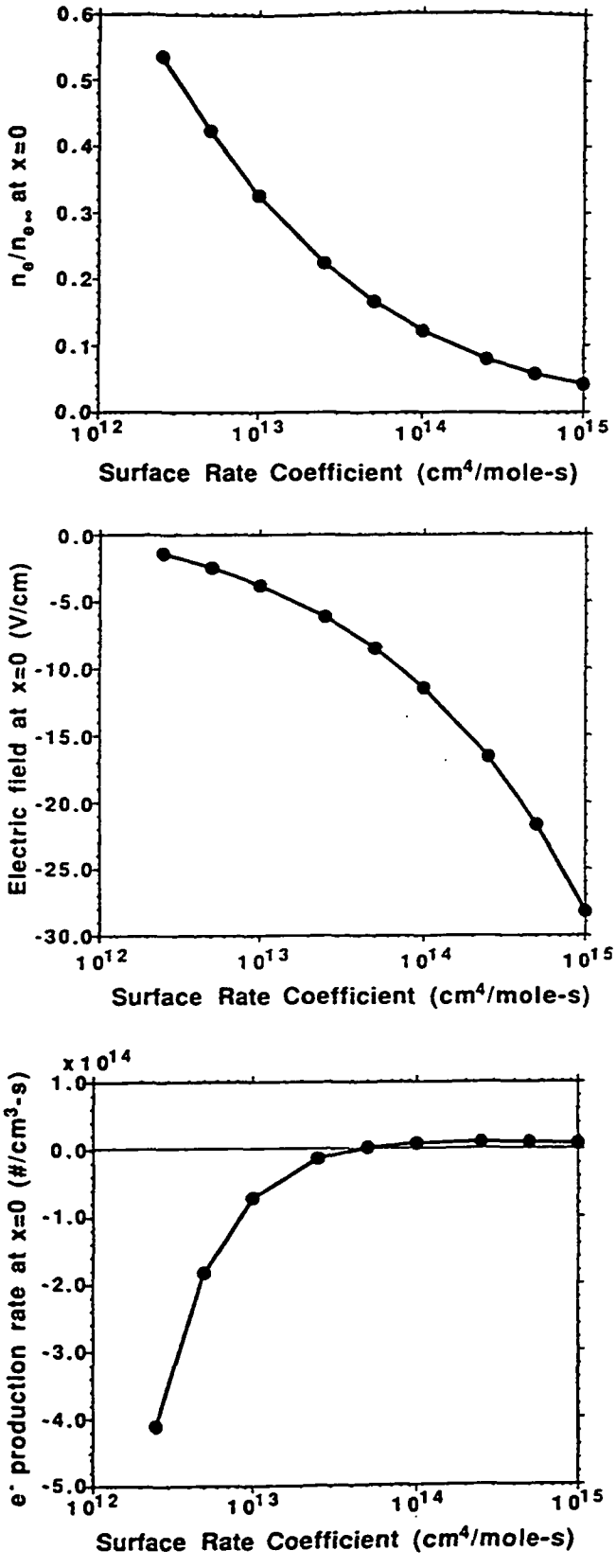

FIG. 8. Effects of varying the surface recombination rate coefficient on (a) electron number density, (b) electric field, and (c) electron generation rate near the surface for the case of $J=0$.

IV. CONCLUSIONS

We have presented a general formulation for a chemically reacting, multicomponent, weakly ionized plasma in stagnation flow against a cooled electrode. Through investigation of the quasineutral or thin-sheath limiting case, we provide a broad understanding of various parameters on plasma behavior in the presheath region. In particular, we have demonstrated the importance of including the neutral thermal boundary layer that arises from electrode cooling and electron thermal nonequilibrium near the stagnation surface. These effects have important consequences on the determination of the presheath potential fall and prediction of a transition between diffuse and constricted modes of arc attachment. In addition, we have demonstrated the high sensitivity of the magnitude of the ambipolar electric field on the choice of boundary condition for ions and electrons near the electrode. In future analyses, inclusion of Poisson's equation in the general formulation can be compared with the thin-sheath approximation to better understand the consequences of the quasineutral assumptions.

ACKNOWLEDGMENTS

E. M. acknowledges support by Sandia National Laboratories in cooperation with the U.S. Department of Energy with additional support from the Materials Science Program at the Defense Advanced Research Projects Agency (DARPA). M. A. C. acknowledges support from NASA Lewis Research Center. We also thank R. J. Kee for many useful discussions on CHEMKIN and multicomponent-transport issues.

[1] L. Talbot, Phys. Fluids 3, 289 (1960).
[2] I. M. Cohen, Phys. Fluids 6, 1492 (1963).
[3] C. H. Su and S. H. Lam, Phys. Fluids 6, 1479 (1963).
[4] S. H. Lam, AIAA J. 2, 256 (1964).
[5] H. K. Messerle and A. J. Manglick, Phys. D. 11, 1073 (1978).
[6] P. M. Chung, L. Talbot, and K. J. Touryan, AIAA J. 12, 144 (1974).
[7] H. A. Dinulescu and E. Pfender, J. Appl. Phys. 51, 3149 (1980).
[8] K. C. Hsu and E. Pfender, J. Appl. Phys. 54, 3818 (1983).
[9] M. A. Cappelli, in *28th Joint Propulsion Conference* (AIAA, Nashville, TN, 1992), AIAA 92-3109.
[10] M. A. Jog, I. M. Cohen, and P. S. Ayyaswamy, Phys. Fluids B 4, 465 (1992).
[11] I. M. Cohen, Phys. Fluids 24, 1373 (1981).
[12] S. A. Self and L. D. Eskin, IEEE Trans. Plasma Sci. PS-11, 279 (1983).
[13] S. H. Lam, in *14th Intersociety Energy Conversion Engineering Conference* (American Chemical Society, Washington, DC, 1979), pp. 1908–1911.
[14] J. L. Lawless and S. H. Lam, J. Appl. Phys. 59, 1875 (1986).
[15] M. S. Barnes, T. J. Colter, and M. E. Elta, J. Appl. Phys. 61, 81 (1987).
[16] J.-P. Boeuf, Phys. Rev. A 36, 2782 (1987).
[17] D. B. Graves, J. Appl. Phys. 62, 88 (1987).
[18] E. Gogolides, J.-P. Nicolai, and H. H. Sawin, J. Vac. Sci. Technol. A 7, 1001 (1989).
[19] D. B. Graves and K. F. Jensen, IEEE Trans. Plasma Sci. PS-14, 78 (1986).
[20] A. D. Richards, B. E. Thompson, and H. H. Sawin, Appl. Phys. Lett. 50, 492 (1987).
[21] M. J. Kushner, J. Appl. Phys. 53, 2923 (1982).
[22] R. J. Kee, G. Dixon-Lewis, J. Warnatz, M. E. Coltrin, and J. A. Miller, Sandia National Laboratories Report SAND86-8246, 1986.
[23] M. E. Coltrin, R. J. Kee, and G. H. Evans, J. Electrochem. Soc. 136, 819 (1989).
[24] R. J. Kee, F. M. Rupley, and J. A. Miller, Sandia National Laboratories Report SAND89-8009, 1990.

[25] R. J. Kee, F. M. Rupley, and J. A. Miller, "The Chemkin Thermodynamic Data Base," Sandia National Laboratories Report SAND87-8215B, 1990.
[26] M. E. Coltrin, R. J. Kee, G. H. Evans, E. Meeks, F. M. Rupley, and J. F. Grcar, Sandia National Laboratories Report SAND91-8003, 1991.
[27] M. E. Coltrin, R. J. Kee, and F. M. Rupley, Int. J. Chem. Kinetics 23, 1111 (1991).
[28] M. E. Coltrin, R. J. Kee, and F. M. Rupley, Sandia National Laboratories Report SAND90-8003B, 1991.
[29] S. A. Self and L. D. Eskin, Stanford University, Mechanical Engineering Department Report MR-2, 1985.
[30] K. Okazaki, T. Makabe, and Y. Yamaguchi, Appl. Phys. Lett. 54, 1742 (1989).
[31] A. P. Paranjpe, Ph.D. thesis, Stanford University, 1989.
[32] M. Surendra, D. B. Graves, and G. M. Jellum, Phys. Rev. A 41, 1112 (1990).
[33] P. M. Chung, Phys. Fluids 12, 1623 (1969).
[34] G. Dixon-Lewis, in *Combustion Chemistry*, edited by William C. Gardiner, Jr. (Springer, New York, 1984), pp. 21–121.
[35] H. Schlichting, *Boundary-Layer Theory* (McGraw-Hill, New York, 1955).
[36] R. J. Kee, J. A. Miller, G. H. Evans, and G. Dixon-Lewis, Twenty-second Symposium (International) on Combustion, The Combustion Institute, 1988, pp. 1479–1494.
[37] J. F. Grcar, Sandia National Laboratories Report SAND91-8230, 1991.
[38] J. F. Grcar, R. J. Kee, M. D. Smooke, and J. A. Miller, Twenty-first Symposium (International) on Combustion, The Combustion Institute, 1986, pp. 1773–1782.
[39] J. O. Hirshfelder, C. F. Curtiss, and R. B. Bird, *Molecular Theory of Gases and Liquids* (Wiley, New York, 1954).
[40] M. Mitchner and C. H. Kruger, *Partially Ionized Gases* (Wiley, New York, 1973).
[41] E. Hinnov and J. G. Hirschberg, Phys. Rev. 125, 795 (1963).

APPENDIX B

Page Intentionally Left Blank

Laser-induced fluorescence diagnostic for temperature and velocity measurements in a hydrogen arcjet plume

John G. Liebeskind, Ronald K. Hanson, and Mark A. Cappelli

A diagnostic has been developed to measure velocity and translational temperature in the plume of a 1-kW-class arcjet thruster operating on hydrogen. Laser-induced fluorescence with a narrow-band cw laser is used to probe the Balmer α transition of excited atomic hydrogen. The velocity is determined from the Doppler shift of the fluorescence excitation spectrum, whereas the temperature is inferred from the lineshape. Analysis shows that although Doppler broadening is the only significant broadening mechanism, the fine structure of the transition must be taken into account. Near the exit plane, axial velocities vary from 4 to 14 km/s, radial velocities vary from 0 to 4 km/s, and swirl velocities are shown to be relatively small. Temperatures from 1000 to 5000 K indicate high dissociation fractions.

Key words: Laser-induced fluorescence, arcjet, atomic hydrogen, Doppler shift, Doppler broadening, velocity, temperature.

Introduction

Arcjets are effective devices for producing high-enthalpy gas flows for applications in materials processing, metal cutting, atmospheric reentry simulation, and spacecraft propulsion. This paper is motivated by the propulsion application, in which arcjet thrusters are targeted for satellite station keeping, vehicle orbit transfer, and space exploration.[1] Arcjets' value in this application stems from the high mean mass velocity that is generated at the nozzle exit. This figure of merit is referred to as the specific impulse, or I_{sp}, and is determined from the ratio of thrust to propellant mass-flow rate. The I_{sp} of chemical rockets is limited because the stagnation temperature cannot exceed the adiabatic flame temperature. This limits the amount of energy available for conversion to kinetic energy. In arcjet thrusters, the energy is coupled via a constricted arc, where much higher temperatures can be obtained, and in practice an I_{sp} can be achieved that is 2 to 3 times that of the best chemical rockets.

The interaction of the arc with the gasdynamic flow creates a complex environment that is difficult to analyze. The cathode is located in a stagnation plenum in the converging section of the nozzle (see Fig. 1). The arc extends from the tip of the cathode through the throat and attaches diffusely to the nozzle–anode in the low-pressure diverging section. The submillimeter throat carries high currents (10 A) and sustains high radial temperature and velocity gradients. Simplified analytical models suggest centerline temperatures in excess of 30,000 K,[2] whereas the throat walls are below the tungsten nozzle's melting point. The ionization and molecular dissociation followed by the large expansion and the high velocities contribute to nonequilibrium conditions at the exit plane. Diagnostics of the plume can lead to a better understanding of the plasma dynamics by determining the conditions of the flow field. Velocity is important because it correlates with thrust, whereas kinetic temperature indicates the amount of enthalpy remaining in the gas.

This paper describes the development of a diagnostic that uses laser-induced fluorescence (LIF) to measure velocity and temperature in the plume of an arcjet thruster. The laser probe is focused to a small diameter in the arcjet plume. Subsequent fluorescence is collected and imaged onto a detector. Flow properties are determined from the behavior of the fluorescence signal as a function of the laser frequency (wavelength). This nonintrusive spectroscopic technique has several advantages. Measurements can be made in the vicinity of the exit plane

The authors are with the High Temperature Gasdynamics Laboratory, Department of Mechanical Engineering, Stanford, California 94305.

Received 8 September 1992.
0003-6935/93/306117-11$06.00/0.

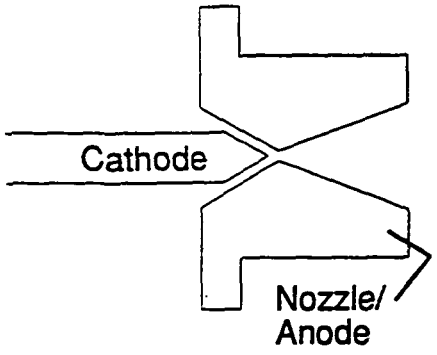

Fig. 1. Arcjet nozzle configuration. The throat diameter is 0.64 mm, and the expansion area ratio is 225.

where solid probes would fail because of the high enthalpy of the flow or would otherwise be difficult to interpret. In addition, the ability to focus the probe laser to small sizes allows for high spatial resolution. This is particularly important in arcjets, where large variations in velocity and temperature occur across the small, 1-cm diameter of the nozzle exit.

Velocity is determined from the Doppler shift of the fluorescence excitation spectrum. This technique has been demonstrated in a variety of flows and has been adapted for use in arcjets.[3,4,5] The translational temperature is determined from the shape of the fluorescence excitation spectrum. In contrast to velocity, the temperature is more difficult to infer because of competing mechanisms that act to broaden the measured profile and the complex nature of the overlapping line components. This paper uses a tunable narrow-band cw laser to resolve the line-absorption profile generated through fluorescence excitation.

Theory

LIF involves excitation of an atomic or molecular species from a lower to a higher quantum state by absorption of laser radiation, with subsequent emission of radiation (fluorescence). To avoid use of additive tracer molecules, an inherent species with a suitable transition is preferred. The exhaust plume of a hydrogen-fueled arcjet consists primarily of neutral and singly ionized atomic and molecular hydrogen as well as electrons. The Balmer α transition of atomic hydrogen was selected owing to its accessibility at 656.28 nm, the substantial population of atomic hydrogen in the absorbing state at arcjet conditions, and the transition's relatively large oscillator strength. A partial energy level diagram for hydrogen is shown in Fig. 2 (Ref. 6). The Balmer α transition gives rise to the first spectral line of the well-known Balmer series. In this series the lower energy level is the first excited state with n (the principal quantum number) = 2. Note that the Lyman series, in which the lower level is the ground state ($n = 1$), involves transitions in the vacuum ultraviolet for which suitable cw laser sources are not yet available. Fluorescence is obtained when the

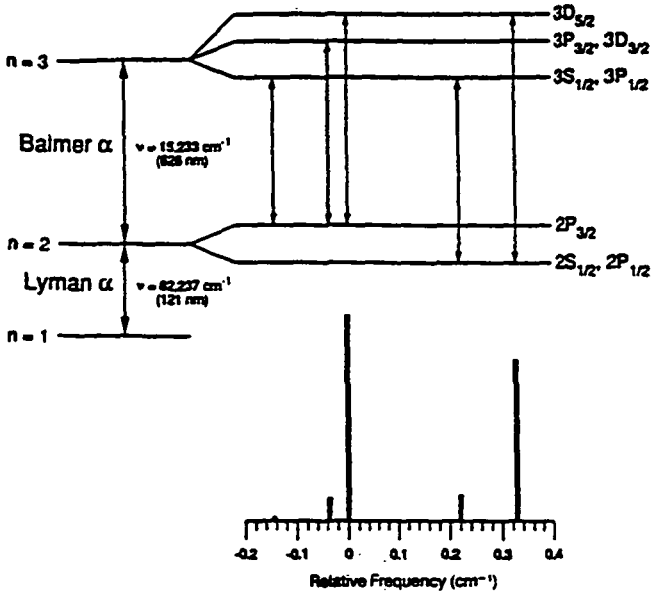

Fig. 2. Hydrogen atom energy level diagram with the fine structure that is due to spin-orbit coupling. The corresponding transitions are shown below the diagram with their relative separations and intensities.

laser is tuned to the frequency resonant with the energy difference between the two states of an allowed transition. The laser, which is focused to the point of interest in the flow, induces some of the atoms in the lower state to absorb a photon, thus pumping them into the upper state. Some of these atoms in the upper state will spontaneously decay back to the lower state by emitting a photon. If the atom undergoes an elastic collision in the interim between the absorption and re-emission processes, the photon will be emitted in an arbitrary direction with a random phase. The rate at which photons arrive at the detector is[7]

$$n_p = n_u A_{ul} V \varepsilon \frac{\Omega}{4\pi}, \tag{1}$$

where n_u is the number density of the upper level, A_{ul} is the Einstein spontaneous emission coefficient, V is the fluorescence probe volume, ε is the efficiency of the collection optics, and Ω is the solid angle subtended by the collection optics. Because of the high temperature, the population in the upper level, n_u, may be significant in the absence of laser excitation. This can lead to a large background signal. For this paper, the number of atoms excited to $n = 3$ by the probe laser is 1 to 2 orders of magnitude smaller than the number of atoms in the $n = 3$ state without laser excitation.

In considering LIF as a velocity diagnostic, we first recognize that each species comprising the flow will have a distribution of velocities. Let u represent the ith species' velocity component along a specified axis and $f_i(u)$ be the distribution function of this species' velocity component. The distribution function represents the fraction of species i having a velocity

component between u and $u + du$. By definition,

$$\int_{-\infty}^{+\infty} f_i(u)\mathrm{d}u = 1. \quad (2)$$

The mean velocity for a species i along the specified coordinate can now be defined by

$$v_i = \int_{-\infty}^{+\infty} u f_i(u)\mathrm{d}u. \quad (3)$$

Mean velocities for different species may vary because of diffusion. The mean mass velocity of the flow is

$$v = \frac{\Sigma\, \rho_i v_i}{\Sigma\, \rho_i}, \quad (4)$$

where ρ_i is the local density of species i. LIF techniques determine the mean velocity of the probed species (v_i) along the direction of laser propagation from the Doppler shift of the fluorescence excitation spectrum. The Doppler shift, $\Delta\nu$, is given by

$$\Delta\nu = \nu_0 \frac{v_i}{c}, \quad (5)$$

where ν_0 is the laser frequency, v_i is the mean velocity in the direction of laser propagation, and c is the speed of light. A stationary hydrogen plasma discharge is used to provide a reference (unshifted) frequency.

The temperature is determined from the shape of the fluorescence excitation spectrum. However, because the Balmer α transition actually consists of several overlapping transitions, any effort to analyze line shapes must account for this structure. The upper and lower states are split by spin-orbit coupling. The split states, referred to as the fine structure, are identified by the quantum number j, which indicates the total angular momentum. Selection rules allow for five different optical transitions between the two manifolds. The line shape function of the Balmer α transition can be modeled as the superposition of these five components with their appropriate broadening mechanisms and relative intensities. The fine structure and the five transition components are shown in Fig. 2. The relative position and intensities of each component are listed in Table 1.[8] Note that the last two components each consist of two degenerate transitions.

Given the relative position and intensities of the various components, the line-shape function of the Balmer α transition is determined by the broadening mechanisms. The predominant broadening mechanism associated with the Balmer α transition in low-power (1–5 kW) arcjet exhausts is Doppler broadening. Each velocity class u, where u is the velocity component in the direction of laser propagation, will have its own Doppler shift. Generally the distribution function $f_i(u)$ is taken to be Maxwellian centered about the mean velocity v_i. Although large gradients in the temperature and velocity can distort the Maxwellian distribution,[9] we consider these distortions to be negligible. The Doppler shifts are combined with the Maxwellian distribution to give a Gaussian fluorescence intensity profile[10]

$$\Phi_D(\nu) = \frac{2}{\Delta\nu_D}\left(\frac{\ln 2}{\pi}\right)^{1/2} \exp\left[-4 \ln 2\left(\nu \frac{\nu - \nu_0}{\Delta\nu_D}\right)^2\right]. \quad (6)$$

$\Phi_D(\nu)$ is generally referred to as the normalized line-shape function and $\Delta\nu_D$ is the FWHM (full width at half maximum or Doppler half-width) given by

$$\Delta\nu_D = \nu_0'\left(\frac{8kT \ln 2}{mc^2}\right)^{1/2}, \quad (7)$$

where ν_0' is the line center or unshifted frequency, m is the mass of the atom, k is Boltzmann's constant, and T is the translational temperature. Because hydrogen is the lightest atom, wide profiles are encountered. Temperatures in the arcjet vary from 1000 to 5000 K, corresponding to half-widths (for each component) of 0.35 to 0.77 cm^{-1}. Neglecting the fine structure at 4000 K leads to an inferred temperature of 5500 K. This error increases at lower temperatures.

The broadening of the Balmer α transition that is due to other mechanisms is expected to be small in comparison with Doppler broadening and has been neglected. The most significant of these is Stark broadening. The Stark-broadened half-width is a monotonically increasing function of electron number density.[11] Emission scans of the Balmer β transition ($n = 4$ to $n = 2$ at 486 nm) were made with a monochromator having entrance slits imaged onto the centerline of the plume near the exit plane. A FWHM of 0.38 Å (1.6 cm^{-1}) was measured, which is approximately the spectral resolution of the monochromator. This width can be used to determine an upper limit of 2×10^{13} cm^{-3} for the electron number density assuming a temperature of 5000 K (the exit plane temperature at the plume's center).[11] This estimated upper limit is in agreement with a study of a similar arcjet operating on simulated hydrazine.[12] The Balmer α transition is much less affected by Stark broadening. At this electron number density,

Table 1. Components of the Balmer α Transition and Their Properties (Ref. 8)

Upper j	Lower j	$\delta\nu$ (cm^{-1})	Transition	Relative Intensity
1/2	3/2	−0.144	$3S_{1/2} \leftrightarrow 2P_{3/2}$	0.05
3/2	3/2	−0.036	$3D_{3/2} \leftrightarrow 2P_{3/2}$	0.28
5/2	3/2	0.0	$3D_{5/2} \leftrightarrow 2P_{3/2}$	2.50
1/2	1/2	0.220	$3S_{1/2} \leftrightarrow 2P_{1/2}$	0.31
			$3P_{1/2} \leftrightarrow 2S_{1/2}$	
3/2	1/2	0.328	$3P_{3/2} \leftrightarrow 2S_{1/2}$	1.96
			$3D_{3/2} \leftrightarrow 2P_{1/2}$	

the Balmer α transition is broadened with a Lorentzian line shape having a FWHM of only 0.01 cm^{-1}.[11]

Resonance broadening occurs when atoms in the upper or lower levels of the transition can undergo a resonant exchange of energy with a perturbing species. The broadening is Lorentzian in shape with a half-width proportional to the number density of the perturbing species and the oscillator strength of the resonant transition.[13] In the arcjet plume, the most populated species with a resonant energy level is ground-state atomic hydrogen. To get an estimate of resonance broadening, an estimate of the ground-state H-atom density is needed. For this purpose, we assume that the density, ρ, of the flow can be estimated from a quasi-one-dimensional conservation of mass. The mean mass-flow rate is given by

$$\dot{m} = \rho v A, \tag{8}$$

where A is the nozzle exit area and v is velocity. If a velocity of 5×10^3 m/s and a dissociation fraction of 30% are used, the H-atom number density is 10^{22} m^{-3}. If interactions between both the upper and lower levels of the Balmer α transition are considered, the Lorentzian resonance-broadened half-width is 0.005 cm^{-1}. Within the framework of the above assumptions, this gives an estimate that is negligible compared with Doppler broadening. Nonresonant pressure broadening is also considered negligible because of the low pressures and high temperatures in the arcjet plume.

Lifetime broadening arises as a result of the depopulation of both levels of the transition by radiative decay.[10] This broadening leads to a Lorentzian line shape. The half-width, which is calculated from the sum of all downward Einstein spontaneous emission coefficients from both the upper and the lower states involved in the transition, is given by

$$\Delta\nu_L = \frac{1}{2\pi}\left(\sum_{j=1}^{u-1} A_{uj} + \sum_{j=1}^{l-1} A_{lj}\right). \tag{9}$$

For the Balmer α transition this summation yields a linewidth of 0.003 cm^{-1}.[6]

Transit-time broadening occurs when high mean or thermal velocities are present in a small fluorescence probe volume. The short interaction time between the atoms and the laser acts to decrease the lifetime of the fluorescence state. A characteristic time is determined from the ratio of a characteristic length to the velocity. The characteristic length for this experiment is the laser beam waist of 0.1 mm. The peak velocity is 14 km/s. This gives a characteristic time of 7×10^{-9} s, which acts as a limiting lifetime. This would add 0.005 cm^{-1} to the linewidth. Hence this mechanism can also be neglected.

At high power levels, the laser can significantly perturb the populations of the atomic states and thereby distort the absorption line-shape function. This effect is known as saturation broadening or power broadening. The induced absorption reduces the number of atoms in the lower ($n = 2$) state while increasing the number of atoms in the upper state ($n = 3$). If the number of atoms involved in this process is small compared with the total number of atoms in these states, the fluorescence signal is linear with the laser intensity and the line shape is independent of the laser intensity. When the laser intensity becomes large, the populations of the two states change significantly. This change is limited to a condition known as saturation, where the maximum ratio of populations of the two states is equal to the ratio of the degeneracies. As saturation is approached, the fluorescence signal becomes a nonlinear function of the laser intensity, causing the excitation line-shape profile to become broader. To determine precisely the line centers and line shapes, saturation has been quantified and avoided.

Other artifacts of the experiment can act to distort the shape of the measured excitation spectrum. The most significant of these are due to reductions of the spatial and temporal resolutions. If the velocity at a point changes in a time period shorter than the measurement time (several minutes), the measured profile will be a convolution of the varying Doppler shift and the instantaneous line shape. Ripple in the power supply that drives the arc discharge might lead to a modulation of the arcjet velocity. Because the temperatures obtained from vertical excitation (with no mean velocity) are the same as those obtained from axial excitation (with high mean velocity) it appears that variations in velocity are not a problem. Poor spatial resolution can lead to the examination of atoms with a finite range of mean velocities. The superposition of the differently shifted fluorescence signals would give rise to an apparent increased broadening. Good spatial resolution was maintained by keeping the diameter of the fluorescence probe volume small so that the range of mean velocities was negligible and by ensuring that the collection optics were well focused.

Experiment

The arcjet thruster used in this experiment is a 1-kW-class radiatively cooled thruster designed and built at the National Aeronautics and Space Administration Lewis Research Center. The tungsten nozzle, as shown in Fig. 1, has a 0.635-mm diameter, a 0.25-mm-long constrictor, and a conical (20° half-angle) diverging section with an area ratio of 225 (9.53-mm exit diameter). A more complete description of the arcjet is available elsewhere.[14] Operating conditions for this experiment are 13 mg/s of H_2 propellant with a maximum power dissipation of 1.48 kW (voltage and current levels of 139 V and 10.3 A, respectively). The arcjet is operated in a 0.56-m-diameter cylindrical stainless-steel chamber 1.09 m long. The 0.35-Torr background pressure is maintained by two 1250-CFM blowers evacuating through 15-cm pipe.

A schematic of the experimental setup is shown in Fig. 3. The fluorescence excitation laser is a cw ring dye laser (Spectra Physics Model 380) pumped by a

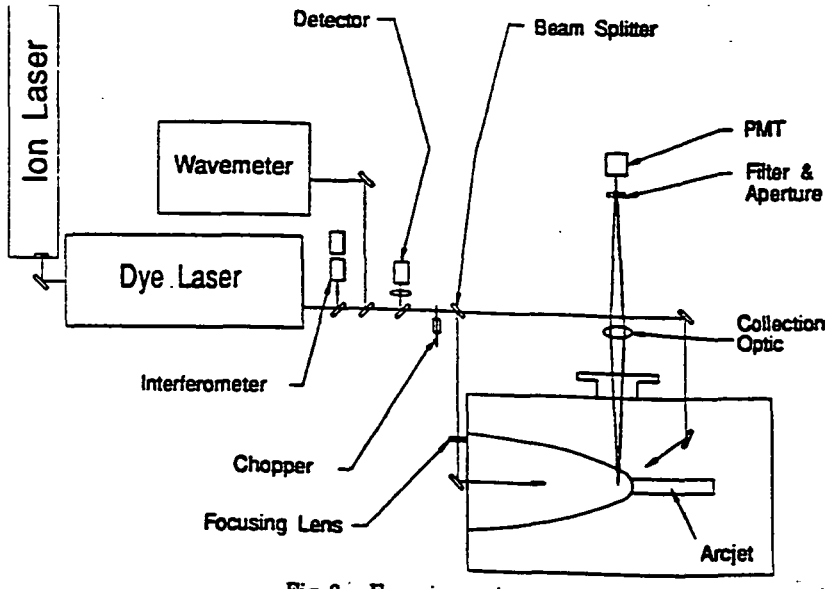

Fig. 3. Experimental setup.

6-W argon–ion laser and operating on DCM dye. The laser produces several hundred milliwatts of power at 15,233 cm^{-1} (656 nm) with a nominal bandwidth of 10 MHz. Because this bandwidth is significantly less than the half-width of the measured fluorescence excitation spectrum of the Balmer α transition, the shapes of the recorded line accurately depict the broadening mechanisms. Part of the beam is passed through a 2-GHz Fabry–Perot interferometer to monitor mode structure and ensure single-mode operation. Another portion of the beam is directed into a wavemeter (Burleigh WA-10) that uses a Michelson interferometer to measure laser frequency to within 0.01 cm^{-1}. A third beam splitter directs the laser to a photodiode detector that monitors laser power.

A beam splitter divides the laser into two beams of approximately equal intensity. One beam is for axial excitation and the other is for radial excitation. The beams are expanded and then focused through windows to a waist of 0.1 mm in the arcjet plume. The radial excitation beam is passed vertically through the plume. The axial beam is passed through a window in the end of the tank, and the thruster nozzle is used as a beam dump. The fluorescence signal is collected on a horizontal axis normal to both excitation beams. It is collected through an 83-mm-diameter window with a lens operating at f/5.7 (76 mm diameter, 280 mm focal length) and imaged onto a R928 photomultiplier tube (PMT) with a magnification of 2.7. A notch filter with a nominal 10 Å (23 cm^{-1}) bandwidth is placed directly in front of the PMT to filter extraneous light. A 0.4-mm aperture is mounted directly in front of the filter at the focal plane of the imaging lens to act as a field stop and determine the measurement location in the plume as well as the axial and vertical spatial resolution. Phase-sensitive detection is used to discriminate the fluorescence signal from the intrinsic plasma emission, which is 30 to 500 times greater. The lock-in amplifier (SRS SR530) is synchronized to a mechanical chopper at 3 kHz. The output from the lock-in is collected and stored in a laboratory computer along with the output from the wavemeter and laser power detector.

At each spatial point investigated, the laser is automatically scanned in frequency by varying the voltage on a (piezo-controlled) 75-GHz intracavity étalon. Radial and axial excitation are obtained on separate scans by blocking one of the beams. The laser is able to scan over a range of up to 2 cm^{-1}. This is enough to capture most of the fluorescence excitation line. Typical scan times are a few minutes.

Both the arcjet and a stationary hydrogen discharge were used as a stationary (unshifted) reference. In the former case, it is assumed that the flow is axisymmetric, which implies that the radial velocity is zero at the centerline. The symmetry of both the axial and radial velocity profiles confirms this assumption. The wavemeter provides enough accuracy and repeatability to forego simultaneous reference scans. The stationary discharge was produced in a low-pressure hydrogen cell mounted in a microwave cavity, which acted as a source of slow (essentially stationary) H atoms.

The velocity and temperature are determined by a least-squares fit to the line-shape model with the Levenberg–Marquardt method.[15] The model consists of five components with specified relative intensities and separations. Doppler broadening is the only broadening mechanism considered. There are three parameters that are used to fit the data to the model. These are the Gaussian half-width, the line shift, and the integrated intensity. The temperature is determined from the Gaussian half-width. The velocity is determined from the shift of the fluorescence excitation profile relative to that of the reference spectrum. The integrated intensity was

necessary to fit the other parameters but can also be used to determine relative excited H atom densities.

Results and Discussion

The effect of saturation was evaluated by comparing LIF line profiles for a range of laser-power levels. For the 0.1-mm laser spot size, the fluorescence was found to be linear below 60 mW. Thus all data were taken with laser powers well below this level.

Two typical fluorescence excitation scans are shown in Fig. 4. The scan on the left is taken from the plume centerline 0.4 mm from the exit plane with axial excitation where the measured temperature is 4500 K. The scan on the right is from the colder, 600 K stationary reference discharge. At temperatures below approximately 1000 K, the Balmer α line shape begins to look more like a doublet. This is due to the fine structure discussed in the Experiment section. The solid curves in Fig. 4 correspond to the model's fit to the data. The fluorescence intensity is the ratio of the output signal from the lock-in amplifier to the signal from the photodiode that monitors laser power. Accounting for laser power in this way preserves the line shape because the fluorescence is linear and not saturated. The power varies by up to 10% as the laser scans in frequency. Both profiles were normalized by their areas to facilitate comparisons of the line shapes between the hot and cold gases. These profiles consist of 70 to 200 data points each, with the data taken at 1-s intervals. Profiles from regions further from the centerline require longer scan times because of decreased signal-to-noise ratios.

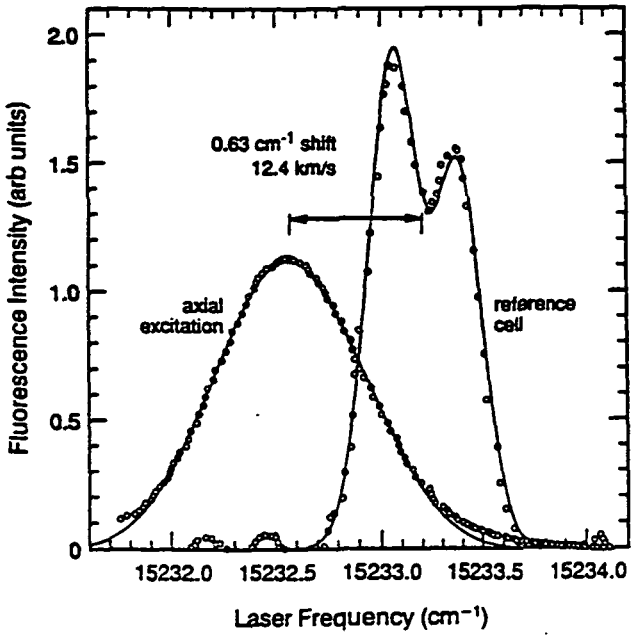

Fig. 4. Sample data taken near the centerline 0.4 mm from the exit plane with the fluorescence excitation spectrum from axial excitation and from the (unshifted) reference cell. The 0.63 cm^{-1} shift corresponds to a 12.4 km/s velocity. Both profiles are normalized by their areas after subtraction of the baseline.

Two laser probe beams are focused to the same small volume on the plume centerline 0.4 mm from the exit plane. The two beams have respective propagation vectors aligned along the radial and axial directions of the arcjet plume. Data were taken as the arcjet was positioned at a variety of vertical locations. Figure 5 shows the radial profile of the axial velocity. The profile is highly peaked at 14 km/s with a fairly linear gradient away from the peak. Note that the profile is shifted approximately 0.7 mm from the indicated centerline (0 mm radial location). This is most likely due to the difficulty in establishing the plume centerline, rather than deviation of the arcjet plume from axisymmetric flow. In establishing the plume centerline the axial laser beam is aligned by centering it on the cathode tip, which is more than 13 mm beyond the exit plane. If the arcjet nozzle is not coaxial with the laser, the laser will pass through the exit plane at an off-center location. A 0.7-mm deviation at the exit plane corresponds to a 3° misalignment of the laser and arcjet.

The radial profile of the radial velocity component is shown in Fig. 6. The profile has a fairly linear shape and, like the axial velocity, is symmetric about the centerline. This validation of our symmetry assumption means that radial excitation at the centerline provides a reliable unshifted reference fluorescence profile. The magnitude of the radial velocity reaches a maximum of 4 km/s. This occurs near the edge of the nozzle, where the axial velocity is approximately the same magnitude, giving a velocity direction of 45° (from the arcjet axis). The flow direction is more clearly represented in Fig. 7, where the radial and axial velocities have been combined in a velocity vector format. Note that the axial velocity data from Fig. 5 were shifted to correct for the arcjet axis alignment problems. Figure 7 best shows the small

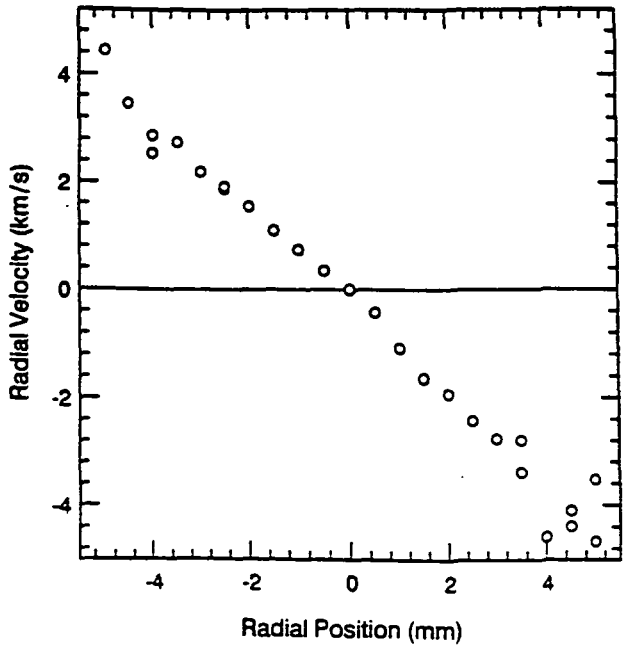

Fig. 5. Radial profile of axial velocity 0.4 mm from the exit plane. The exit plane radius is 4.8 mm.

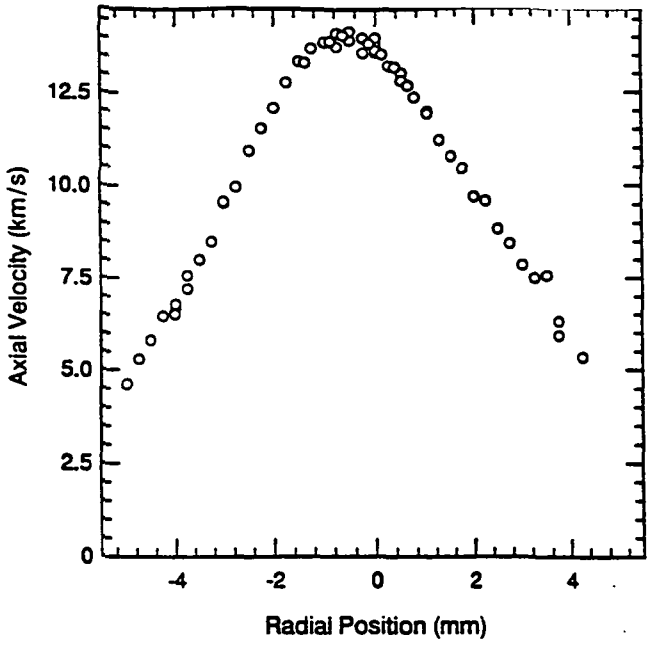

Fig. 6. Radial profile of the velocity in the vertical direction along a vertical line through the arcjet center, 0.4 mm from the exit plane.

asymmetry near the edges of the plume. This is most likely due to tank effects. The tank pump port is only 375 mm downstream from the arcjet exit plane and off to the side (280 mm from the centerline), allowing a nonaxisymmetric pressure field to develop.

Measurements were made of the velocity component in the angular direction about the axis (circumferential or swirl velocity). The swirl velocity is normal to both the radial and axial directions. To perform these measurements, the vertical probe beam was translating away from the plume centerline such that it remained normal to the radial velocity component. Velocities up to 1 km/s were measured near the edge of the plume. However, this is inconclusive because a minor misalignment of the arcjet with the laser axis can account for this result. If the laser is not completely normal to the radial axis, there will be a nonzero component of the radial velocity in the direction of laser propagation. This problem can be overcome by taking velocity measurements throughout the flowfield along a two-dimensional grid. The radial and swirl components can then be separated. The significance of the current results is that the swirl velocity components are apparently small compared with the radial or axial velocity components.

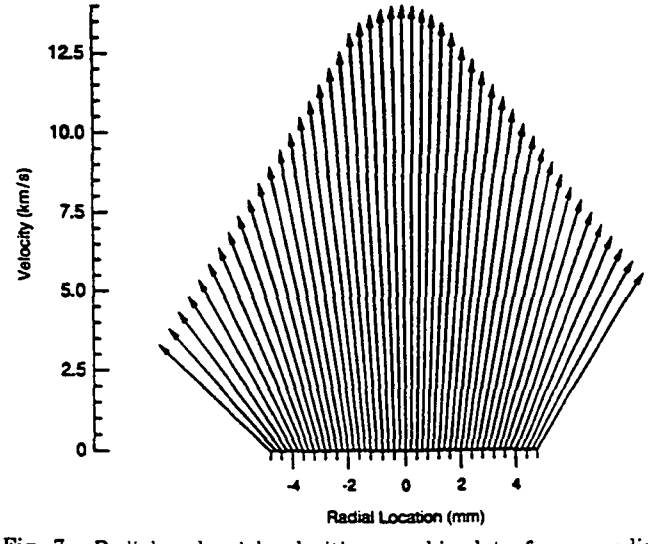

Fig. 7. Radial and axial velocities, combined to form a radial profile of the velocity vectors 0.4 mm from the exit plane.

The temperature is determined by fitting the data to the model as discussed above. In applying the fitting procedure, it was necessary to account for a positive baseline, which was caused by the scattering of laser light from surfaces. The temperature obtained from the model is sensitive to small changes in this baseline. The precision in determining the baseline can therefore limit the uncertainty of the temperature measurement. The large linewidths at the higher temperatures and limited scanning range of the laser prevent a complete scan of the entire fluorescence profile. Therefore, to establish the baseline on one side of the profile, a portion of the profile on the other side is truncated. This forces a compromise in the ability to establish the baseline and the ability to capture the width of the profile. At lower temperatures (where the densities are also lower) uncertainties are increased by noise in the baseline combined with high baseline-to-peak fluorescence ratios. At the radial edges of the plume, this ratio is as high as 70%, whereas at the centerline it is as low as 1%.

This sensitivity to the baseline is illustrated in Fig. 8, which shows fluorescence data along with three profiles obtained by fits to the model for different baseline values. The program that fits the data to the model can fit to a specified baseline, or it can determine a baseline by a least-squares fit. When the program determines the baseline by a fit, it overpredicts the baseline to compensate for an underprediction of the wings. That is, the program determines a baseline that is clearly higher than the actual baseline. This produces a temperature on the low side. When the baseline is forced to zero, the fitting procedure produces a temperature that is significantly higher. The most appropriate baseline is somewhere between these limits. For the results presented here, the baselines were all determined manually using interactive graphics software. For the fluorescence profile in Fig. 8, the two extreme baselines produce temperatures that differ by 900 K, or 20% of the determined temperature. If any significant portion of the left-hand side of this profile were omitted, a baseline could not be established. Alternatively, if the laser were tuned to begin scanning at a lower frequency, it could not scan enough of the profile to establish the width. All three of the fitted profiles underpredict the fluorescence in the wings. This error could be caused by Lorentzian broadening mechanisms, which are not included in the model. Lorentzian line shapes decay much more slowly in the

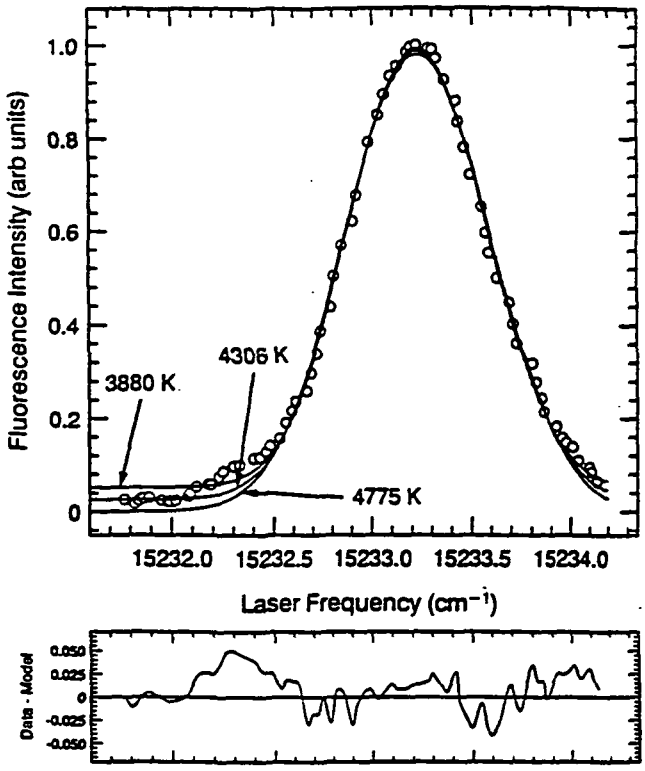

Fig. 8. Sample of raw data showing fits produced by the model. The three lines were fixed to different baselines and correspond to determined temperatures of 3880, 4306, and 4775 K. This figure illustrates the sensitivity of temperature determination to correct baseline establishment.

wings compared with Gaussian line shapes. Therefore, a small Lorentzian component to the broadening would first affect the wings. Because the effect is seen only in the wings, the overall error in the inferred temperature is small. To estimate the maximum error this might cause, a profile was generated by convolving a Lorentzian profile with a half-width of 0.01 cm^{-1} corresponding to an electron density of 10^{13} cm^{-1} and a Gaussian profile with a 0.70 cm^{-1} half-width corresponding to a temperature of 4200 K. This profile (which included the effects of the fine structure) was then fitted to the model used for data reduction. The Lorentzian component led to an overprediction of the temperature by 300 K, which is less than the uncertainty that was due to baseline establishment. The misfit in the wings is only present near the plume centerline, where the electron number density is likely to be the highest. Toward the plume edges, the fluorescence signal is weaker and the baseline is noisier, making the baseline equally difficult to locate. Examples of both of these phenomena can be seen in Fig. 8.

A radial profile of the temperature is shown in Fig. 9. The temperature peaks between 4000 and 5000 K at the centerline and falls to 1000 K at the edges of the plume. The shape is similar to the radial profile of the axial velocity with the same shift in the centerline. The scatter is relatively high because of the large uncertainties. The data presented were obtained from a mix of radial and axial laser excitation.

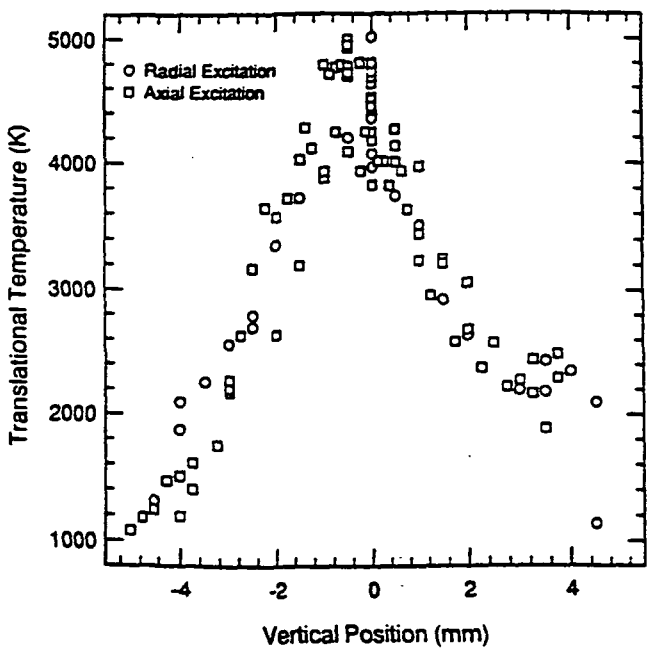

Fig. 9. Radial profile of translational temperature.

The overlap in the data indicates that there are no anisotropies or fluctuations in velocity.[5] Note that fluctuations of temperature give rise to the measurement of an average temperature. Fluctuations of velocity give rise to the measurement of the convolution of bulk velocity shifts and the instantaneous line shapes, leading to an erroneously high temperature. Because there is no radial velocity at the centerline, it is unlikely that there are any significant velocity fluctuations. Because the temperatures measured from radial and axial excitation are the same it follows that there are no significant fluctuations in the axial velocity.

The integrated intensity of the fluorescence excitation spectrum is a function of the number density of hydrogen in the absorbing state ($n = 2$). The radial profile of the integrated signal from data near the exit plane is shown in Fig. 10. The data are plotted on a log scale to show that the fluorescence signal drops by 2.5 orders of magnitude from the plume center to the edges. This is most likely due to decreases in both the Boltzmann fraction of the excited state as well as the dissociation fraction. This follows from the 3000 K decrease in temperature. If the quenching rate is small compared with radiative relaxation, the integrated fluorescence signal is directly proportional to the number density of H in the absorbing state. The large differences in energy between the upper fluorescence state and the adjacent states lead to small quenching cross sections, the low densities further decrease quenching rates, and the radiative lifetime of the fluorescence is short. However, without further knowledge of the collisional rates, we cannot make any quantitative conclusions about number densities.

Measurements were taken 0.4 mm from the exit plane at the centerline for a variety of arcjet power levels and a mass flow rate of 13 mg/s. The axial

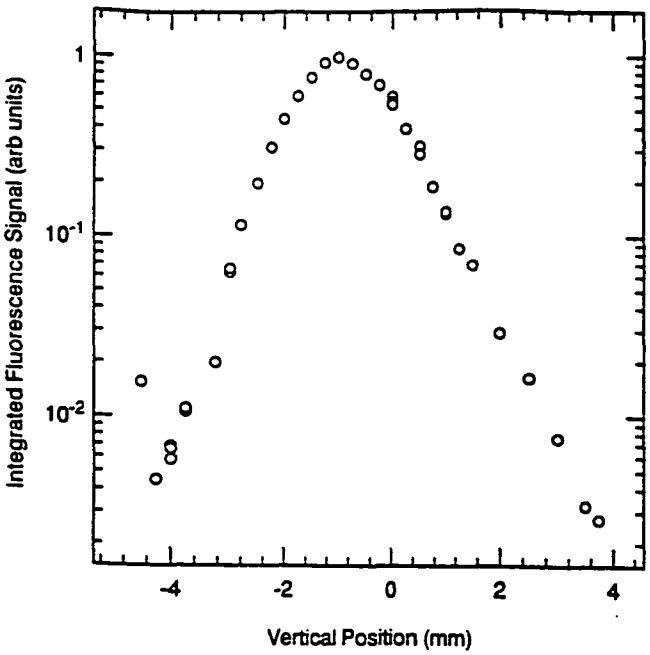

Fig. 10. Integrated fluorescence signal intensity profile, 0.4 mm from the exit plane.

velocities and temperatures are shown in Fig. 11. Note that when the input power is more than doubled, the centerline axial velocity increases by less than 30%. This is consistent with the variation of thrust with input power.[16] However, for the same change in power, the kinetic temperature increases approximately 3 times. This indicates an increased level of enthalpy that is convected out of the nozzle. This represents lost energy that is not converted to kinetic energy or thrust. This is consistent with a drop in the efficiency as calculated from thrust measurements.[16] The efficiency is defined as the ratio of I_{SP} to the sum of the specific power and I_{SP} that is produced with the arc off.

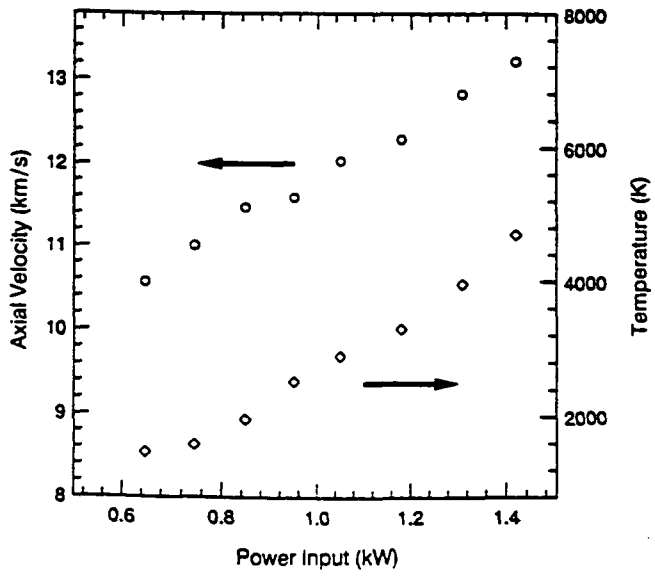

Fig. 11. Axial velocity and temperature at the centerline, 0.4 mm from the exit plane, for a variety of power levels.

When the arcjet is operating with argon propellant, a shock structure that is due to the mismatch between exit and background pressure is clearly visible in the varying emission intensity. However, when the arcjet is operating on hydrogen propellant, no such structure is visible. There could be several reasons for this, including a higher mean free path leading to relatively thick or diffuse shock waves; a more closely matched pressure at the exit plane; or more oblique shock angles, making radial viewing of the change in emission (because of the temperature jump) difficult. Measurements of the axial velocity and temperature were taken at a variety of locations along the centerline. Fig. 12 shows these results along with the Mach number as determined from the data (assuming single-component flow, see conclusions). The Mach number rises steadily from 1.4 at the exit plane to 3.0 at approximately 18 mm (2 exit diameters) downstream. After going through the shock, the Mach number drops. Note that the flow does not appear to be accelerating in the expansion region of the first 18 mm. The velocity is slowly decreasing until the Mach number peaks where the velocity begins to decrease more rapidly. The decreasing velocity in the expansion section is in part due to an off-axis probe volume. The measurements were made along the indicated 0-mm radial position. As shown in Fig. 5, this is not the true location of the plume centerline. This deviation from the true centerline position is likely to increase further from the exit plane. Thus the velocity shown in Fig. 12 might be a component of and not the full centerline velocity. This could be corrected by taking data at various radial positions for each axial location. Although

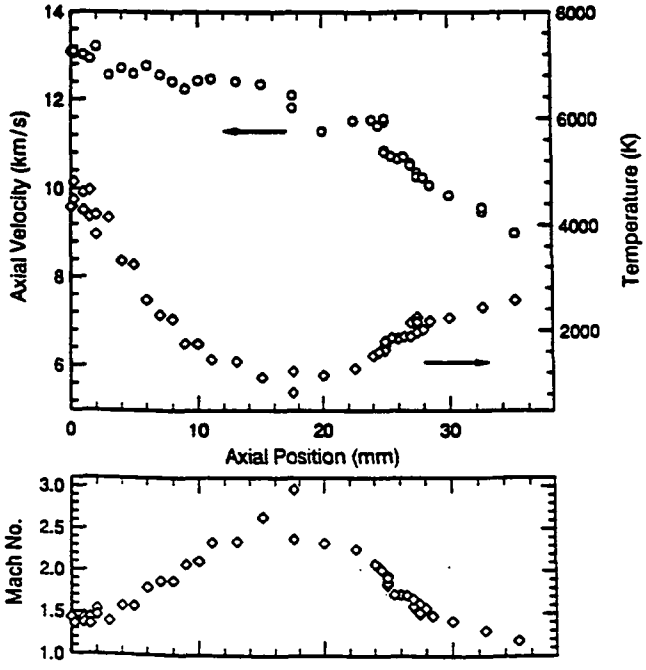

Fig. 12. Axial velocity and temperature taken from a scan along the centerline with constant 1.43-kW input power. The Mach number in the lower graph is derived from the velocity and temperature data and shows the shock at 18 mm.

these gasdynamic property variations are more a function of the background pressure than the plasma dynamics in the nozzle, they do suggest that the flow is underexpanded. Under these circumstances, the exit pressure must be higher than the 0.35-Torr chamber pressure.

A few simple experiments were conducted to determine the presence of polarization of the fluorescence. The fluorescence process is an induced electric dipole phenomenon.[10] Unless there are a significant number of collisions to randomize the orientation of the fluorescing atoms, the fluorescence will be emitted in directions and with polarization reflecting the polarization and orientation of the excitation laser. The laser polarization was rotated while monitoring the variation in fluorescence intensity and line shape. In addition, a polarizing filter was placed in front of the PMT to analyze the fluorescence for preferred polarization. No polarization effects were detected. This indicates that the time between collisions involving excited H atoms is small compared with the lifetime of the transition.

Conclusions

The mean mass exit velocity of the hydrogen arcjet as determined from previous thrust measurements (at the 1.48-kW power level) is 8.3 km/s.[16] This appears consistent with the measured axial atomic velocities. Note that although the 14 km/s peak velocity is significantly higher than the mean mass velocity, the axial velocity drops to 4 km/s at the plume edges. It is likely that the density is not the highest at the centerline, where the temperature and dissociation fractions are high. This interpretation is supported by mass flux profiles determined by sampling probes in similar devices.[17] To fully correlate thrust measurements to velocity data, a measurement of the total density is required as well as a measurement of the (possibly different) velocity distribution of molecular hydrogen. The high radial velocities at the plume edge may represent a significant thrust loss. This effect also would be better quantified by density measurements.

Velocity measurements far from the exit plane (120 mm) have been made with molecular beam sampling mass spectrometry.[18] These measurements suggest the presence of high diffusion velocities for atomic hydrogen. It would be valuable to measure directly the velocity of molecular hydrogen to determine if this diffusion is significant at the exit plane where the pressure (> 0.35 Torr) is several orders of magnitude higher than the 5×10^{-4} Torr near the molecular beam sampling skimmer. There are a multitude of transitions between the excited states of molecular hydrogen that are accessible by cw dye lasers. Future work will include a feasibility study of these transitions for velocity measurements.

At the high peak temperatures measured, the central portion of the plume should consist predominantly of atomic hydrogen. Because the flow chemistry may be partially frozen, equilibrium calculations will give lower bound values of the dissociation fraction. For hydrogen at 8 Torr, the equilibrium composition will vary from one-fourth atomic hydrogen to one-fourth molecular hydrogen over the range 2500 to 3000 K. (Although the exit plane pressure is unknown, an order-of-magnitude change in pressure shifts this dissociation transition range by approximately 300 K.) We conclude that the central area of the plume consists predominantly of atomic hydrogen. The dissociation fraction outside this core is more dependent on the extent to which the flow is frozen. Because the gas at the centerline consists predominantly of atomic hydrogen, the peak atomic hydrogen velocities measured are the same as the peak mean mass velocity.

This paper has demonstrated the utility of spectrally resolved LIF to measure velocity and translational temperature in an arcjet plume. The measurements have provided a variety of information on the nature of the arcjet plume. In summary, we find high peak temperatures, indicating a high dissociation fraction, low swirl velocities, and the presence of diffuse shock structure within 2 nozzle diameters from the exit plane. Even though the arcjet is axisymmetric it would be desirable to make measurements of the complete flow field. If measurements are taken throughout a plane at each axial location, problems that are due to laser–arcjet alignment are eliminated. This would be important for a more rigorous characterization of the arcjet plume.

This research was supported by a grant from the National Aeronautics and Space Administration Lewis Research Center, and Frank Curran was the grant monitor.

References

1. P. J. Wilbur, R. G. Jahn, and F. M. Curran, "Space electric propulsion plasmas," IEEE Trans. on Plasma Sci. **19**, 1167–1179 (1991).
2. M. A. Cappelli, J. G. Liebeskind, R. K. Hanson, G. W. Butler, and D. Q. King, "A comparison of arcjet plume properties to model predictions," paper AIAA 93-0820 in *31st Aerospace Sciences Meeting* (American Institute of Aeronautics and Astronautics, New York, 1993).
3. D. A. Erwin, G. C. Pham-Van-Diep, and W. D. Deininger, "Laser-induced fluorescence measurements of flow velocity in high-power arcjet thruster plumes," AIAA J. **29**, 1298–1303 (1991).
4. J. G. Liebeskind, R. K. Hanson, and M. A. Cappelli, "Velocity measurements in a arcjet using LIF," paper AIAA 91-2112 in *27th Joint Propulsion Conference* (American Institute of Aeronautics and Astronautics, New York, 1991).
5. W. M. Ruyten and D. Keefer, "Characterization of electric thruster plumes using multiplexed laser induced fluorescence measurements" paper AIAA 92-2965 in *28th Joint Propulsion Conference* (American Institute of Aeronautics and Astronautics, New York, 1991).
6. C. E. Moore, "Atomic energy levels," Natl. Bur. Stand. (U.S.) Circ. **467**, 1–8 (1949).
7. R. P. Lucht, "Applications of laser-induced fluorescence spectroscopy for combustion and plasma diagnostics," in *Laser*

Spectroscopy and Its Applications, L. J. Radziemski, R. W. Solarz, and J. A. Paisner, eds. (Dekker, New York, 1987), Chap. 9, p. 627.
8. H. A. Bethe and E. E. Salpeter, *Quantum Mechanics of One and Two-Electron Atoms* (Springer-Verlag, Berlin, 1957), Sec. 64, p. 274.
9. W. G. Vincenti and C. H. Kruger, *Introduction to Physical Gas Dynamics* (Krieger, Malabar, Fla., 1961), Chap. 9, p. 383.
10. W. Demtröder, *Laser Spectroscopy* (Springer-Verlag, Berlin, 1981), Chap. 3, pp. 85–87.
11. C. R. Vidal, J. Cooper, and E. W. Smith, "Hydrogen Stark-broadening tables," Astrophys. J. Suppl. Ser. 214, 37–136 (1973).
12. D. H. Manzella, F. M. Curran, R. M. Myers, and D. M. Zube, "Preliminary plume characteristics of an arcjet thruster," paper AIAA 90-2645 in *21st International Electric Propulsion Conference* (American Institute of Aeronautics and Astronautics, New York, 1990).
13. H. R. Griem, *Plasma Spectroscopy* (McGraw-Hill, New York, 1964), Chap. 4, pp. 95–98.
14. F. M. Curran and T. W. Haag, "An extended life and performance test of a low power arcjet," paper AIAA 88-3106 in *24th Joint Propulsion Conference* (American Institute of Aeronautics and Astronautics, New York, 1988).
15. W. H. Press, B. P. Flannery, S. A. Teukolsky, and W. T. Vettling, *Numerical Recipes in C* (Cambridge U. Press, Cambridge, 1988) Chap. 14, pp. 528–547.
16. F. M. Curran, S. R. Bullock, T. W. Haag, C. J. Sarmiento, and J. M. Sankovic, "Medium power hydrogen arcjet operation," paper AIAA 91-2227 in *27th Joint Propulsion Conference* (American Institute of Aeronautics and Astronautics, New York, 1991).
17. W. M. Van Camp, D. W. Esker, R. J. Checkley, W. G. Duke, J. C. Kroutil, S. E. Merrifield, and R. A. Williamson, *Study of Arc-Jet Propulsion Devices*, Rep. E368 (McDonnell Aircraft Corporation, St. Louis, Mo., 1966); Rep. CR-54691 (National Aeronautics and Space Administration, Cleveland, Ohio, 1966).
18. R. P. Welle, J. E. Pollard, S. W. Janson, M. W. Crofton, and R. B. Cohen, "One kilowatt hydrogen and helium arcjet performance," paper AIAA 91-2229 in *27th Joint Propulsion Conference* (American Institute of Aeronautics and Astronautics, New York, 1991).

N13

Experimental Investigation of Velocity Slip near an Arcjet Exit Plane

J. G. Liebeskind, R. K. Hanson, M. A. Cappelli

Reprinted from

AIAA Journal

Volume 33, Number 2, Pages 373–375

A publication of the
American Institute of Aeronautics and Astronautics, Inc.
370 L'Enfant Promenade, SW
Washington, DC 20024-2518

Experimental Investigation of Velocity Slip near an Arcjet Exit Plane

J. G. Liebeskind,* R. K. Hanson,† and M. A. Cappelli‡
Stanford University, Stanford, California 94305

Introduction

VELOCITY slip is a phenomenon associated with multicomponent flows in which species of different mass have different mean velocities. This phenomenon has been studied in molecular beam nozzles[1] and has been exploited for isotope separation.[2] Significant velocity slip has been measured in the plume of low-power arcjet thrusters.[3] These recent measurements, obtained by mass spectrometry of a molecular beam sampling probe, were limited to locations more than 10 diameters from the exit plane.

The determination of whether slip develops in the nozzle, near the exit plane, or in the expansion plume of an arcjet thruster, is important to both modeling efforts and to the interpretation of measurements. If velocity slip develops inside the nozzle, numerical models will need to include separate momentum equations for each neutral species or, at the very least, an appropriate model for multicomponent transport. These additions increase the complexity of an already difficult task. Measurements of exit-plane velocity in these devices have recently been made by laser-induced fluorescence (LIF),[4] a species specific technique. If significant velocity slip exists, then separate measurements for each species are necessary to completely characterize the flowfield.

We have previously reported LIF-based measurements of atomic hydrogen velocity and kinetic temperature in a hydrogen-fueled arcjet.[4,5] We recognize, however, that the flow consists of both atomic and molecular hydrogen (along with small fractions of ions and electrons). The most direct method to investigate velocity slip in the arcjet flowfield would be to measure, in addition to the velocity of atomic hydrogen, the velocity of molecular hydrogen under the same conditions. As with atomic hydrogen, absorption transitions from the ground state require vacuum-ultraviolet wavelengths. Owing to the low densities of excited-state molecules and the rovibrational distribution which reduces the density of any particular state, these transitions are difficult to probe.

A simpler approach, for the purpose of evaluating slip, is to seed the flow with a species that is accessible with the same laser used to probe atomic hydrogen. In the present study, helium was chosen as the seed species owing to its inertness (with respect to the arcjet nozzle), its relative mass (four times the mass of atomic hydrogen), and its convenient electronic transitions in the visible wavelength region. Velocity and temperature are measured by LIF of both helium and atomic hydrogen at the same arcjet operating condition. Absence of slip between helium and atomic hydrogen would suggest that slip is not a dominant mechanism in the nozzle or exit plane vicinity of our hydrogen arcjet.

Theory

In a multicomponent mixture, each species (denoted by i), may have its own mean velocity v_i, and the mean mass velocity v_m is defined by

$$v_m = \frac{\sum n_i m_i v_i}{\sum n_i m_i} \tag{1}$$

Here, n_i is the number density of species i and m_i is the mass. The simplified steady-state momentum equation for a single species in the axial direction z can be expressed as

$$n_i m_i v_i \frac{\partial v_i}{\partial z} + \frac{\partial p_i}{\partial z} = n_i m_i \sum_j k_{ij}(v_j - v_i) \tag{2}$$

where p_i is the partial pressure. The term on the right side of Eq. (2) represents the momentum exchange between species of different types due to collisions. The momentum exchange term formulated in this way assumes that the force per unit volume exerted on particles of species i, due to collisions with species of type j, is proportional to the difference between their respective mean velocities. The proportionality constant k_{ij}, which accounts for differences in mass of the colliding particles, can be considered a collision frequency for momentum transfer. This constant can be determined from kinetic theory.[6,7] The slip velocity v_{slip} is usually defined for a binary mixture as the difference in velocities,

$$v_{slip} = v_j - v_i \tag{3}$$

If the density is high such that flow is in a continuum regime, the collision rate will be high, allowing efficient momentum exchange between species. Thus, the different species will be in equilibrium, and the slip velocity will be negligible. However, in an expanding flow, conditions can occur in the transition from continuum to free molecular flow, where velocity and pressure gradients are large and the collision rates are low. Insufficient collisions for momentum exchange between species allows a slip velocity to develop. The

Received March 12, 1994; revision received Aug. 10, 1994; accepted for publication Aug. 19, 1994.

*Research Assistant, High Temperature Gasdynamics Laboratory, Department of Mechanical Engineering. Student Member AIAA.

†Chairman, High Temperature Gasdynamics Laboratory, Department of Mechanical Engineering. Associate Fellow AIAA.

‡Assistant Professor, High Temperature Gasdynamics Laboratory, Department of Mechanical Engineering. Member AIAA.

proportionality constant k_{ij} is inversely proportional to the Knudsen number Kn (Ref. 7)

$$k_{ij} \propto 1/Kn \tag{4}$$

As the Knudsen number increases within the continuum regime, momentum transfer between species decreases. However, as the flow becomes rarefied to the extent that collisions become negligible, the slip approaches a constant value (which may be zero) and Eq. (2) is no longer valid. The Knudsen number for this flow has been determined, based on experimental results, to be just under unity.[5] This puts the flow regime in the transition between continuum and rarefied flow.

Experiment

The arcjet thruster used in this experiment is a 1-kW class radiatively cooled thruster designed and built at NASA Lewis Research Center. The tungsten nozzle has a 0.64-mm-diam throat, 0.25-mm-long constrictor, and a conical (20-deg half-angle) diverging section with an area ratio of 225 (9.53-mm exit diameter). A more complete description of the arcjet is available elsewhere.[8,9] When operating on the hydrogen-helium mixture, the current and voltage are 9.5 A and 143 V corresponding to 1.36 kW arc power. The arcjet is operated in a 0.56-m-diam cylindrical stainless steel chamber 1.09 m long. The 0.5-Torr background pressure is maintained by two 35.4 m^3/min coupled to the chamber with 152-mm-diam pipe.

The temperature and velocity measurements were made using LIF. A continuous wave ring dye laser scans across the atomic transition. Since the laser bandwidth is much smaller than the spectral feature, the fluorescence excitation spectrum accurately depicts the broadening mechanisms of the probed species. The velocity is determined from the Doppler shift whereas the temperature is inferred from the shape of the fluorescence excitation spectrum using a Doppler-broadened line-shape model.[4] Since Doppler broadening arises from the velocity distribution of the species, this diagnostic technique probes the kinetic or translational temperature which may differ from the electronic, rotational, and vibrational temperatures of the molecular species in the flow.[10,11] Details of the implementation and analysis have been published previously[4]; the only difference in this experiment is the use of optogalvanic detection in a dc discharge for the helium reference (unshifted) signal. The optogalvanic cell provided a reference for helium with a high signal-to-noise ratio. Fluorescence and absorption in a microwave discharge were used for a hydrogen reference calibration because it provided a stronger signal-to-noise ratio than the optogalvanic technique.

The atomic hydrogen transition probed is the Balmer α transition at 656 nm (15,233 cm^{-1}), an electronic transition between the first and second excited states of H, i.e., $n = 2 \rightarrow n = 3$. This transition actually consists of the overlap of several fine structure components. Since the separation of these components is of the same magnitude as the broadening, the fine structure must be accounted for when analyzing the line shape. The helium transition probed is the $2^1P \rightarrow 3^1D$ transition at 668 nm (14,970 cm^{-1}).

The relatively high energy of helium's first excited state, 166,278 cm^{-1} (20.6 eV) above the ground state can lead to weak fluorescence signals. To obtain a significantly strong fluorescence signal (relative to the noise), a high helium flow rate of 6.2 standard liters/min (SLPM) was necessary. This is significant when compared to the 9.0 SLPM of hydrogen, and hence altered the normal operating conditions of the arcjet. In particular, the addition of helium to the propellant increases the arc voltage and reduces the velocities. The voltage increase of less than 3 V can be explained by a combination of the increased mass flow (due to the helium addition) and helium's higher ionization energy. The 30% velocity decrease (at the centerline) can be attributed to helium's higher atomic mass and the reduced specific power. Also, the peak temperature drops 20% from 5000 K to 4000 K. Although the addition of the helium modifies the flow parameters, the conditions that may lead to slip are expected to be similar to those encountered in the unseeded g arcjet.

Results and Conclusions

The raw data from the helium and hydrogen fluorescence are shown in Figs. 1 and 2, respectively. The Doppler shifts correspond to axial velocities of 10.4 km/s for helium and 10.3 km/s for hydrogen. The magnitude of these measurements is consistent with previous measurements,[4,5] thrust measurements,[8] and model predictions.[12] The hydrogen and helium velocities agree within the 0.2 km/s uncertainty of the measurement. This indicates that the slip velocity is less than the uncertainty of the measurement; i.e., the upper limit of the slip velocity is about 2% of either species' velocity.

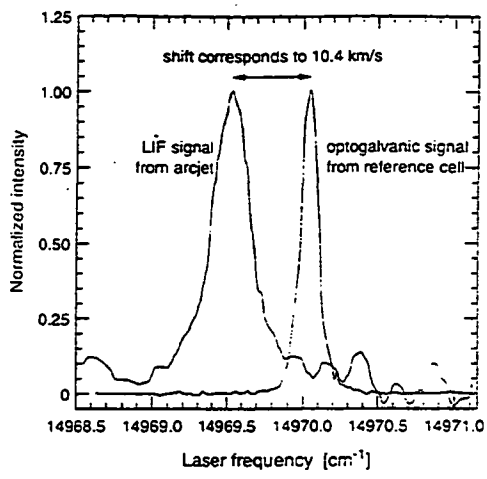

Fig. 1 Doppler-shifted fluorescence excitation spectrum of helium along with the unshifted reference signal used to calibrate the wave meter, probe volume centered in the plume, 0.5 mm from the exit plane.

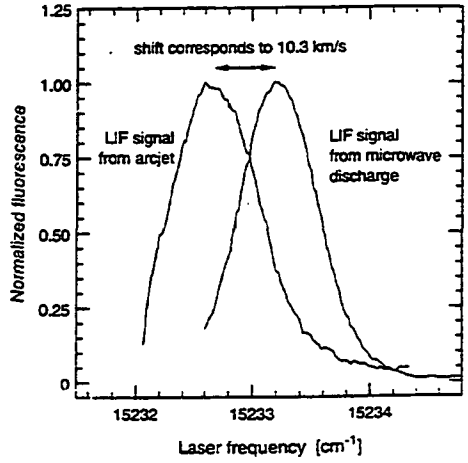

Fig. 2 Doppler shift of atomic hydrogen measured relative to its calibration, measurement location same as the helium data; note the smaller atomic mass leads to broader line widths even though the temperature is the same.

The inferred temperature for helium and hydrogen are 3990 K and 4260 K, respectively. The 6% difference is less than the 20% uncertainty of the measurement. These results allow us to conclude that all species share a common kinetic temperature. Because of the higher sensitivity to noise, the uncertainties of the temperature are higher than the uncertainties of the velocity.

The results indicate that the velocities of atomic hydrogen and helium are the same, suggesting that in the present device, the velocity of any single species, as measured in the vicinity of the exit plane, closely represents the mean mass velocity (within the uncertainty of the measurement). This conclusion is significant because it implies that species specific velocity-measurement techniques such as LIF need only be applied to a single species. In a hydrogen arcjet, it is much easier to probe the atomic hydrogen than the molecular hydrogen, furthermore, it is often easier to probe electronic excited states.

For further investigation of the effect of collisions, it would be interesting to extend these slip measurements further along the axis of the plume to see where slip develops. This extention, however, would require a test chamber capable of maintaining high vacuum

back pressures that would better reproduce the thruster plume structures expected in flight conditions.

Acknowledgments

This work was supported by NASA Lewis Research Center with F. M. Curran as technical monitor. We are grateful to NASA for supplying the arcjet and power processing unit.

References

[1]Miller, D. R., "Free Jet Sources," *Atomic and Molecular Beam Methods Volume 1*, edited by G. Scoles, Oxford Univ. Press, New York, 1988, pp. 41–44.

[2]Mitra, N. K., and Fiebig, M., "Flow in a Laval Nozzle with Gas Mixtures of Disparate Molecular Masses," in *Rarefied Gas Dynamics Volume II*, edited by H. Oguchi, Univ. of Tokyo Press, 1984, pp. 655–664.

[3]Welle, R. P., Pollard, J. E., Janson, S. W., and Cohen, R. B., "One Kilowatt Hydrogen and Helium Arcjet Performance," AIAA Paper 91-2229, June 1991.

[4]Liebeskind, J. G., Hanson, R. K., and Cappelli, M. A., "Laser-Induced Fluorescence Diagnostic for Temperature and Velocity Measurements in a Hydrogen Arcjet Plume," *Applied Optics*, Vol. 32, No. 30, 1993, pp. 6117–6127.

[5]Liebeskind, J. G., Hanson, R. K., and Cappelli, M. A., "Plume Characteristics of an Arcjet Thruster," AIAA Paper 93-2530, June 1993.

[6]Chapman, S., and Cowling, T. G., *The Mathematical Theory of Non-Uniform Gases*, Cambridge Univ. Press, New York, 1970, Chap. 8, pp. 134–150.

[7]Mitra, N. K., Fiebig, M., and Schwan, W., "Quasi-One-Dimensional Nozzle Flows of Disparate Mixtures," *Physics of Fluids*, Vol. 27, No. 10, 1984, pp. 2424–2428.

[8]Curran, F. M., and Haag, T. W., "An Extended Life and Performance Test of a Low Power Arcjet," AIAA Paper 88-3106, July 1988.

[9]Curran, F. M., Bullock, S. R., Haag, T. W., Sarmiento, C. J., and Sankovic, J. M., "Medium Power Hydrogen Arcjet Operation," AIAA Paper 91-2227, June 1991.

[10]Manzella, D. H., Curran, F. M., Myers, R. M., and Zube, D. M., "Preliminary Plume Characteristics of an Arcjet Thruster," AIAA Paper 90-2645, July 1990.

[11]Crofton, M. W., Welle, R. P., Janson, S. W., and Cohen, R. B., "Temperature, Velocity and Density Studies in the 1 kW Ammonia Arcjet Plume by LIF," AIAA Paper 92-3241, July 1992.

[12]Cappelli, M. A., Liebeskind, J. G., Hanson, R. K., Butler, G. W., and King, D. Q., "A Direct Comparison of Hydrogen Arcjet Thruster Properties to Model Predictions," 23rd International Electric Propulsion Conf., IEPC-93-220, Sept. 1994.

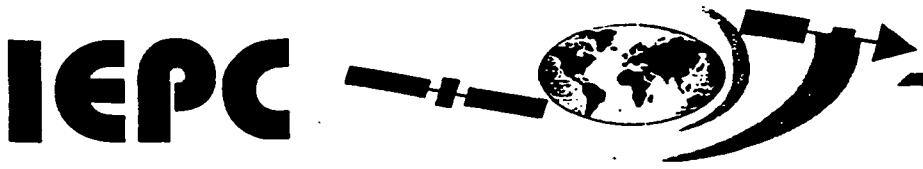

IEPC-93-220

A Direct Comparison of Hydrogen Arcjet Thruster Properties to Model Predictions

M.A. Cappelli, J.G. Liebeskind, R.K. Hanson
High Temperature Gasdynamics Laboratory
Department of Mechanical Engineering
Stanford University
Stanford, California

and

G.W. Butler, D.Q. King
Olin-Rocket Research Company
Redmond, Washington

AIAA • AIDAA • DGLR • JSASS

23rd International Electric Propulsion Conference

Westin Hotel Seattle, WA September 13 - 16 1993

A DIRECT COMPARISON OF HYDROGEN ARCJET THRUSTER PROPERTIES TO MODEL PREDICTIONS

M.A. Cappelli**
J.G. Liebeskind,* and R.K. Hanson‡
High Temperature Gasdynamics Laboratory
Department of Mechanical Engineering
Stanford University
Stanford, California

and

G.W. Butler†† and D.Q. King††
Olin Rocket Research Company
Redmond, Washington

Abstract

This paper describes a detailed comparison of experimentally measured arcjet plume properties to model predictions. The experiments focus on the measurement of the exit plane vector velocity field and kinetic temperature by laser induced fluorescence. The model is based on a single-fluid magnetohydrodynamic description of the flow. Reasonable agreement between model predictions and experimental exit plane velocity profiles is obtained over a wide range of specific power, despite the complex nature of the flow. At higher powers however, there are significant differences between the measured and predicted exit plane temperature. At the highest specific power studied, the model overpredicts the temperature by as much as 2000K and the specific impulse by approximately 20%. These differences cannot be attributed to the present treatment of the collisionless anode sheath or finite-rate molecular recombination (dominant frozen flow loss) and is believed to be more closely related to the treatment of other physical processes such as finite-rate ionization, ambipolar diffusion or possibly the selection of exit plane boundary conditions. These findings suggests that further refinements in the treatment of these processes may be necessary in order to extend the predictive capabilities of the model.

I. Introduction

Arcjet thrusters are high specific impulse electric propulsion devices that are presently targeted for use in stationkeeping and orbit transfer.[1] In comparison to other propulsion alternatives such as low-thrust chemical rockets, the use of arcjets will enable smaller launch vehicles for payload delivery because of the significant savings in propulsion system mass.

Much emphasis has been placed recently on the development and flight qualification of low power (<2 kW) hydrazine arcjet thrusters.[2-4] However, in order to meet a wider range of mission possibilities, arcjet operating ranges must be extended to higher powers (2 - 30 kW). Although much progress has been made in this direction through extensive laboratory studies, [5-7] it is now evident that scaling to higher powers will require a better understanding of the physical processes that control arcjet performance. These include: (i) the physics of arc root attachment at both the cathode and the anode; (ii) the processes that establish the local plasma conductivity (i.e., ionization, ambipolar diffusion of charged species); (iii) the dissipation of energy via Joule heating, the subsequent transport of this energy to the internal surfaces of the arcjet, and the conduction of energy away from these internal

---

* Research Assistant, Student Member AIAA
** Assistant Professor, Member AIAA
‡ Professor, Member AIAA
†† Member, AIAA

surfaces; (iv) the magneto-hydrodynamic coupling of the flowfield to the electrical nature of the arc, and; (v) processes such as dissociation and vibrational excitation, which give rise to frozen flow losses and reduce thrust efficiencies.

To better understand these processes, studies that include a combination of modeling and laboratory measurements are necessary. The data base generated by the experiments must extend beyond thrust and energy balances, and should be capable of resolving detail at the level predicted by the computations (i.e., capable of measuring velocity components, translational, rotational or vibrational temperatures, neutral species and electron number densities).

This paper describes our continued effort to develop and validate computational models of arcjet performance by way of direct comparison to detailed measurements of flow properties. We have selected a nominally 1 kW class hydrogen arcjet thruster as a benchmark for this comparison. Unlike ammonia arcjet flows, the chemical composition is relatively simple, and the transport properties and chemistry are better known. Furthermore, hydrogen is a strong contender as a propellant for future arcjet demonstration missions.[1]

The numerical results presented here are based on a single-fluid model that has been developed at Olin-Rocket Research Company.[8,9] The experimental data are obtained from facilities in the High Temperature Gasdynamics Laboratory at Stanford University. Details of both the numerical model and experiments are available in other papers.[8-12] In this paper, we shall only discuss the sensitivity of the model to parameters which influence some of the physical processes described above, such as its sensitivity to changes in electron-ion and atomic hydrogen recombination rate coefficients. In a previous paper,[13] we performed a detailed comparison of experimental measurements of flow properties taken at a nominal power (1.5 kW) to properties predicted by the numerical model. Our focus here is to extend this comparison over a range of specific power.

A brief description of the single-fluid model is given in Section II. An overview of the experimental facility is described in Section III. A detailed comparison between experimental results and model predictions is presented in Section IV. A discussion of this comparison and an analysis of the model's sensitivity to chemical rate coefficients is given in Section V. A summary of this study and conclusions are given in Section VI.

II Single-Fluid Model

The single-fluid model is based on a solution of the axisymmetric Navier - Stokes equations coupled to relations which govern the behavior of the magnetic and electric fields, as formulated within the magnetohydrodynamic (MHD) approximation.[14] The model tracks the relative mole fractions of the various species which comprise the mixture by solving individual species conservation equations that include source terms for the net production of species via chemical reactions. The model considers a mixture that includes atomic and molecular hydrogen (H, H_2), electrons (e), and protons (H^+). Table I summarizes the chemical reaction set and nominal values of the reaction rate coefficients (in modified Arrhenius form) used in the calculations. Reverse reactions are computed as required by using detailed balance and curve fits (in JANNAF format[15]) to the high temperature thermodynamic properties derived from spectroscopic data.[16]

In the present study, diffusive transport is neglected. This simplification is expected to significantly affect the calculations of the electrical conductivity, σ, in colder regions of the flow and is discussed in more detail later in the paper. Neglecting the diffusion of neutral species, such as the slip velocity between atomic hydrogen and molecular hydrogen may be a more reasonable approximation, especially in the low density nozzle. Recent velocity measurements of atomic hydrogen and seeded helium at the exit plane of a 1 kW arcjet verified that slip velocities between species in the flow may indeed be negligible.[17]

In the formulation, the global momentum includes the Lorentz force associated with self-generated magnetic fields. Body forces associated with excess free charge (space charge) are neglected within the MHD approximation. Quasi-neutrality is assumed throughout the flow. The global energy equation includes Joule heating. The required transport coefficients (thermal conductivity, viscosity, electrical conductivity) are computed from the species mole fractions, collision integrals and mixture rules as provided by Yos.[18]

The magnetic field, $\vec{B}$, is computed from the

magnetic induction equation in the steady-state approximation[14]

$$\nabla \times \vec{u} \times \vec{B} - \nabla \times \left[\eta \left(\nabla \times \vec{B} \right) \right] = 0 \qquad (1)$$

In writing Equation (1), we have neglected the contributions associated with ion-slip and the Hall effect. In the above equation, $\vec{u}$ represents the mean mass velocity of the flow and $\eta = 1/\mu_o \sigma$ is a measure of the plasma resistivity. A detailed derivation of Equation (1) can be found in Reference 14. The current density is derived from the computed magnetic field using Ampere's law.

The importance of the Hall effect is determined by the Hall parameter[14] (product of electron cyclotron frequency and mean collision time for electrons and ions and electrons and neutral species). The Hall parameter is less than unity for conditions anticipated in the arcjet. Ion-slip is generally unimportant in highly-ionized plasmas, and is only significant in weakly-ionized plasmas when the Hall parameter is much greater than unity.

For boundary conditions, we assume a no slip condition for velocity and zero flux condition for species number densities at the electrode surfaces. For temperature, we couple the heat flux at the electrode surface to a model of heat transfer within the anode. Heat transfer to the cathode is neglected. The model systematically calculates the temperature distribution and flux condition on the internal and external surface of the anode. Only the nozzle of the complete anode structure is modeled. A specified heat flux or temperature distribution is required at the boundary where the anode/nozzle joins with the rear arcjet housing. In general, this boundary condition is found to have a small effect on the predicted arcjet performance. Constraining the current to a direction normal to the anode at the anode surface acts as a condition on the the gradient of the magnetic field on this boundary. At the exit plane, we assume that the magnetic field is zero. The flow is assumed to be axisymmetric, and so we solve only for the azimuthal component in the magnetic field.

As mentioned above, we believe that the single fluid model is not capable of accurately predicting the near-electrode plasma properties and therefore the near-electrode conductivity. In the vicinity of the cathode or anode, property gradients are high and ambipolar diffusion will create an overpopulation of electrons and ions in this region. Furthermore, we expect an elevated electron temperature, since electron thermal conduction is very efficient and thermalization between electrons and neutral species occurs at a finite rate. Since the single-fluid model used here does not account for these effects, the model will underpredict the electron number density, and in turn, over predict the Joule heating rate (per unit volume), $P_\Omega = \vec{J} \cdot \vec{J}/\sigma$. In order to compensate for this, a minimum value of the near-electrode conductivity is imposed. This conductivity "floor", σ_{min}, is found to have a dramatic effect on the computed arcjet behavior. In particular, we find that the value selected for the conductivity floor greatly influences the computed arc voltage. For this reason, a value of σ_{min} is selected to provide reasonable agreement between the computed and measured discharge voltage over a wide range of power to mass flow rate ratio, $P/\dot{m}$. Typical values of σ_{min} correspond to electron number densities of approximately 10^{10} cm^{-3}. This value is approximately ten orders of magnitude lower than the electron number densities predicted in the core of the arc. The fact that the computed arcjet performance depends so critically on this value further emphasizes the need to include a self-consistent treatment of the plasma behavior in the near-electrode region of the arcjet. A proposed self-consistent treatment of the quasi-neutral, near-electrode region in arcjet thrusters has been recently described in the literature.[19,20]

The computed arcjet voltage reflects the resistive contribution to the plasma conductivity, as constrained within the quasi-neutral assumption. As a result, the single-fluid quasi-neutral model does not formally treat and therefore capture the structure of the non-neutral sheath. The space charge generated in the immediate vicinity of the electrodes (within a distance of the order of a Debye length) gives rise to an additional voltage drop. In the case of a collisionless anode sheath, this may represent an additional mechanism for heat transfer to the anode. We use a simple model to arrive at an estimate of the anode sheath potential, Φ_s. We shall assume that the sheath is collisionless (valid in low pressure regions of the nozzle, when the mean free path, λ, is much greater than the Debye length, λ_D), and that the anode fall is strongly positive relative to the potential of the distant plasma. Furthermore, we shall assume that the total current, J, is carried by the electrons within the space charge region, and that it is approximately equal to the one-way random electron flux at the sheath-plasma

boundary. Under these conditions, the voltage drop across the sheath is described by Child's law,[14] and is given here as

$$\Phi_s^{3/4} \approx \frac{3}{2}\left[\frac{J}{\varepsilon_o}\left(\frac{m_e}{2e}\right)^{1/2}\right]^{1/2} d_s \qquad (2)$$

Here, ε_o is the permitivity of free space, e is the magnitude of the elementary charge, m_e is the electron mass, and d_s is the sheath thickness, which for a collisionless sheath, can be as large as the electron mean free path, λ_e. For conditions near the arcjet constrictor, we estimate $\lambda_e = 3 \times 10^5$ m. If we assume that the current density to the anode is of order 10^5 A/m^2, equation (2) above gives a maximum value of $\Phi_s \approx 13$V. For the results presented here, the sheath voltage is taken to be constant over the entire anode surface and the total power , $P = I \cdot \Phi_s$, is assumed to be driven entirely into the anode. The power lost in the anode sheath is added to the power dissipated through Joule heating to arrive at the total electrical power invested into the device.

We note that this simple treatment of the plasma sheath is invalid when the densities are sufficiently high to render the sheath collisional. Under these conditions, a self-consistent multi-fluid treatment of a collisional sheath in a flowing plasma may be necessary.[20]

The governing single-fluid equations are integrated using a finite-volume algorithm originally developed for magnetohydrodynamic flows at Los Alamos National Laboratory.[21] A discussion of the numerical method may be found in References 8 and 9. Its original capabilities have been extended by Olin-Rocket Research Company to include finite rate chemistry, high temperature transport properties, radiative losses, and thermal conduction. The computational grid includes the region within the arcjet plenum, throat, and nozzle. The domain extends to the nozzle exit plane. The model therefore accurately predicts the internal flowfield of the thruster, but is incapable of modeling expansion waves immediately downstream of the nozzle exit plane.

Although there are some obvious limitations to this model described here, it offers a framework on which to construct multi-fluid models.[9] Furthermore, it provides an opportunity to guide the design of higher power thrusters. The usefulness of the single-fluid and a extended two-fluid model in describing the performance of a 10 kW hydrogen arcjet thruster has been previously described.[9]

III. Experiment

The arcjet thruster used in the experiment is a 1 kW class radiatively-cooled laboratory-type thruster designed and built at NASA Lewis Research Center. The tungsten nozzle has a 0.635 mm diameter throat and a conical (20° half angle) diverging section with an area ratio of 225 (9.53 mm exit diameter). A more complete description of the arcjet design is available elsewhere.[2] Baseline operating conditions are 13.7 mg/s of H_2 propellant with a maximum power dissipation of 1.5 kW (voltage and current levels of 148 V and 10.1 A respectively). Some measurements were also performed at slightly lower mass flow rates (13.1 mg/s). At these propellant mass flow rates, it is possible to achieve stable operation at powers as low as 650 W. The arcjet is operated in a 0.56 m diameter cylindrical stainless steel chamber 1.09 m long. The 0.35 Torr background pressure is maintained by two 1250 cfm blowers evacuating through 6 inch diameter pipe.

The experimental data of plume velocity and translational temperature is obtained by laser-induced fluorescence (LIF) excitation of the Balmer -α transition of atomic hydrogen. In employing LIF, a laser probe is focused to a small diameter in the arcjet plume. Subsequent fluorescence from excited atomic hydrogen is collected and imaged onto a detector. Flow properties are determined from the way in which the fluorescence signal varies with the laser frequency (wavelength). This spectroscopic technique has several advantages. It is non-intrusive, and measurements can be made in the vicinity of the exit plane where solid probes would fail due to the high-enthalpy nature of the flow. In addition, the ability to focus the probe laser to small sizes allows for high spatial resolution. Having high spatial resolution (approximately 100 mm) is particularly important in low power arcjets where large variations in velocity and temperature occur across the small, 1 cm diameter of the nozzle exit.

Velocity is determined from the Doppler shift of the fluorescence excitation spectrum. The translational temperature is determined from the shape of the fluorescence excitation spectrum. In

contrast to velocity, the temperature is more difficult to infer due to competing mechanisms which act to broaden the measured profile as well as the complex nature of the overlapping line components. For conditions present in the arcjet plume, the Balmer-α transition is primarily Doppler broadened and has a Doppler width that is much larger than the laser bandwidth. As a result, the shape of the recorded fluorescence spectrum accurately depicts the excited state velocity distribution function. The excited state atomic hydrogen is assumed to be in translational equilibrium with the ground state species. Details of the diagnostics have been presented previously.[10,11]

A schematic of the experimental setup is shown in Figure 1. The fluorescence excitation laser is a CW ring dye laser (Spectra Physics Model 380) pumped by a 6 W argon-ion laser and operating on DCM dye. It produces several hundred milliwatts of power at 15,233 cm^{-1} (656 nm) with a nominal bandwidth of 10 MHz. Part of the laser beam is passed through a 2 GHz Fabry-Perot interferometer to monitor mode structure and ensure single mode operation. Another portion of the beam is directed into a wavemeter (Burleigh WA-10) which uses a Michelson interferometer to measure laser frequency to within 0.01 cm^{-1}. A third beamsplitter directs the laser to a photodiode detector which monitors laser power.

A beamsplitter divides the laser into two beams of approximately equal intensity. One beam is for axial excitation and the other is for radial excitation. The beams are expanded and then focused through windows to a waist of 0.1 mm in the arcjet plume. The radial excitation beam is passed vertically through the plume. This allows the fluorescence signal to be collected on a horizontal axis normal to both excitation beams. It is collected through an 83 mm diameter window with a lens operating at f/5.7 (76 mm diameter, 280 mm focal length) and imaged onto a R928 photomultiplier tube (PMT) with a magnification of 2.7. A notch filter with a nominal 10 Å (23 cm^{-1}) bandwidth is placed directly in front of the PMT to filter extraneous light other than that from the transition of interest. A 0.4 mm aperture is mounted directly in front of the filter at the focal plane of the imaging lens to act as a field stop and determine the measurement location in the plume as well as the axial and vertical spatial resolution. Phase sensitive detection is used to discriminate the fluorescence signal from the background emission which is 30 to 500 times greater. The lock-in amplifier (SRS SR530) is synchronized to a mechanical chopper at 3 kHz. The output from the lock-in is collected and stored in a laboratory computer along with the output from the wavemeter and laser power detector.

At each spatial point investigated the laser is automatically scanned in frequency by varying the voltage on a (piezo-controlled) 75 GHz intracavity etalon. Radial and axial excitation scans are performed on separate scans by blocking one of the beams. The laser is able to scan over a range of up to 2 cm^{-1}, enough to capture most of the fluorescence excitation line. For adequate signal to noise, scan times are a few minutes in duration.

For a stationary (unshifted) reference, both the arcjet itself and a stationary hydrogen discharge were used. It is assumed that the flow is axisymmetric which implies that the radial velocity is zero at the centerline. The symmetry of both the axial and radial velocity profiles confirms this assumption. The wavemeter provides enough accuracy and repeatability to forego simultaneous reference scans. The stationary discharge was produced in a low pressure hydrogen cell mounted in a microwave cavity which acted as a source of H atoms with essentially zero average velocity.

The velocity and temperature are determined by a least squares fit to the lineshape model using the Levenberg-Marquardt method.[22] The model consists of the five components associated with the fine structure of the probed transition, with specified relative intensities and separations.[11] Doppler broadening is the only broadening mechanism considered. There are three parameters that are used to fit the data to the model: Gaussian halfwidth, line shift, and magnitude. The temperature is determined from the Gaussian halfwidth. The velocity is determined from the shift. The magnitude was necessary to fit the other parameters but can also be used to determine relative excited H atom densities.

The effect of saturation was evaluated by comparing LIF line profiles for a range of laser-power levels. For the 0.1 mm laser spot size, the fluorescence was found to be linear below 60 mW. Thus all data was taken with laser powers well below this level.

Two typical fluorescence excitation scans are

shown in Figure 2. The scan on the left is taken from the plume centerline 0.4 mm from the exit plane with axial excitation where the measured temperature is 4500 K. The scan on the right is from the colder, 600 K reference cell. At temperatures below about 1000 K, the Balmer-α lineshape begins to look more like a doublet. This is due to the fine structure discussed briefly in the previous section and in more detail elsewhere.[11] The solid lines correspond to the model's fit to the data. The fluorescence intensity is the ratio of the output signal from the lock-in amplifier to the signal from the photodiode which monitors laser power. Accounting for laser power in this way preserves the lineshape since the fluorescence is linear and not saturated. The power varies by up to 10% as the laser scans in frequency. Both profiles were normalized by their areas to facilitate comparisons of the lineshapes between the hot and cold gases. These profiles consist of 70 to 200 data points each, with the data taken at one second intervals. Profiles from regions further from the centerline require longer scan times due to decreased signal-to-noise ratios.

IV. Results

As described in Section II above, a-priori knowledge of the current-power operating characteristics of the arcjet was necessary in order to establish a value of the conductivity "floor", σ_{min}. Figure 3 shows the measured and predicted variation in operating current versus operating power for a specific power of 90 MJ/kg and three values of the conductivity floor. For a single conductivity floor, we find that the predicted current-power characteristics are best modelled by a value of σ_{min} = 4.07 mho/m. We note however, that use of a single value of σ_{min} may be inappropriate, as it is evident in the figure that this value of σ_{min} over predicts the arc current at low arc powers, and underpredicts the current at high arc powers, over the range of powers studied here. In general, use of a single value of σ_{min} = 4.07 moh/m can result in a 25-30% overprediction or underprediction of the arcjet operating voltage for a given specific power. In order to more accurately model the current-power characteristics, we use a variable σ_{min} that is quadratically dependent on the arcjet power:

$$\sigma_{min} = -3.969 + 11.529P - 4.099P^2 \quad moh/m$$

where P is the arcjet power in kilowatts.

We also note that although a power dependent value of σ_{min} is employed in the computation for the range of specific powers studied here, a more appropriate model for the current-power characteristics would include a mass flow dependence on σ_{min} (i.e., a dependence on specific power). The dependence on specific power is not included in this study, and we assume that over the range of specific powers investigated here, adjustments in the value of σ_{min} are insignificant.

In the simulations, a value of Φ_s =13V is taken for the anode sheath voltage. This value is found to accurately reproduce the performance characteristics of a 10kW hydrogen arcjet[9] and is approximately that estimated by Child's Law when the collisionless sheath thickness approaches the electron mean free path. The sensitivity of the computed arcjet performance to values of the sheath voltage drop is discussed in Section V.

For the calculations presented here, we have assumed an adiabatic boundary condition for the surface where the nozzle assembly is attached to the remaining arcjet structure. Although this assignment is somewhat arbitrary, we find that on the basis of a comparison to calculations that employ an isothermal condition of 1000K, the computed flow properties are only weakly sensitive to this boundary condition.

Unless otherwise stated, the experimental measurements presented here are for hydrogen mass flow rates of 13.7 mg/s. This is approximately 7% higher than the mass flow rate used for earlier comparisons to model predictions.[13] Figures 4 - 6 compare the computed and measured exit plane velocities and kinetic temperature for values of specific power, $P/\dot{m}$ =64, 73, and 110 MJ/kg. In all cases, there seems to be good agreement in magnitude and in profile shape (near the jet core), between the model predictions and experimental measurements of exit plane axial velocity (see Figure 4). The systematic differences between the model predictions and experimental results in the regions close to the nozzle wall may be indicative of additional post-nozzle flow expansion that is not simulated by the model. We note that the measurements are made with a finite spatial resolution (0.1 mm) approximately 0.4 mm from the true exit plane and may capture the gasdynamic behavior in the region

of the nozzle lip. The differences however, are within the experimental uncertainties. The increased uncertainty in the measured velocity as one moves outwards from the central arcjet axis arises from the concomitant drop in signal as a result of the dramatic drop in excited state number density.

As can be seen from Figure 5, there is reasonable agreement between the simulated and measured spatial variation in the radial velocity component for the range of specific powers studied. Positive and negative values in Figure 5 represent data taken at positions extending across the entire arcjet plume. Since the laser is directed downwards with respect to the laboratory reference frame, a negative velocity implies downward motion and is not to be confused with motion of the flow along a direction towards the arcjet axis. The measured radial velocities are found to vary nearly linearly with increasing distance from the arcjet axis. The measured velocities are in satisfactory agreement with model predictions near the arcjet exit plane core. However, we find that there is a noticeable difference between model predictions and experimental measurements made at positions far from the plume axis. We emphasize again however, that the model forces the radial velocity component to zero for the internal flowfield calculation in order to invoke a no-slip boundary condition. In fact, additional gasdynamic effects near the lip of the nozzle may be captured in the measurements of the radial velocities. It is noteworthy that both the measurements and calculations indicate that the radial velocities are only weak functions of the arcjet specific power. Also, the magnitude of the radial velocity reaches approximately 4 km/s for the highest specific power studied. This occurs near the nozzle lip, where the measured axial velocity is of the same magnitude thus implying a 45° flow direction at this spatial location.

As can be seen from Figure 6, a significant difference between model predictions and experimental measurements of exit plane temperature is evident, both in magnitude and in profile shape. In particular, we find that the discrepancy increases with increasing specific power.

These results are consistent with earlier comparisons[13] of the measured and predicted centerline axial velocity and temperature variation with specific power. These earlier data are presented in Figure 7. As can be seen in Figure 7, good agreement between simulations and experiment was obtained for centerline values of temperature at relatively low specific powers (50 MJ/kg), however, rather poor agreement (factor of two difference) was obtained at the higher values of specific power (110 MJ/kg). Both the measurements and simulation clearly indicate that when the input power is more than doubled, the centerline velocity increases by only 30%. This is consistent with the observed variation in thrust with changes in operating power[2] for medium power hydrogen arcjet thrusters. The experimental results also indicate that the kinetic temperature increases by a factor of three over the range of powers studied. At higher powers, there is an increased fraction of the enthalpy convected out the nozzle. The increased specific impulse therefore comes at the expense of thrust efficiency (defined here as $g^2 I_{sp}^2 P / 4\dot{m}$). Figure 8 shows the computed variation in both the specific impulse and efficiency with arcjet power at a constant mass flow rate of 13.1 mg/s. Although the computed thrust efficiency is seen to decrease with increasing specific power, the experimental measurements suggest that the efficiency must fall more precipitously to account for the considerable rise in exit plane temperature.

The measurements of temperature are based on the measurements of Doppler broadened fluorescence excitation profiles and are found to be very sensitive to the baseline fitting procedure.[11] The experimental uncertainty is greater for temperature than it is for velocities, and is reflected in the scatter in the experimental data. Despite the increased uncertainty, we find that the discrepancy between measurements and model predictions lies outside of the expected experimental uncertainty in temperature for the higher specific power cases. For the highest specific power investigated here, we find that the model underpredicts the temperature by at least 50% over a good portion of the arcjet radial domain ($r < 2$ mm). The reason for this difference is speculated on in Section V. There has been some question raised[23] as to wether the excited electronic state that is probed in these experiments is produced with excess kinetic energy resulting from dissociative recombination. This is certainly possible, although it should be noted that for the highest specific power case, the model significantly overpredicts the specific impulse (about 1000s), which, for conditions close to that of the high specific impulse case, has been

measured to be approximately 830 s.[6] An overprediction of 20% in the I_{sp} is consistent with the observed difference in the measured and computed temperatures.

Although measurements of exit plane electron number density and ground state atomic hydrogen number densities under the above mentioned conditions have not been made, it is noteworthy that the predicted centerline values, which can be inferred from the predicted radial variation as shown in Figure 9, are consistent with measurements previously reported in the literature. For a specific power of 113 MJ/kg and a mass flow rate of 13.1 mg/s, a centerline exit plane electron number density of 10^{20} m^{-3} falls within the centerline value of 10^{19} m^{-3} reported by Manzella[24] at a downstream location of 1 cm, and a centerline value of 10^{21} m^{-3} reported by Zube,[25] 1 cm upstream of the exit plane inside the expansion nozzle. More recent measurements[26] of the electron number density in the arcjet throat indicate that the axial electron number densities are 2-5 times higher than that predicted for the highest specific powers studied. Centerline values of the ground state atomic hydrogen 2 cm from the exit plane as high as 5×10^{18} m^{-3} have been reported,[27] indicating that additional plume expansion or hydrogen recombination may be taking place within a very short distance of the exit plane.

V. Discussion

Although the single fluid model predictions and measurements of arcjet velocities compare favorably, the differences observed between predictions and measurements of exit plane temperatures at higher specific powers (> 75 MJ/kg) suggest that some features of the model require further refinement. It is apparent that there is a systematic underprediction of the exit plane temperature. This result is consistent with the overprediction of specific impulse, based on measurements made on similar thrusters at NASA Lewis. We find that these differences cannot be accounted for by refinements in the anode (internal) heat transfer model. Instead, we believe that there are physical processes that are either not included in the model (i.e., ambipolar diffusion), or are included but not accurately represented (i.e., ionization), which must account for the observed differences in predicted and measured arcjet performance. It is apparent that there is an underprediction in the dissipated power, and therefore an underprediction in the exit plane temperature. Part of the discrepancy may be accounted for by the simplified treatment of the anode sheath. We used here an upper limit to the sheath potential, Φ_s, of 13V, which represents a 10% loss of power to the arcjet anode. According to the experimental data, increasing the dissipated power by this amount (i.e., assuming no electrical power loss to the anode) can lead to as much as a 1000 K increase in the exit plane centerline temperature. It is important to note however, that it the model predictions that does not reflect such a trend in that a 10% increase in power raises the temperature by a mere 300 - 400 K.

The electron third-body recombination rate used here is representative of that estimated for a strongly recombining low temperature (i.e., 3000-4000 K) plasma[28]. The conditions in the constrictor of the arcjet are that of a high temperature (> 30000 K) ionizing plasma. A proper treatment of the ionization/recombination processes would require the coupling of a collisional-radiative model to the flow calculations. At this time, such an addition to the model would be prohibitively expensive from a computational standpoint. If the rate presently employed is too low, then the ionization rate calculated from detailed balance will also be low. This will result in too low a constrictor electron number density (as is observed[26]), and hence too low a conductivity. A low conductivity will give rise to a relatively high voltage drop over a shorter distance (for the same current density) and hence a shorter arc length. In order to increase the flow temperature (decrease the thrust efficiency) we must therefore increase the recombination rate that is employed in the simulation so that the arc penetrates further into the supersonic region of the expanding flow. Simulations were performed for values of 10 and 100 times that of the nominal recombination rate coefficient that is used, for the highest arcjet specific power studied. The results of this computational study indicate that changes of such magnitude have only a marginal influence on the exit plane temperature. More dramatic differences between the true electron-ion recombination rate coefficient and that employed here would be necessary to account for the differences in the measured and predicted exit temperature.

Perhaps a more important process not accounted

for in the model is species diffusion. In the single-fluid model, this can be accounted for to first order by the addition of diffusive fluxes for both neutral and charged species (ambipolar diffusion). Because of the significant temperature gradients that can exist in the arcjet constrictor (10^8 K/m), it is necessary to include thermal diffusion. A more rigorous treatment of the decoupled electron, ion, and neutral species dynamics would require the addition of an appropriate momentum equation for each plasma constituent. Such multi-fluid models would permit the diffusion of electrons and ions into colder regions of the constrictor and nozzle, thereby elevating the local plasma conductivity, and removing the need to artificially impose a conductivity "floor" in the region near the nozzle wall.

The extension of the single fluid model to two fluids has been previously described.[9] A two fluid model, with the electrons distinguished from both the neutrals and ions, would allow for the possible departure from local thermal equilibrium. In the two fluid model, energy is added to the electron pool through Joule heating, and is transferred to the heavier species by both elastic and nonelastic processes (ionization, dissociation). An elevated electron temperature is established, especially near the anode, due to the more efficient conduction of electron energy across regions of the plasma where steep temperature gradients may exist. This two-temperature nonequilibrium would also help in maintaining an elevated plasma conductivity, and would therefore also result in an increase in arc length and therefore decrease in nozzle performance or thrust efficiency.

In general, we find that the differences in measured and predicted exit plane temperature cannot be accounted for by uncertainties in atomic hydrogen recombination rate coefficients. We find that a large (i.e., order of magnitude) change in the rate coefficients for third-body enhanced recombination of atomic hydrogen ($H + H + M \rightarrow H_2 + M$) has only a minor influence on the calculated exit-plane temperature field and arcjet performance. This indicates that frozen flow losses associated with finite-rate molecular recombination processes are difficult to recover under present arcjet design constraints.

At present, the computational domain is limited to the exit plane of the arcjet. We impose a zero magnetic field constraint on this boundary. This boundary condition is expected to influence the current distribution within the nozzle. It is well known that the arc attachment points extend well beyond the constrictor and into the expanding portion of the anode/nozzle in these low power arcjet thrusters.[29] Constraining the magnetic field to be zero at the exit plane may limit the extent to which the arc penetrates out from the constrictor and therefore constrain the ohmic dissipation to the subsonic portion of the flow thereby increasing the nozzle performance.

VI Summary and Conclusions

In this paper, we have described a detailed comparison of experimentally measured low power hydrogen arcjet plume properties to model predictions. The experiments focus on the measurement of the exit plane vector velocity field and kinetic temperature by laser induced fluorescence. The model is based on a single-fluid magnetohydrodynamic description of the flow. Excellent agreement between model predictions and experimental exit plane velocity profiles is obtained over a wide range of specific power, despite the complex nature of the flow. At higher powers however, there is significant difference between the measured and predicted exit plane temperature. The model overpredicts the temperature by as much as 2000K. These differences cannot be attributed to the present treatment of the collisionless anode sheath or finite-rate molecular recombination (dominant frozen flow loss) and is believed to be more closely related to the treatment of other physical processes such as finite-rate ionization, ambipolar diffusion or possibly the selection of exit plane boundary conditions.

The simulations overpredict performance (I_{sp}) at the higher specific powers studied. This overprediction in performance is consistent with the underprediction in temperature and implies an overprediction in the thrust efficiency or nozzle performance. The thrust efficiency is shown to be only marginally sensitive to order of magnitude changes in the value of the electron third-body recombination rate coefficient that is employed in the simulation. However, little data is available as to what value of this rate coefficient is appropriate. This suggests that further refinements in the treatment of finite-rate ionization and species diffusion in these thrusters may be necessary in order to extend the predictive capabilities of the

model.

Acknowledgments

The Stanford contribution to this study was supported by NASA Lewis Research Center with F. Curran as the contract monitor, and in part by Olin-Rocket Research Company.

References

1. P.J. Wilbur, R.G. Jahn, and F. Curran; Space Electric Propulsion Plasmas," IEEE Transactions on Plasma Science, Vol. 19, No 6, pp. 1167-1179, December, 1991.
2. F.M. Curran and T.W. Haag; "An Extended Life Test and Performance of a Low Power Arcjet." AIAA 88-3106, 24th Joint Propulsion Conference, Orlando Florida, July 1988.
3. S.K. Knowles, S.E. Yano, and R.S. Audland, "Qualification and Liftesting of a Flight Design Hydrazine Arcjet System," AIAA 90-2576, July 1990.
4. W.W. Smith, R.D. Smith, K. Davies, and D. Lichtin, "Low Power Hydrazine Arcjet System Flight Qualification," IEPC-91-148, 22nd International Electric Propulsion Conference, Viareggio, Italy, October, 1991.
5. W.E. Morren and F.M. Curran, "Preliminary Performance and Life Evaluations of a 2 kW Arcjet," AIAA 91-2228, 27th Joint Propulsion Conference, Sacramento, June 1991.
6. F.M. Curran, R. Bullock, T.W. Haag, C.J. Sarmiento, and J. M. Sankovic, "Medium Power Hydrogen Arcjet Operation," AIAA 91-2227, 27th Joint Propulsion Conference, Sacramento, June 1991.
7. B. Glocker, Th. Rosgen, and A. Laxander, "Medium power Arcjet Analysis and Experiments." IEPC 91-016, 22nd International Electric propulsion conference, Viareggio, Italy, October 1991.
8. G.W. Butler, B.A. Kashiwa, and D.Q. King, "Numerical Modeling of Arcjet Performance," AIAA 90-1474, 21st Fluid Dynamics, Plasmadynamics, and Lasers Conference, Seattle, WA, June 1990.
9. G.. Butler and D.Q. King, "Single and Two-Fluid Simulations of Arcjet Performance," AIAA 92-3104, 28th Joint Propulsion Conference, Nashville, TN, July 1992.
10. J.G. Liebeskind, R.K. Hanson, and M.A. Cappelli, "Velocity Measurements of a Hydrogen Arcjet Using LIF," AIAA 91-2112, 27th Joint Propulsion Conference, Sacramento, CA, June 1991.
11. J.G. Liebeskind, R.K. Hanson, and M.A. Cappelli, "Flow Diagnostics of an Arcjet Thruster Using Laser Induced Fluorescence," AIAA 92-3243, 28th Joint Propulsion Conference, Nashville, TN, July 1992.
12. J.G. Liebeskind, R.K. Hanson, and M.A. Cappelli, "Plume Characteristics of an Arcjet Thruster," AIAA 93-2530, 29th Joint Propulsion Conference, Monterey, CA, June, 1993.
13. M.A. Cappelli, J.G. Liebeskind, R.K. Hanson, G.W. Butler, and D.Q. King, "A Comparison of Arcjet Properties to Model Predictions," AIAA 93-0820, 31st Aerospace Sciences Meeting, Reno, Nevada, January 1993.
14. G.W. Sutton and A. Sherman, *Rngineering Magnetohydrodynamics*, McGraw-Hill, New York, 1965.
15. B.J. McBride and S. Gordon, "Fortran IV Program for Calculation of Thermodynamic Data," NASA TN D-4097, July 1965.
16. C.E. Moore, "Atomic Energy Levels," National Standards Reference data Systems, NSRDS-NBS 35, 1971.
17. J.G. Liebeskind, R.K. Hanson, and M.A. Cappelli, "LIF Measurements of Species Velocity in an Arcjet Plume," IEPC 93-131, 23rd International Electric Propulsion Conference, Seattle, WA, September 1993.
18. J.M. Yos, "Transport Properties of Nitrogen, Hydrogen, Oxygen, and Air to 30,000 K," AVCO Corporation technical Memorandum RAD-TM-63-7, Contract AF33(616)-7578, Task 73603, March 1963.
19. E. Meeks and M.A. Cappelli, "Two-temperature Fluid Model for High pressure Plasmas in Contact with Cooled Electrodes," J. Appl. Phys. **73**, 3172, 1963.
20. E. Meeks and M.A. Cappelli, "A Multi-fluid Model of Near-electrode Plasma Behaviour," AIAA 93-2103, 29th Joint propulsion Conference, Monterey, CA, June 1993.
21. Dr. Brian A. Cashiwa, Los Alamos National Laboratories, private communication.
22. W.H. Press, B.P. Flannery, S.A. Teukolsky, and W. T. Vettling, *Numerical Recipes in C*, Cambridge university Press, Cambridge, UK, 1988.
23. S.W. Jansen, The Aerospace Corporation, private communication.
24. D.H. Manzella, F.M. Curran, R.M. Myers, and D.M. Zube, "Preliminary plume Charateristics of an Arcjet Thruster," AIAA 90-2645, 21st International Electric propulsion Conference, Orlando FL, July 1990.
25. D.M. Zube, "Emission Spectroscopy Experiments in a Low Power Arcjet Nozzle," University of Stuttgart, Department of Aerospace Engineering, Engineering thesis, 1990.
26. P.V. Storm and M. .A. Cappelli, "Axial Emission Diagnostics of a Low Power Hydrogen Arcjet Thruster," IEPC-93-219, 23rd International Electric

propulsion conference, Seattle, WA, September 1993.

27. D.H. Manzella and M.A. Cappelli, "Vacuum Ultraviolet Absorption Measurements of Atomic hydrogen in a Hydrogen Arcjet thruster," AIAA 92-3564, 28th Joint Propulsion Conference, Nashville, TN, July 1992.

28. E. Hinnov and J.G. Hirschberg, "Electron-Ion Recombination in Dense Plasmas," Phys. Rev. **125**, 795, 1962.

29. F.M. Curran and D.H. Manzella, "The Effect of Electrode Configuration on Arcjet Performance," NASA Technical Memorandum 102346, July, 1989.

Reaction	A	B	E
$H+H+M \rightarrow H_2+M$	6.4×10^{17}	-1	0
$H^+ + e + M \rightarrow H + M$	5.26×10^{26}	-2.5	0
$H_2 + e \rightarrow H + H + e$	1.91×10^{11}	1	203,000
$H^+ + e + e \rightarrow H + e$	7.08×10^{39}	-4.5	0

Table 1. Chemical reaction mechanisms.

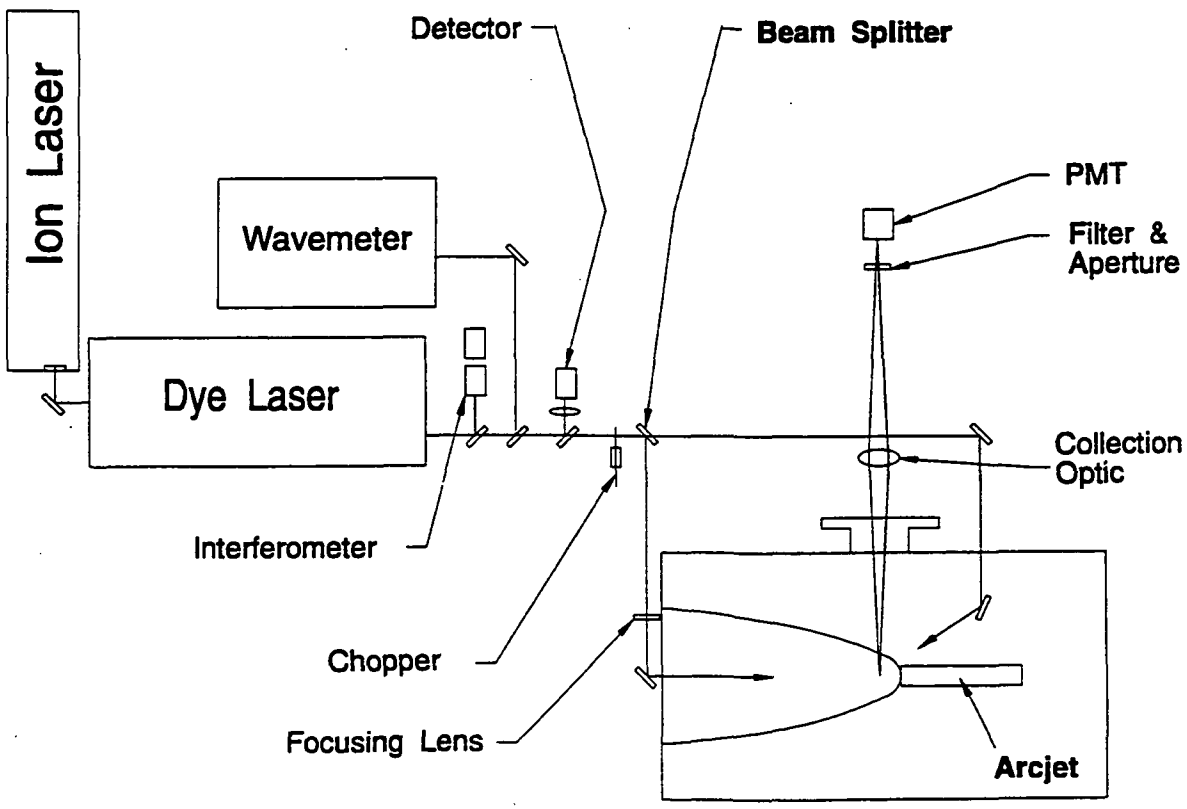

Figure 1. Schematic of experimental facility.

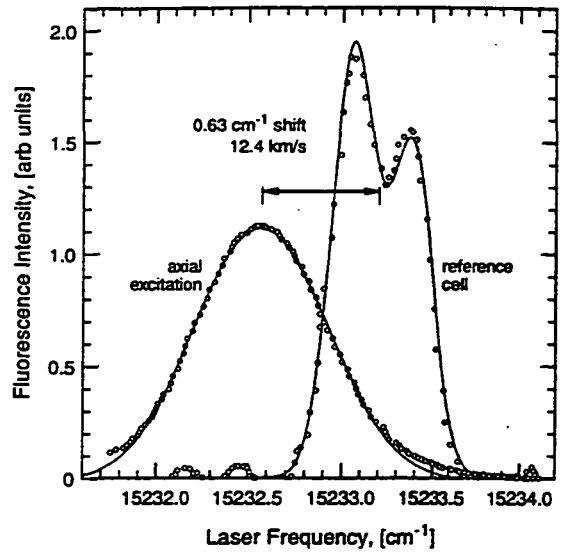

Figure 2. Typical fluorescence excitation scans taken with the laser focused along the centerline 0.4 mm from the exit plane. The more narrow profile with resolved features is taken from a 600 K low pressure stationary discharge cell.

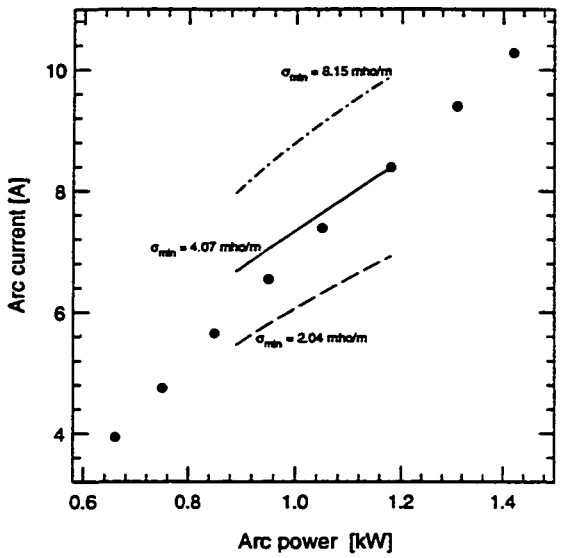

Figure 3. Comparison of experimental cuurent-power characteristics at a specific power of 90 MJ/kg to that predicted for three different values of the conductivity floor, σ_{min}.

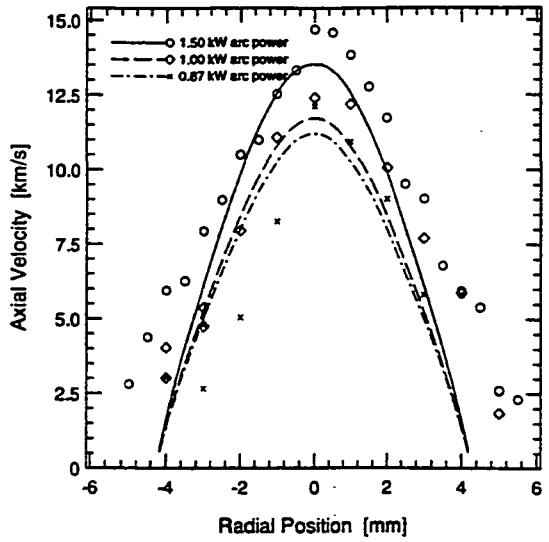

Figure 4. Comparison between measured (symbols) and predicted (lines) spatial variation in exit plane axial velocity. $\dot{m}$ = 13.7 mg/s.

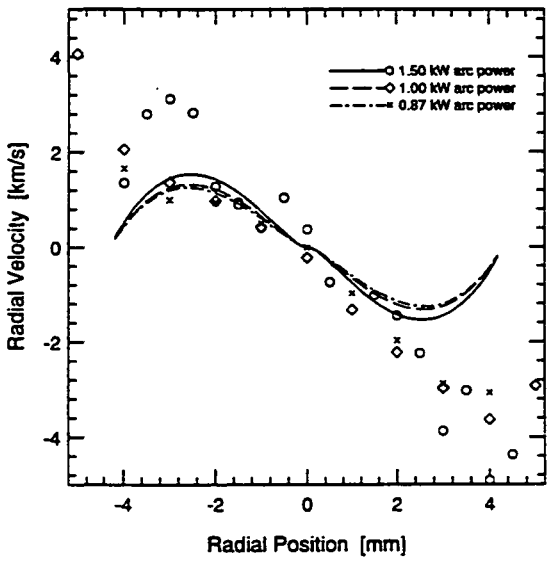

Figure 5. Comparison between measured (symbols) and predicted (lines) exit plane radial velocity component. $\dot{m}$ = 13.7 mg/s.

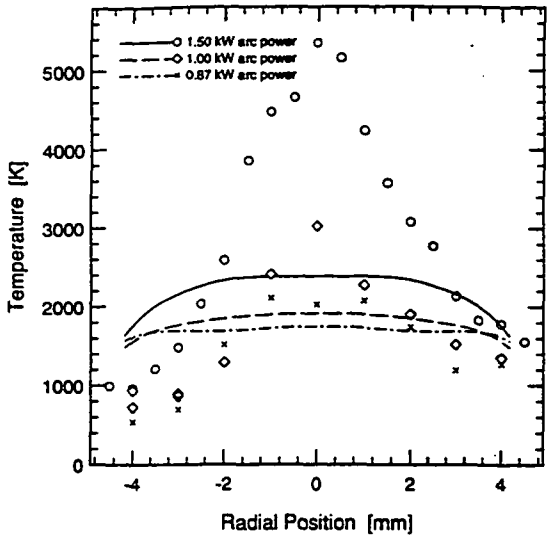

Figure 6. Comparison between measured (symbols) and predicted (lines) variation in the exit plane temperature. $\dot{m}$ = 13.7 mg/s.

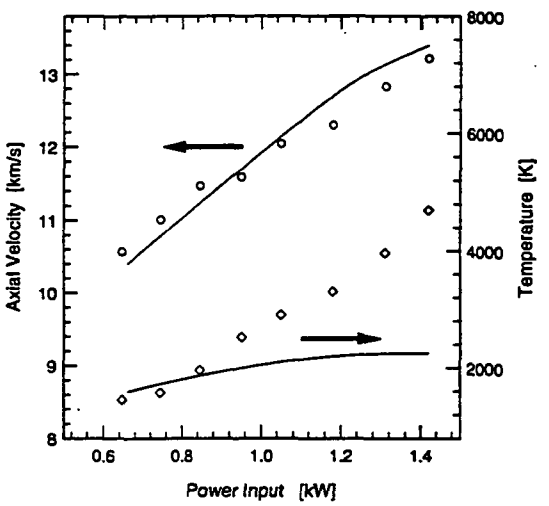

Figure 7. Computed (solid line) and measured (open symbols) variation in centerline axial velocity and temperature with power. $\dot{m}$ = 13.1 mg/s.

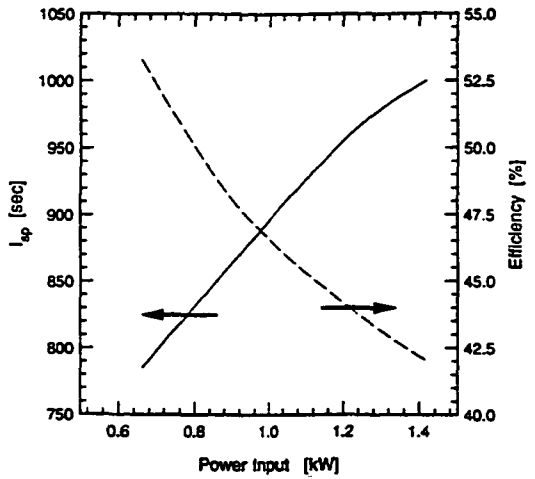

Figure 8. Computed variation in thrust efficiency and specific impulse with power. $\dot{m}$ = 13.1 mg/s.

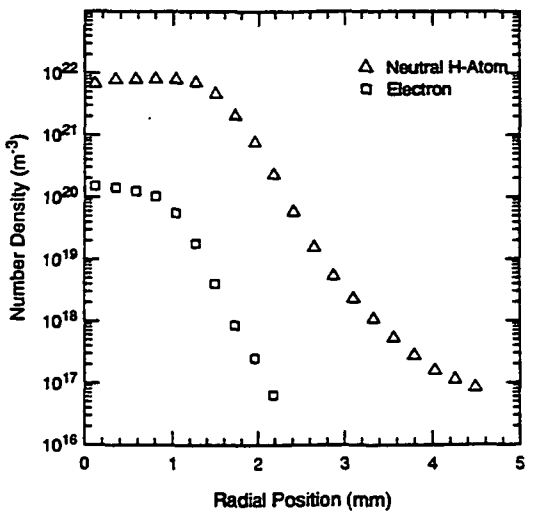

Figure 9. Computed radial variation in the exit plane electron and H-atom number densities. $\dot{m}$ = 13.1 mg/s, P/$\dot{m}$ = 113 MJ/Kg.

APPENDIX C

J. Fluid Mech. (1994), *vol.* 280, *pp.* 41–67

Numerical and experimental investigations of low-density supersonic jets of hydrogen

By I. D. BOYD[1], D. R. BEATTIE[2] AND M. A. CAPPELLI[2]
[1] Cornell University, Ithaca, NY 14853, USA
[2] Stanford University, Stanford, CA 94305, USA

(Received 12 November 1993 and in revised form 10 June 1994)

Low-density flow of molecular hydrogen from a small nozzle is studied using numerical and experimental techniques. The conditions in the nozzle indicate that non-equilibrium effects will significantly influence the flow. Therefore, the numerical analysis is undertaken using a Monte Carlo approach. The experimental studies employ spontaneous Raman scattering. Comparisons of the measured data and computed results are made for total number density, rotational temperature, and for the number density of the first rotational level. The numerical results are found to be quite sensitive to the rotational relaxation rate, and a strong degree of thermal non-equilibrium is observed at the exit plane of the nozzle. Comparisons between experiment and analysis permit estimation of the rotational relaxation rate for hydrogen. Investigations are also conducted for expansion of the supersonic jet into a finite back pressure. The interaction of the plume with the chamber background gas is found to form shock waves in both the simulations and experiments. This phenomenon is investigated further by increasing the background pressure. Direct comparison of the simulation results and experimental measurements is very favourable.

1. Introduction

Low-power hydrogen arcjet propulsion engines are under development for use on spacecraft for orbit transfer and station-keeping manoeuvres. Potentially, these engines offer significant improvements in specific impulse over current chemical rockets. However, the thrust efficiencies achieved to date with these rockets have only reached about 30%. Many of the factors that cause this relatively low efficiency are concerned with the fluid mechanics and chemical kinetics of hydrogen. The purpose of the present study is to examine some of these effects at a fundamental level. Detailed studies are performed for flow of hydrogen in a small nozzle. The geometric size and mass flow are representative of a spacecraft thruster. These aspects combine to give a low Reynolds number in the nozzle throat that yields flow in strong thermodynamic non-equilibrium. In this paper, both numerical and experimental studies are reported for an unheated hydrogen flow. These represent the first phase of a continuing effort to investigate arc-heated expanding hydrogen flows. The experimental investigation employs Raman scattering to obtain number density and rotational temperature.

Sophisticated experimental techniques are being applied to investigate flow properties in the nozzle and plume of various arcjet thrusters. In these investigations, the thruster plume expands into a vacuum tank. Of course, owing to the finite pumping speeds of ground-based experimental facilities, the back pressures obtained are orders of magnitude higher than orbital flight conditions. There is an interest in understanding

how measurements taken in such facilities may be affected by the interaction of the expanding thruster plume with this residual pressure in the test chamber. This study addresses the issue for the hydrogen thruster operated in the arcjet facility at Stanford University.

Unfortunately, it is quite difficult to estimate such effects. The plume expanding from a typical arcjet is complicated by viscous and chemical kinetic effects. The flow field is two-dimensional such that densities at the nozzle exit centreline may be an order of magnitude higher than those at the nozzle lip. In addition, the physical behaviour that occurs in the interaction region between the plume and the residual gas is not simple. Depending on flow conditions, shock waves may be formed, and the viscous and kinetic effects again become significant. Therefore, a detailed study of the interaction phenomenon has been undertaken. Experimental investigations again employ Raman scattering to measure number density along the axis of the plume. The measurements are carried through the interaction region where the thruster plume encounters the residual gas. In addition, Monte Carlo calculations of the same flow conditions are performed.

Details of the experimental and numerical methods are provided in the following sections. In the numerical study, particular attention is given to the modelling of rotational relaxation for H_2. A description of the nozzle and plume flows is given, and comparison of the numerical results and experimental data is discussed.

2. Experimental investigations

This section describes experiments performed using spontaneous Raman scattering to determine the rotational-level populations of H_2 for the flow in the expansion plume of a small rocket. The theory of this technique is described first. Discussions then follow on the experiments performed, and the methods employed for interpretation of the results.

2.1. *Theory*

Spontaneous Raman scattering is an inelastic, linear, two-photon scattering process. In this case, an incident photon scatters off an H_2 molecule causing a change in the molecular quantum state and a corresponding change in the energy of the scattered photon. The intensity of the signal is given by Valentini (1987):

$$N_{i,f} = N_L l n_0 \frac{n(v_i, J_i)}{n_0} \left(\frac{d\sigma}{d\Omega}\right)_{i,f} d\Omega, \tag{1}$$

where $N_{i,f}$ is the number of Raman photons collected for transition from initial state i to final state f; N_L is the number of incident laser photons; l is the sample length imaged; n_0 is the number density of scattering species; $n(v_i, J_i)/n_0$ is the population fraction in state i; v_i is the initial vibrational state; J_i is the initial rotational state; $(d\sigma/d\Omega)_{i,f}$ is the differential Raman cross-section for transition from state i to state f; and $d\Omega$ is the collection solid angle.

The number of scattered photons is linearly proportional to the number of incident photons and the density of the scattering species. Spontaneous Raman scattering has the advantage of allowing spatially resolved measurements of ground-state densities with an easily interpretable signal. The primary disadvantage is the small scattering cross-section (typically 10^{-33} m^2). Measurements here are based on the purely vibrational Raman transitions from $v = 0$ to $v = 1$ with $\Delta J = 0$ for $J = 0$, 1, 2 and 3 (i.e. the Q-branch). Table 1 shows a summary of initial and final states, wavelength,

v_i	v_f	J_i	J_f	λ (nm)	σ 10^{-33} m^2	n_i/n_0	Relative intensity
0	1	0	0	612.325	1.544	0.128	1.982
0	1	1	1	612.103	1.648	0.657	10.828
0	1	2	2	611.662	1.645	0.117	1.930
0	1	3	3	611.004	1.665	0.092	1.529

TABLE 1. Summary of Raman transitions

cross-section, Boltzmann fraction, and relative intensity for these transitions using a laser wavelength of 487.986 nm and a gas temperature of 300 K.

The density can be determined by using the absolute intensity from all transitions combined in conjunction with the signal from a reference cell. The sum of the intensity of each transition divided by its cross-section is proportional to the density and a constant determined by the optical system:

$$\sum_i \frac{N_{i,f}}{(\mathrm{d}\sigma/\mathrm{d}\Omega)_{i,f}} = \sum_i N_L l n_0 \frac{n(v_i, J_i)}{n_0} \mathrm{d}\Omega$$
$$= N_L l n_0 \mathrm{d}\Omega$$
$$= \alpha n_0. \tag{2}$$

A spectrum recorded from a known gas density can be used to determine α and hence the density from subsequent spectra.

The relative intensity of the various transitions can be used to determine a rotational temperature, assuming partial thermodynamic equilbrium exists among the rotational states. The intensity of each transition divided by its cross-section is proportional to the density and the population fraction of the initial state:

$$\frac{N_{i,f}}{(\mathrm{d}\sigma/\mathrm{d}\Omega)_{i,f}} = N_L l n_0 \frac{n(v_i, J_i)}{n_0} \mathrm{d}\Omega$$
$$= \alpha n_0 \frac{n(v_i, J_i)}{n_0}$$
$$= \alpha n_0 f(T, i). \tag{3}$$

When two or more transitions are observed, their intensities can be fitted to a function of temperature and density (using the predetermined optical system constant).

2.2. *Experiments*

The nozzle considered in the present study is based on a 1 kW class NASA hydrogen thruster. The converging–diverging nozzle geometry is shown in figure 1. Note the cathode that is present in the device. The nozzle has a 0.64 mm throat diameter with a 20° half-angle, and an exit-to-throat area ratio of 225:1. The conditions chosen for examination represent a cold-flow configuration in which the arc is not ignited. The specific flow conditions are a stagnation temperature of 295 K and a mass flow rate of 14.1 mg s^{-1}. These conditions correspond to a Reynolds number at the nozzle throat of about 2800. This value indicates that the flow is dominated by the effects of thermal relaxation, and by viscosity in the nozzle boundary layer. The thruster is operated in a vacuum chamber 1.09 m long and 0.56 m in diameter with optical access through 75 mm diameter ports. It is mounted on a two-axis translation stage (axial and radial).

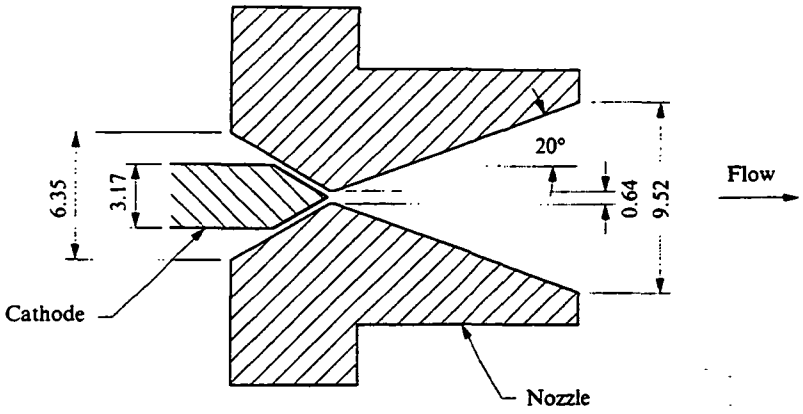

FIGURE 1. Nozzle geometric configuration (dimensions in mm).

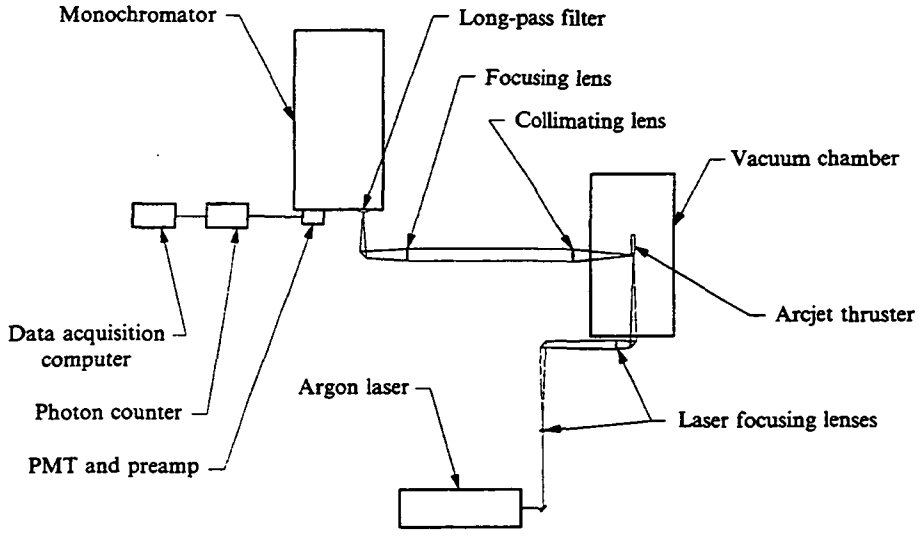

FIGURE 2. Experimental apparatus.

The tank is evacuated by two Roots blowers backed by mechanical roughing pumps with a total capacity of $1.2\ m^3\ s^{-1}$. This system is capable of maintaining a back pressure of 43 ± 2 Pa with a flow rate of $14.1 \pm 0.1\ mg\ s^{-1}$.

The Raman excitation source is an Ar^+ laser with 2.5 W in the 487.986 nm line used for this experiment. The laser beam is focused axially into the plume with a beam waist under 100 μm (see figure 2). Scattered light is collected and focused onto a monochromator entrance slit with an achromatic two-lens system. The collection optical axis is perpendicular to the laser polarization and the direction of laser propagation. The spatial resolution is 4 mm in the axial direction (determined by the slit height) and 0.1 mm in the radial direction (determined by the laser beam waist). The monochromator is a 1.0 m focal length f/8.7 single-pass Czerny–Turner design with a 1180 line mm^{-1} grating blazed at 500 nm. A long-pass filter is placed before the entrance slit to further reduce the intensity of collected laser light to negligible levels. The monochromator slits are typically 300 μm giving a spectral resolution of 0.2 nm.

Light is detected at the exit slits by a cooled low-noise photomultiplier tube (PMT) with dark noise of 0.4 counts s^{-1}. The PMT output is amplified and sent to a

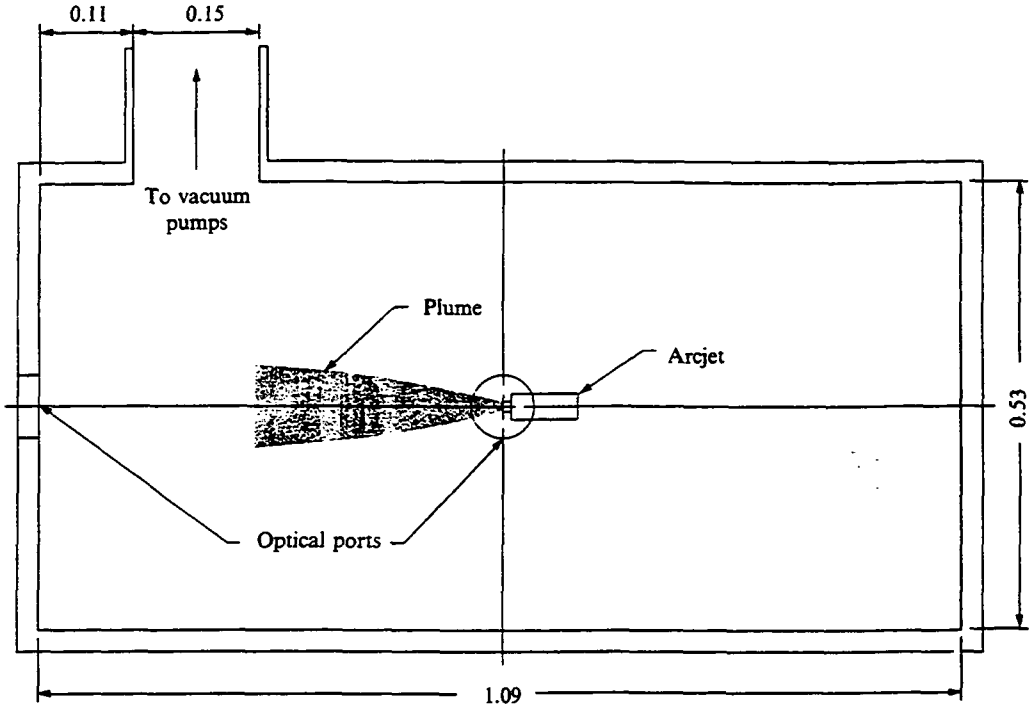

FIGURE 3. Schematic of arcjet in vacuum chamber (dimensions in m).

continuously gated photon counter. The monochromator is scanned over the spectral ration of interest and the photon counter output is recorded on a computer. The signal intensity is calibrated by filling the chamber with 10 kPa of H_2. A spectral scan is recorded with the operating conditions unchanged from those used for the data scans.

The overall experimental configuration is shown schematically in figure 3. Of particular interest is the position of the vacuum pumps with respect to the expanding flow. The location of the pumps will clearly give a non-symmetric background pressure field. It is presumed that such effects are small given the relatively large distance of separation between the pumps and the arcjet.

2.3. *Data analysis*

Spectral scans of the Raman Q-branch are recorded at various radial positions from the centreline to the nozzle edge. The collection segment starts at the nozzle exit plane and extends 4 mm downstream. Scans are also made on the centreline at various axial positions. The total number of scans taken is limited by the somewhat long scan duration of 40 minutes at 0.05 nm min^{-1}. In order to provide a more detailed view of the flow profile in the exit plane, data are also collected at a fixed spectral position while scanning the axial position.

The spectral data are analysed by fitting to theoretical spectra with the unknown quantities such as temperature and density as fitting parameters. The theoretical spectra are obtained by calculating the predicted position and intensity of the various Q-branch lines, then convoluting with the instrument response function. The line positions are taken from the experimental values of Veirs & Rosenblatt (1987) which are in excellent agreement with the quantum mechanical calculations of Wolniewicz (1983). The line intensities are proportional to the Boltzmann fraction in the initial

state and the transition Raman cross-section. The cross-sections are taken from the dynamic polarizability calculations of Ford & Brown (1973). Since these values are averaged over all solid angles for unpolarized light, it is assumed that any variations with solid angle or polarization are the same for all Q-branch transitions. Note that the Ford & Brown cross-sections are defined in terms of scattered energy rather than scattered photons, as defined in (1). The two definitions differ by a factor of λ_s/λ_0, where λ_s is the scattered wavelength and λ_0 is the incident wavelength.

As expected, the observed spectral features are principally instrument broadened. The Raman transitions are primarily Doppler broadened at the low pressures involved. According to Weber (1973), the Doppler width (FWHM) is

$$\Delta\nu_D = \frac{2}{c}\left(2\ln 2\frac{kT}{m}\right)^{1/2}\left[4(\nu_0^2+\nu_0\nu_R)\sin^2\frac{\theta}{2}+\nu_R^2\right]^{1/2}, \tag{4}$$

where T is the gas temperature = 300 K; m is the hydrogen molecule mass; ν_0 is the incident photon frequency; ν_R is the Raman frequency shift; and θ is the collection angle = 90°.

Using (4), a value of 3.57 GHz is obtained for $\Delta\nu_D$. This Doppler width of 4.5 pm and the laser linewidth of 5 pm are both small in comparison to the 0.2 nm monochromator resolution. Hence the monochromator slit function is used to represent the instrument function for fitting purposes. Since the monochromator slits are equal in width and the resolution is large compared to the diffraction limit (0.01 nm), a triangular function is utilized.

Two fits are performed. The first fit, NTE (Non-Thermodynamic Equilibrium), does not assume that the flow is in thermodynamic equilibrium. The rotational population fractions (and thereby relative intensity of the transitions) are freely varied to best fit the data. Additional fit parameters include a wavelength offset to account for monochromator error, an intensity offset to allow for PMT dark noise, and the width of the slit function.

The second fit (LTE) assumes that the flow is in local thermodynamic equilibrium (LTE) with a rotational temperature dictating the rotational population fractions. The two parameters in this fit are the temperature and number density. The wavelength offset, intensity offset and spectral resolution have the same values determined by the NTE fit. The rotational energy levels used to compute the Boltzmann fractions are calculated with a six-parameter fit from Jennings, Rahn & Owyoung (1985). This fit is in excellent agreement with the energy level calculations for $J = 0, 1, \ldots, 5$ of Wolniewicz (1983). The vibrational partition function is calculated assuming a harmonic oscillator using the energy difference from $\nu = 0$ to $\nu = 1$ also provided by Wolniewicz. The harmonic approximation introduces negligible error in absolute intensity since the population fraction in the ground state is close to unity at the low temperatures of this study.

At the low temperatures involved here, the symmetric/antisymmetric nuclear spin states of H_2 do not reach equilibrium. This equilibration process can be extremely slow in the absence of a catalyst (McQuarrie 1973). Owing to the coupling of nuclear and rotational spin states, this non-equilibrium results in the rotational populations deviating from a Boltzmann distribution. Since H nuclei have spin $\frac{1}{2}$ (i.e they are fermions), H_2 must have an antisymmetric total wave function:

$$\Psi_{total} = \Psi_{trans}\Psi_{rot}\Psi_{vib}\Psi_{elec}\Psi_{nuclear}. \tag{5}$$

The only components of the total wave function which can be antisymmetric are the nuclear and rotational wave functions (see table 2). Therefore, an H_2 molecule must

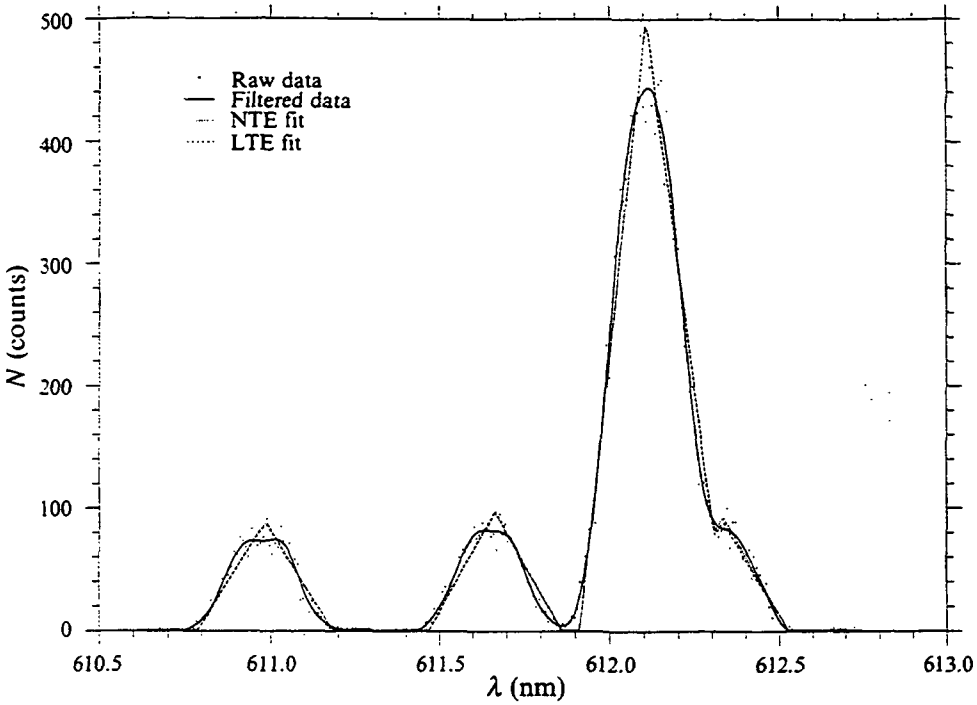

FIGURE 4. Scan of Raman intensity against wavelength taken under reference conditions.

Wave function	Symmetry	Degeneracy
Translational	Symmetric	1
Rotational		
J even	Symmetric	$2J+1$
J odd	Antisymmetric	$2J+1$
Vibrational	Symmetric	1
Electronic: $^1\Sigma_g^+$	Symmetric	1
Nuclear		
Ortho	Symmetric	3
Para	Antisymmetric	1

TABLE 2. H_2 wave function

be in a symmetric nuclear state and antisymmetric rotational state or vice versa. These two combinations are often referred to as ortho and para respectively. The nuclear degeneracy ratio of 3:1 (ortho–para) results in a 3:1 statistical weighting of odd–even J states. Above 300 K, the upper rotational states are sufficiently populated in a Boltzmann distribution that the ortho–para ratio is in fact 3:1. However, at lower temperatures where the population increasingly fills $J = 0$, the ortho–para ratio decreases. In the limit as T approaches 0, the equilibrium ortho–para ratio also approaches zero.

The implication of this phenomenon is that equilibrium dictates an ortho–para ratio below 3:1 at the temperatures in this flow. However, since the ortho–para ratio is frozen at the 3:1 high-temperature limit, the rotational population fractions will not be Boltzmann, even if the rotational states are in LTE. This effect is accounted for in the fitting process by upholding the 3:1 ortho–para ratio, while at the same time

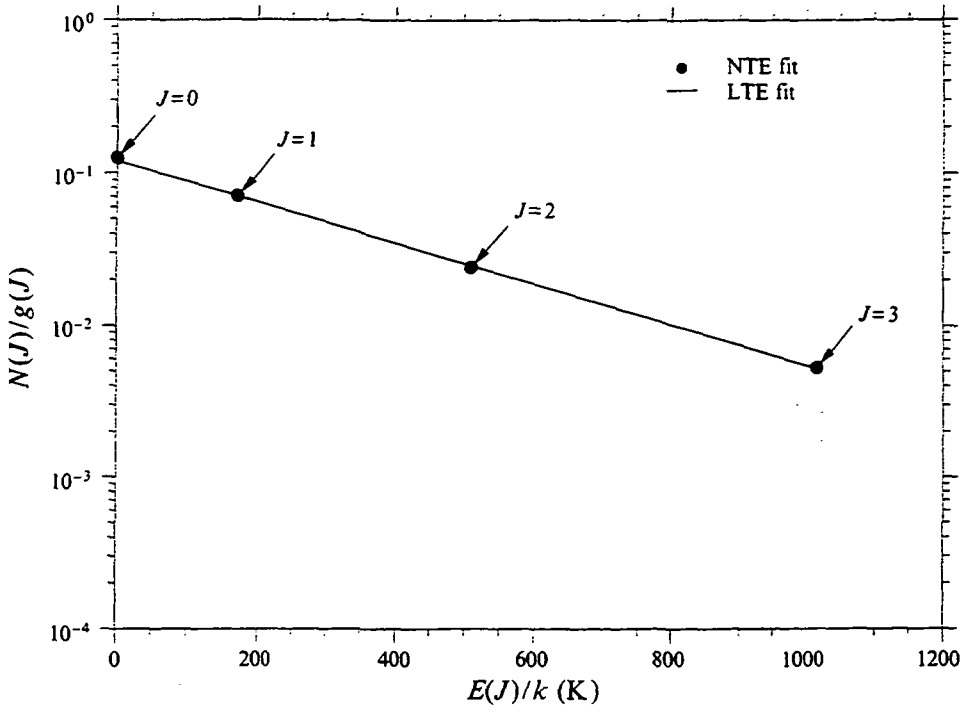

FIGURE 5. Boltzmann plot of rotational population under reference conditions. $T = 323 \pm 1$ K, $n = (2.27 \pm 0.02) \times 10^{24}$ m^{-3}.

requiring that the odd and even states independently satisfy a Boltzmann distribution with the same rotational temperature. On a Boltzmann plot, the odd and even states each fall on a line with the same slope (i.e. same temperature) but a different intercept. As the temperature is decreased the intercepts move further apart.

In order to measure absolute density, reference scans are taken with the tank containing 10 kPa of hydrogen. A sample reference scan showing the raw data, filtered data, NTE fit, and LTE fit is shown in figure 4. The raw data are low-pass filtered to allow the spectral features to be seen more clearly. Fitting to the raw data and filtered data is found to give identical results. The two fits agree quite well, as expected, since the gas should be in equilibrium. A Boltzmann plot of the results from the two fits shows that the data match the equilibrium fit to within experimental error (figure 5).

A scan taken in the exit plane of nozzle is shown in figure 6. The intensity is lower than the reference intensity and the shot noise is much more evident. It is also clear that the population has shifted almost entirely into the $J = 0$ and $J = 1$ states, indicating a lower temperature. The LTE fit temperature was 113 ± 5 K. From the Boltzmann plot shown in figure 7, one can see the equilibrium fit lines match the $J = 0$, 1, and 2 intensities quite well. The discrepancy between the equilibrium and non-equilibrium fits at $= 3$ is not surprising since the signal-to-noise ratio of that data point is very poor (< 1).

The calculation of number density is slightly more accurate than temperature, especially at the lower signal levels. The cross-sections of interest are almost equal, so it is not critical that the fitting process determine exactly what portion of the overlapping peaks corresponds to $J = 0$ and $J = 1$. However, the error in density of the data scan is the sum of the density parameter fitting error and the reference density error.

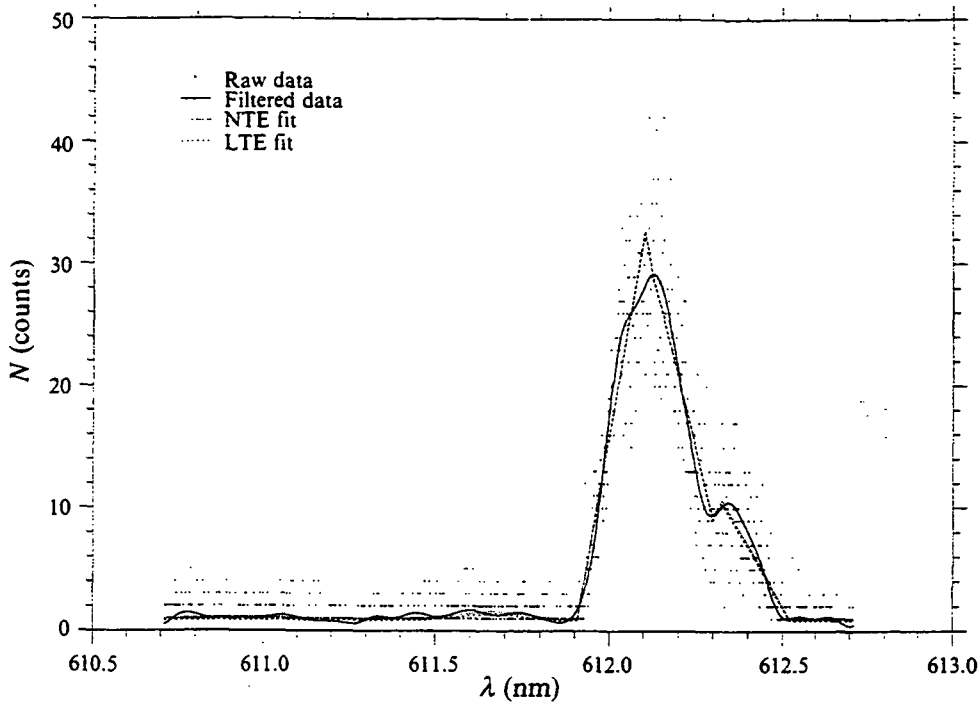

FIGURE 6. Scan of Raman intensity against wavelength taken in the nozzle exit plane.

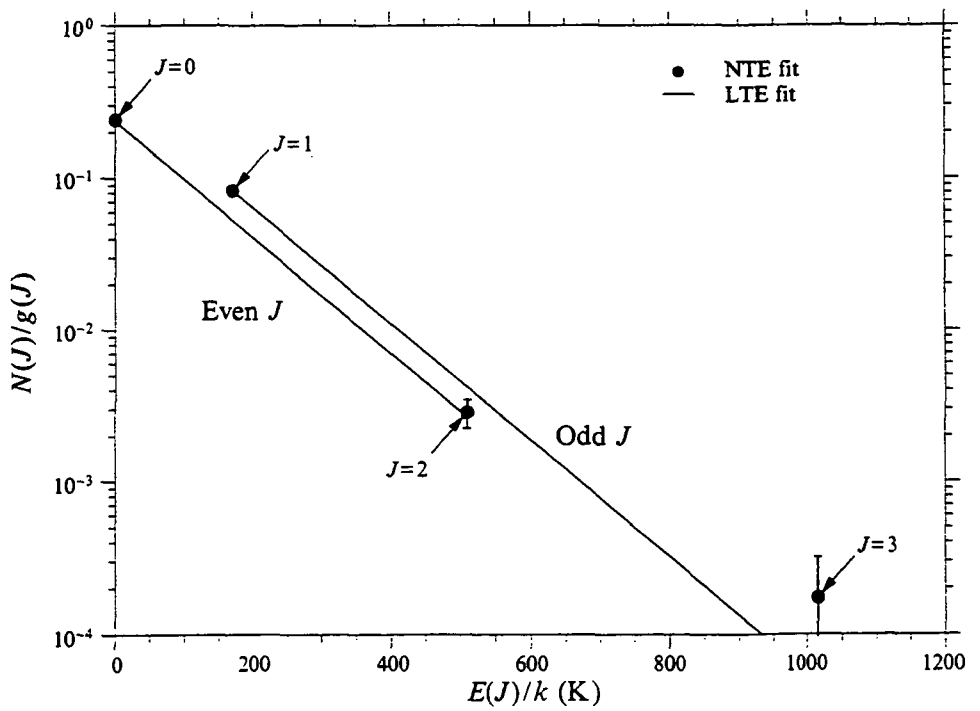

FIGURE 7. Boltzmann plot of rotational population taken in the nozzle exit plane, $T = 113 \pm 5$ K, $n = (6.15 \pm 0.15) \times 10^{22}$ m^{-3}.

A more detailed view of the exit-plane flow profile is obtained by setting the monochromator at the $J = 1$ peak and scanning the flow position radially. For this step, spectral resolution is less important, so the slits are opened to 400 μm to maximize the signal. This signal is proportional to the population in the $J = 1$ state, so it is normalized by the $J = 1$ signal from the spectral scans to give the density of state $J = 1$.

For the experimental data taken along the plume centreline, again the signal from the $J = 1$ state is measured. In this study, data are taken along the arcjet axis from the exit plane to 60 mm downstream. The back pressure in the vacuum tank is varied from 43 to 67 Pa by varying the number of pumps used. Data are also taken with the chamber evacuated below 1 Pa to give a background signal, and filled with 10 kPa hydrogen for a reference signal. The plume density is found by subtracting the background signal from the measured signal, then scaling by the known density of the reference scan. The error in density is estimated as one standard deviation, assuming that the counts follow a Poisson distribution. The errors range from 6% at the highest densities to 36% at the lowest.

3. Numerical investigations

This section discusses the numerical and physical aspects of simulating the flows of hydrogen using a Monte Carlo method. The general methodology for simulating the nozzle flow is described, details of the kinetics models employed are provided, and the rocket plume simulations are described.

3.1. *Nozzle flow simulation*

The low Reynolds number at the nozzle throat indicates that thermal non-equilibrium effects may be significant in the nozzle flow. The local value of the Reynolds number at the nozzle exit will be reduced by a factor close to the ratio of the exit and throat areas. Under such conditions, it is well established that the Navier–Stokes equations are invalid, owing to the failure of the linear forms for viscosity and thermal conductivity. A previous investigation of a small nitrogen thruster with a throat Reynolds number of 850 was reported by Boyd *et al.* (1992). In that investigation, experimental measurements of Pitot pressure were compared to continuum calculations at the nozzle exit. It was found that the continuum method overpredicted the pressure by 25%. An alternative numerical methodology for low-Reynolds-number flows is the direct simulation Monte Carlo method (DSMC) developed by Bird (1976). Instead of solving an equation set, this method attempts to provide a direct simulation of the flow by employing a large number of model particles. Boyd *et al.* (1992) employed this method and found it to give excellent agreement with the experimental data. Further studies by Penko *et al.* (1993) and Boyd, Jafry & Vanden Benkel (1994) have shown that the DSMC technique gives good agreement with experimental data taken in low-Reynolds-number plumes.

In a similar way to the previous study on N_2, the DSMC computation begins at the nozzle throat and extends out to the near field of the plume. Initially, throat profiles obtained from a Navier–Stokes solution of the flow were employed to begin the DSMC simulation. However, it was subsequently found that simple isentropic theory could be used without affecting the final DSMC solution far downstream of the throat. The interaction of the gas with the nozzle wall is assumed to be diffuse with full accommodation to a temperature of 300 K. In the study by Boyd *et al.* (1992) it was found that a temperature gradient existed along the nozzle wall. Such data were not

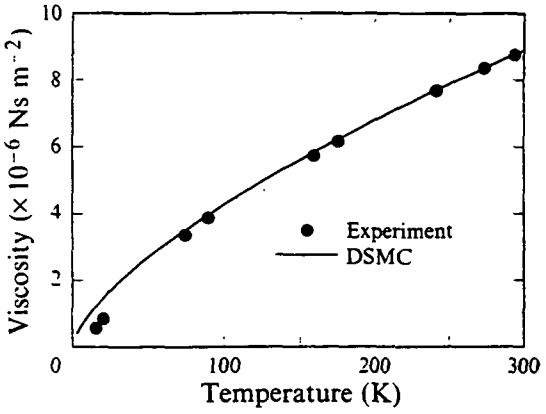

FIGURE 8. Temperature dependence of the viscosity coefficient for molecular hydrogen.

available for the present study and the assumption of a constant wall temperature may introduce a small error in the numerical results. For the nozzle simulation, the expansion of the plume is assumed to occur in a perfect vacuum. The computational grid employed in the present studies consists of 781 cells in the axial direction and 60 cells in the radial direction. The cell dimensions are varied with local flow conditions to maintain a maximum dimension of one local mean free path everywhere in the domain. In the important regions next to the nozzle wall and at the nozzle lip the cell sizes employed are much smaller than the local mean free path to obtain better resolution. An example of the type of grid employed in the present study is shown in Boyd *et al.* (1994). At the steady stage of the calculation there are about 700000 particles in a typical simulation. For this configuration, a typical run time is about 1.5 CPU hours on a Cray C-90.

3.2. *Hydrogen kinetics models*

Model parameters for translational and rotational relaxation must be chosen to apply the DSMC technique to low-temperature flows of molecular hydrogen. The stagnation conditions investigated indicate that it is only necessary to consider temperatures close to 300 K. Relaxation of the translational mode occurs in the simulation through collisions between particles. These collisions are computed by applying collision probabilities to pairs of particles in each cell in the computational domain. In the current study, the form of the collision probability is determined by the Variable Hard Sphere (VHS) model of Bird (1981). In this model, the important parameters are a reference collision diameter d_{ref} and a viscosity temperature coefficient ω. These parameters are obtained simultaneously by considering the temperature dependence of the coefficient of viscosity for hydrogen. In figure 8 experimental data for viscosity are compared to the VHS model using parameters $d_{ref} = 2.88 \times 10^{-10}$ m and $\omega = 0.67$. These are the values given by Bird (1981) for hydrogen and clearly give an excellent fit to the measured data.

In the DSMC method, relaxation of the rotational mode occurs by applying a probability of exchanging energy between the translational and rotational modes of particles that collide. For many diatomic species, a suitable energy-dependent form for this probability has been developed by Boyd (1990). The form of this probability reflects the observations made experimentally that the probability of rotational equilibration increases as temperature decreases. However, this trend appears to be reversed for diatomic hydrogen. In fact, the number of collisions required to equilibrate

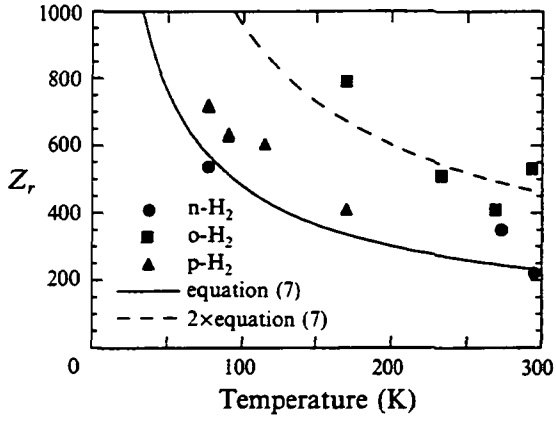

FIGURE 9. Temperature dependence of the rotational collision number for various forms of molecular hydrogen.

the rotational mode of this species increases as the temperature is decreased. This point is illustrated in figure 9 where the rotational collision number for three different forms of hydrogen are shown as a function of temperature. The experimental data are taken from literature cited by Lambert (1977). As discussed previously, the rotational state of hydrogen occurs in two different forms: para (p-H_2) and ortho (O-H_2). Under normal conditions (n-H_2), ortho-H_2 is present as 0.75 and para-H_2 is 0.25 by mole fraction.

Because the behaviour of H_2 differs from other diatomics, it is necessary to develop a new rotational energy exchange probability for the DSMC technique. In addition to the experimental data shown in figure 9, the available literature (Boitnott & Warder 1971; Lensch & Gronig 1977; Gallagher & Fenn 1974) indicates that the rotational relaxation time of hydrogen at temperatures below 300 K is within a factor of 2 of $\tau_r = 10^{-8}$ s at a pressure of 1 atmosphere. The definition for the rotational collision number is

$$Z_r = \tau_r/\tau_c, \tag{6}$$

where τ_c is the inverse of the molecular collision rate. Evaluating τ_c using the VHS model, and using a slightly higher value for the rotational relaxation time of $\tau_r = 1.4 \times 10^{-8}$ s, it may be shown that the rotational collision number for hydrogen is

$$Z_r = 10480/T^{\omega}. \tag{7}$$

This analytical form is compared to the available experimental data in figure 9. The simple model gives good agreement with the experimental data for normal hydrogen. By multiplying (7) by a factor of 2, good agreement is obtained for the experimental data for o-H_2. These comparisons give an idea of the spread in the available experimental data. Of course, this rather simple approach only gives an estimate of the rotational relaxation rate. Future studies may attempt to include more detailed analysis.

By following a similar analysis to that presented in Boyd (1990) for other diatomic species, it may be shown that the appropriate energy-dependent form of the probability of rotational energy exchange to be used in the DSMC technique based on (7) is

$$\phi_r = \frac{1}{Z_r} = \frac{1}{10480} \frac{\Gamma(\zeta + \frac{5}{2} - \omega)}{\Gamma(\zeta + \frac{5}{2})} \left(\frac{E_c}{k}\right)^{\omega}. \tag{8}$$

In (8), E_c is the total collision energy, k is the Boltzmann constant, and ζ is the average number of degrees of freedom participating in the energy exchange process ($\zeta = 2$ for a collision between two diatomic molecules that both exchange rotational energy in the collision). Because of its approximate nature, the leading constant in (8) is considered a parameter to be identified by comparison with the experimental data generated in this investigation.

Two separate adjustments must be made to (8) before it can be applied in the DSMC technique. The first is due to the implementation of collision mechanics. It has been shown by Lumpkin, Haas & Boyd (1991) that if the rotational energies of two particles are changed simultaneously in one collision then the probability must be multiplied by a factor

$$F_1 = \frac{5-2\omega+2\zeta}{5-2\omega}. \tag{9}$$

The second adjustment is due to the fact that the collision time given by the VHS collision model is not generally the same as that employed in converting experimentally measured rotational relaxation times to rotational collision numbers. In this conversion process, it is common (Parker 1964) to employ a collision time of the form

$$\tau_c = \pi\mu/(4p), \tag{10}$$

where μ is the coefficient of viscosity, and p is the pressure. Accounting for the viscosity and collision time produced by the VHS model (Bird 1981) the following correction must be applied to (8):

$$F_2 = \frac{8\Gamma(\frac{9}{2}-\omega)}{15\pi\Gamma(\frac{5}{2}-\omega)}\frac{208-12\omega}{211-12\omega(\frac{5}{2}-\omega)}. \tag{11}$$

In the current application, with $\omega = 0.67$, and $\zeta = 2$, (9) and (11) are evaluated as $F_1 = 2.093$ and $F_2 = 0.870$ respectively. The probability of exchanging translational and rotational energy for each collision is then given by

$$\phi_r = F_1 \times F_2 \times \text{equation (8)}. \tag{12}$$

3.3. *Plume flow simulation*

The code employed in the nozzle study is based on a numerically efficient program designed to be executed on Cray supercomputers (Boyd 1991). With minor modifications, the same code is used in the plume study on a computer work-station. The rate of execution of the code on the work-station is ten times slower than on a Cray YMP.

Application of the DSMC technique to model the nozzle and near-field plume expansion of this unignited hydrogen arcjet is discussed above. The hydrogen kinetics model described above is again employed in the plume study. The flow field considered begins at the exit plane of the nozzle and extends to distances of 10 cm axially and 6 cm radially. The results computed for the nozzle flow are employed as an input condition at the nozzle exit plane for the present study. Decoupling the nozzle and plume calculations saves a great deal of computational expense. The densities in the nozzle flow are orders of magnitude higher than those occurring in the plume. The computational expense of the DSMC method is approximately proportional to the density of the flow. Therefore, it takes much less computer resources to perform a plume calculation. The smaller size of the plume problem allows the simulation to be performed in reasonable times on the work-station. The decoupled approach for

simulating nozzle and plume flows using the DSMC technique has been successfully applied in previous investigations (Boyd *et al.* 1992; Penko *et al.* 1993). It is observed that only at the highest chamber pressure considered below is there a very small upstream influence. The decoupled approach appears to be valid at least for the conditions considered in this study.

Boundary conditions are applied along the radial line directly above the nozzle lip, and along the maximum axial and radial coordinates of the computational domain (at $Z = 10$ cm and $R = 6$ cm respectively). In each case, these are specified in terms of pressure and temperature. It is very difficult to perform an exact simulation of the chamber residual pressure. As illustrated in figure 3, the pressure is not distributed homogeneously throughout the chamber. Also, it is not clear what the temperature of the residual gas will be. For the purposes of the present investigation, a constant pressure (p_b) for the background gas is assumed at each of the boundaries. In addition, the residual gas is assumed to be at room temperature (300 K). Particles are introduced into the simulation across each boundary with properties corresponding to a gas at rest at the conditions of the residual gas defined in this manner. This technique was applied in a previous investigation of helium micro-thrusters (Boyd *et al.* 1994), and diffuse shock-like structures were observed in the solutions. However, no experimental data were available to assess the validity of those calculated results.

4. Results

In this section, direct comparison is provided of the experimental data and numerical results obtained in this study. The comparisons are divided into those for nozzle and those for plume flow.

4.1. *Nozzle flow*

Flow-field properties predicted by the DSMC method are first considered before comparison with the experimental data is made. Contours of Mach number for the nozzle flow are shown in figure 10. It is noted that a very large viscous boundary layer develops in the nozzle flow such that only about 30% of the nozzle exit plane is isentropic. The DSMC method is found to successfully predict the important phenomenon at the nozzle lip which is intersected by the sonic line. This behaviour is not generally predicted by continuum methods and is due in part to the need to include slip effects along the nozzle wall. An idea of the degree of thermal non-equilibrium in the flow field is obtained from figures 11(*a*) and 11(*b*) where contours of temperatures obtained for the translational and rotational modes are shown. It is clear that the rotational mode relaxes at a significantly slower rate than the translational mode. These results are obtained using (12). It is concluded that rotational non-equilibrium plays an important role in the expansion of molecular hydrogen under conditions of low Reynolds number.

Comparison of numerical results and experimental data for total number density in the nozzle exit plane is made in figure 12(*a*). Three different DSMC solutions are shown corresponding to Case 1 using (12), Case 2 using half of (12), and Case 3 using twice (12) for the rotational relaxation rate of H_2. Note that Case 1 corresponds to the solid line given in figure 9 and Case 2 corresponds to the dashed line. Generally, the computational results for density are relatively insensitive to the exact form of the rotational relaxation rate. and quite good agreement with experiment is obtained. In both experiment and simulation a small drop in density close to the nozzle axis is observed. This is believed to be due to the influence of the thick viscous boundary layer that causes the gas on the centreline to expand more rapidly.

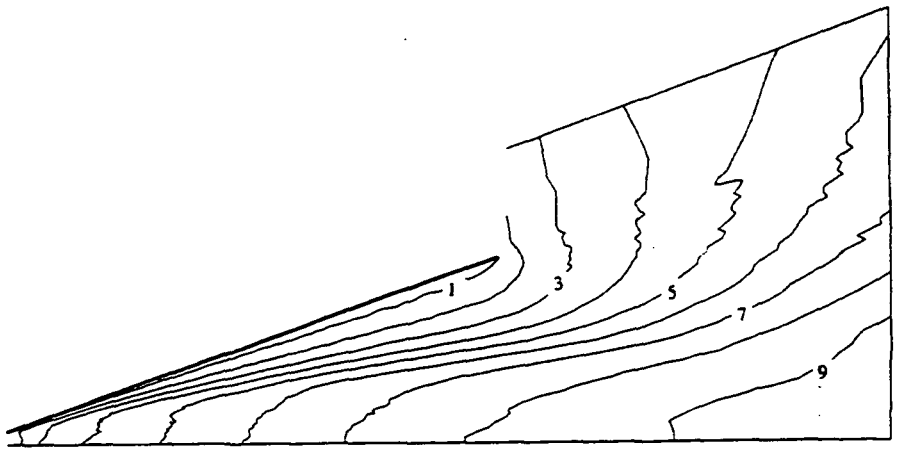

FIGURE 10. Contours of Mach number computed using the DSMC technique.

(*a*)

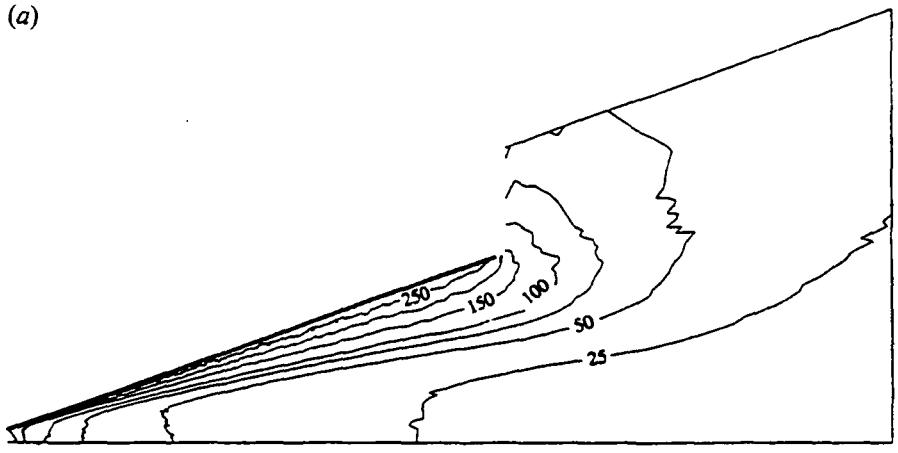

(*b*)

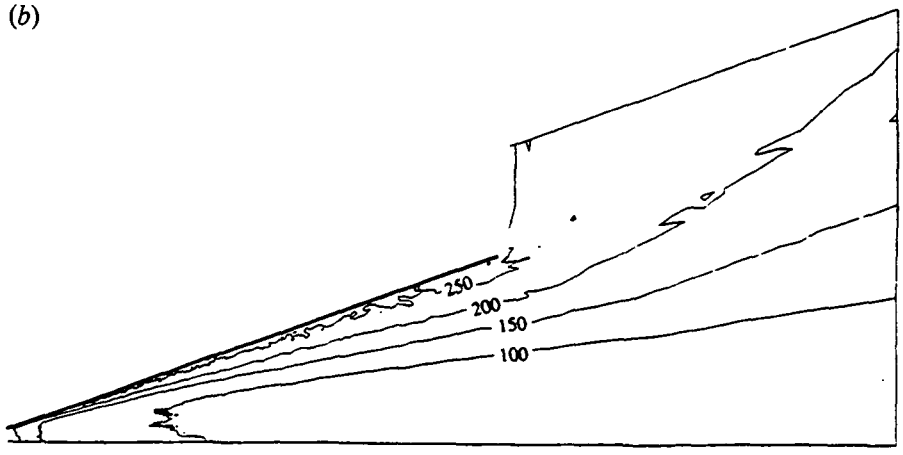

FIGURE 11. Contours of (*a*) translational and (*b*) rotational temperature. computed using the DSMC technique.

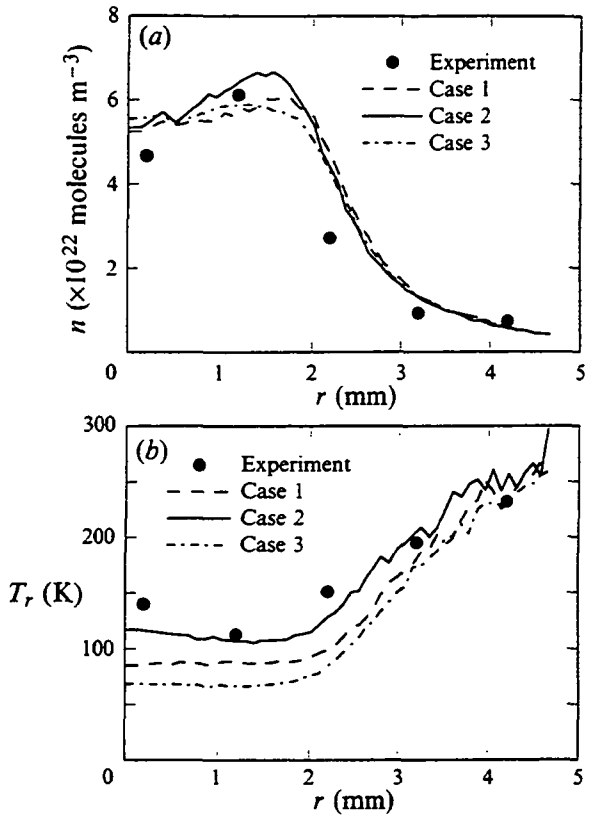

FIGURE 12. Comparison of experimental data and DSMC results for (*a*) number density and (*b*) rotational temperature in the nozzle exit plane.

Rotational temperature profiles in the nozzle exit plane are compared in figure 12(*b*). As might be expected, this quantity is much more sensitive to the probability employed for rotational equilibration. At the axis, there is a difference in rotational temperature of a factor of about 2 between Cases 2 and 3, corresponding to a difference in relaxation rate of a factor of 4. The best agreement with experiment is obtained for Case 2, the slowest rate considered. In agreement with the experimental data there is a small rise in rotational temperature at the nozzle axis. This makes physical sense considering the small decrease in density described previously. To display the significant degree of thermal non-equilibrium predicted by the DSMC method in the flow, the translational and rotational temperatures obtained in Case 2 are compared with the experimental data in figure 13. At conditions of thermal equilibrium, the rotational temperature could be combined with the number-density measurements to estimate the pressure in the nozzle exit plane using the equation of state. The DSMC analysis reveals that this procedure leads to errors in pressure on the axis of a factor of about 5. This observation provides a strong argument in favour of the need to perform detailed numerical simulations and to directly measure the gas kinetic temperature for these non-equilibrium flows.

The final comparison of results and data is for the number density of the first rotational level in the nozzle exit plane. These measurements are made at a finer spatial resolution than the total number density and rotational temperature measurements considered previously. The comparison is shown in figure 14. The DSMC results are

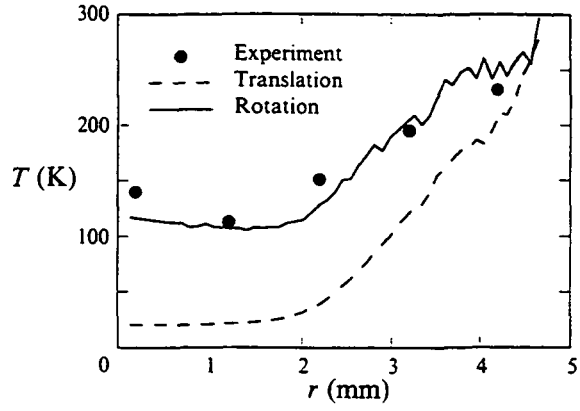

FIGURE 13. Degree of thermal non-equilibrium computed for Case 2 in the nozzle exit plane.

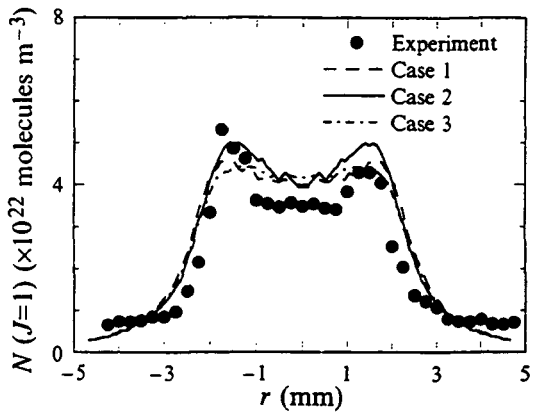

FIGURE 14. Comparison of experimental data and DSMC results for density of the $J = 1$ state in the nozzle exit plane.

computed from the values for total number density and rotational temperature in the exit plane. Note the small degree of asymmetry in the experimental data. The data on the left wing are in better agreement with those shown in figure 12. For this reason, it is concluded that the best comparison of theory and measurement occurs for Case 2. The good agreement obtained using this probability function for the three different data sets allows a value to be estimated for the rotational relaxation rate of hydrogen at temperatures below 300 K. When the probability used in Case 2 is converted into a relaxation time the value is $\tau_r p = 2.8 \times 10^{-8}$ s atm. This value is higher than those generally quoted for the relaxation of normal hydrogen. Recalling that a constant rotational relaxation time was employed in the analysis for temperatures below 300 K, this higher value may indicate that there is an increase in τ_r at low temperatures. On the other hand, this value is consistent with the experimental measurements for ortho-hydrogen. It is concluded that the relaxation time obtained in the present study is at least within the range of experimental data reported previously in the literature. The value obtained in the present study is a more complete test of the relaxation model due to the two-dimensional, viscous, and rapid-expansion processes experienced in the flow.

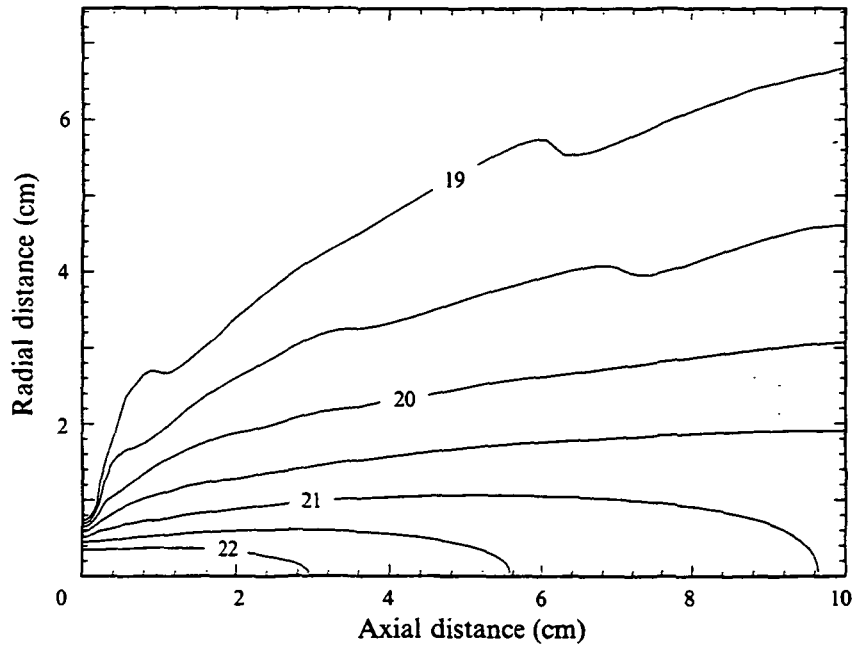

FIGURE 15. Contours of $\log_{10}$ number density in molecules m^{-3} at a background pressure of 0 Pa.

4.2. *Plume flow*

First, the DSMC method is applied to model the hydrogen-plume expansion process into a perfect vacuum. This is similar to the in-flight operational mode of the device (although here the arc is unignited). The boundary conditions are therefore specified as $p_b = 0$ Pa. Contours of number density are shown in figure 15. Note that the nozzle exit is about 4.75 mm long, and the origin is at the nozzle exit. It is clear that the flow is highly directed. The variation of density along the plume centreline is shown in figure 16(*a*). The density decreases rapidly by a factor of about 50 at a distance of 10 cm from the nozzle exit. A significant decrease in the translational temperature is shown in figure 16(*b*). The translational temperature shown in figure 16(*b*) is a weighted average of the single mode parallel to, and the two modes perpendicular to, the flow direction. While the former mode is frozen due to lack of collisions, the latter modes continue to decrease due to geometric effects. Specifically, as the distance away from the source of a highly expanded, low-density jet increases, the molecules located on the centreline tend to have smaller and smaller velocity components perpendicular to the flow direction. This is because only those molecules with such velocity components have not moved far away from the centreline during the expansion process. Thus, when the frozen parallel velocity component is combined with the slowly decreasing perpendicular components, the overall translational temperature continues to decrease as shown in the computations. Also included in figure 16(*b*) is the rotational temperature which is frozen. Note the degree of thermal non-equilibrium that exists at the nozzle exit plane which occurred during the nozzle expansion process.

The lowest value of the residual chamber pressure that can be achieved in the experimental facility is $p_b = 43$ Pa. Contours of number density in particles m^{-3} obtained using the DSMC technique for this condition are shown in figure 17. The finite chamber pressure creates a very thin jet with a diameter of about 1 mm. The diagram illustrates the important features that are typical of those observed in all

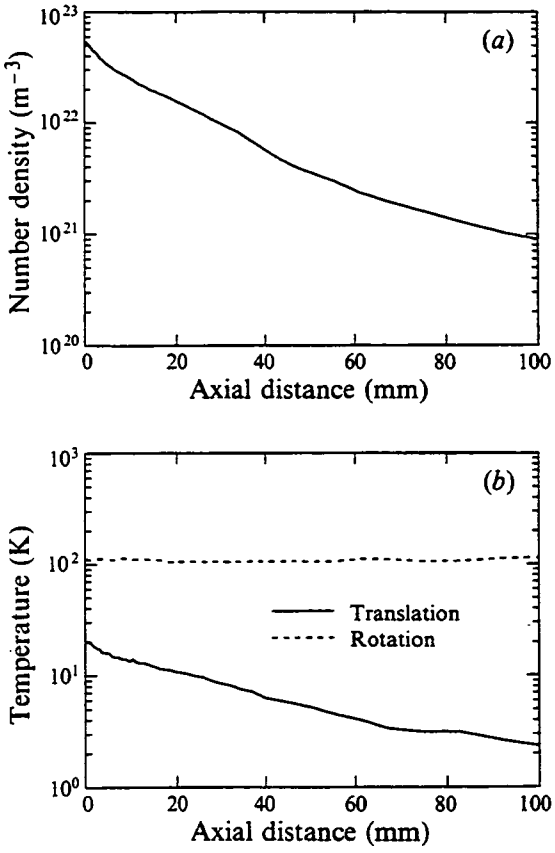

FIGURE 16. (*a*) Number density and (*b*) translational and rotational temperature, along the plume centreline computed with the DSMC method at a background pressure of 0 Pa.

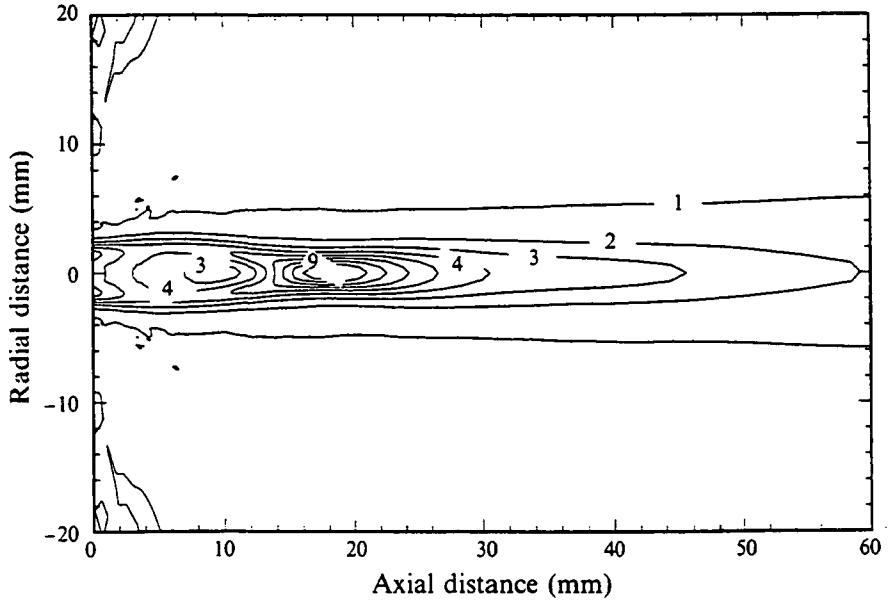

FIGURE 17. Contours of number density in molecules m^{-3} at a background pressure of 43 Pa. (Contour levels multiplied by 10^{-22}.)

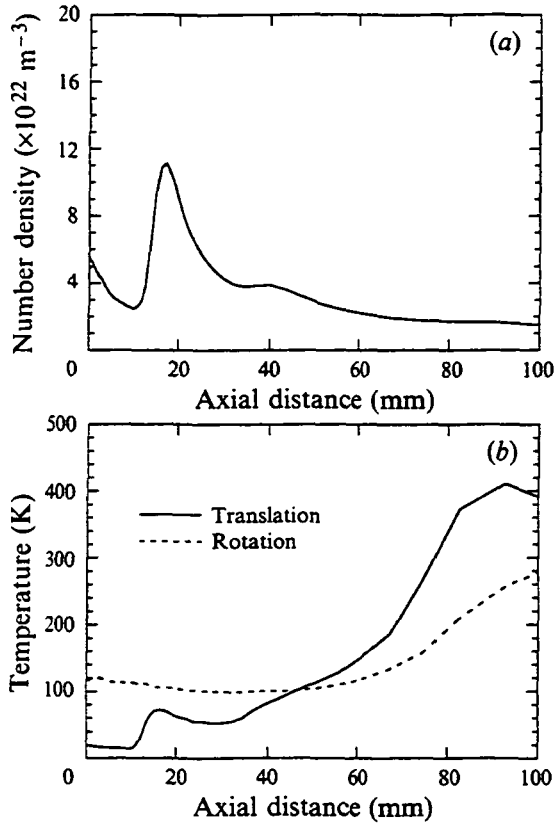

FIGURE 18. (*a*) Number density and (*b*) translational and rotational temperature, along the plume centreline computed with the DSMC method at a background pressure of 43 Pa.

calculations which include the chamber pressure. Careful examination of figure 17 reveals that the density along the jet centreline falls then rises sharply before falling again. This behaviour is considered in greater detail in figures 18(*a*) and 18(*b*) which show the density and temperatures obtained along the centreline. The profiles indicate that complex fluid dynamics processes are at work. A very strong shock wave is formed at a distance of about 10 mm from the nozzle exit plane. Behind this shock, the gas expands rapidly again before a second compression is reached. This secondary shock-like structure is much weaker, and the gas eventually starts to expand again further downstream. Although not clear in figure 18(*a*), a further weaker compression occurs at about 70 mm from the nozzle exit plane. These results are consistent with the diamond shock patterns observed in larger supersonic nozzles. The pressures in the nozzle exit plane are less than the residual pressure of 43 Pa, thus the nozzle is overexpanded. Actual diamond structure is not observed in the calculations. This is presumably due to viscous dissipation at the low densities encountered. The compression and expansion wave behaviour is also found in the translational temperature profile shown in figure 18(*b*). The translational mode reaches a local maximum after the shock formation at 10 mm from the nozzle exit plane. The subsequent expansion is followed by further compression of the temperature up to and beyond the temperature of the background gas. Extension of the flow field beyond 10 cm axially would presumably allow the translational mode to equilibrate with the residual gas. By comparison, the rotational mode undergoes a much slower rate of

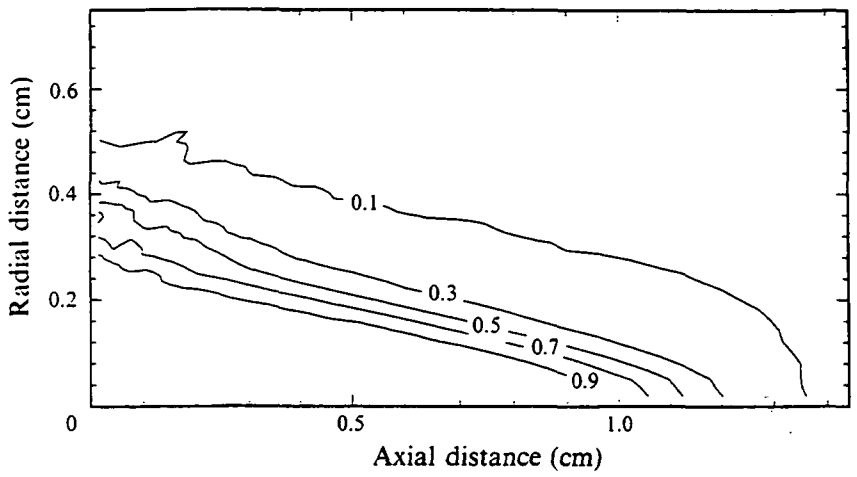

FIGURE 19. Contours of the ratio of pressure obtained at $p_b = 0$ Pa to that obtained at $p_b = 43$ Pa.

relaxation. The rotational temperatures slowly rise towards the equilibrium value. This illustrates the degree of thermal non-equilibrium that accompanies the complex flow-field structure of these interaction regions.

The results shown in figures 18(*a*) and 18(*b*) indicate that the effective test section of flow undisturbed by the residual gas only extends along the axis to a distance of about 10 mm along the plume centreline. Radially, the influence of the chamber pressure is much stronger owing to the reduction in nozzle exit pressure in the radial direction. In figure 19 contours are shown of the ratio of pressures computed with $p_b \approx 0$ to those obtained at $p_b = 43$ Pa. The contour value just less than unity indicates where the residual gas first affects the plume expansion process. While the flow along the axis is unaffected to a distance of about 10 mm from the nozzle, it is clear that in the radial direction interference effects are felt much sooner. Indeed, it appears that there is some interference close to the nozzle lip in the nozzle exit plane. This is confirmed in figures 20(*a*) and 20(*b*) which compare the number-density and translational-temperature profiles computed just downstream of the nozzle exit plane for the vacuum and $p_b = 43$ Pa cases. Figure 20(*a*) indicates that the number density at the nozzle exit is only slightly affected by the back pressure beyond about 4 mm. The translational temperature, however, is much more sensitive as indicated by figure 20(*b*). The effect of the residual gas is first felt at a radial distance of 3 mm from the centreline.

Consideration is now given to comparison of the numerical results with the measured data. To facilitate taking high-spatial-resolution experimental data, only the density in the $J = 1$ rotational state is measured. These measurements are taken along the plume centreline. In the present study, the corresponding numerical prediction is calculated using the DSMC results obtained for the total number density and the rotational temperature. These are combined in the usual equilibrium relation to determine the number density in the first rotational level. The numerical and experimental results are compared in figure 21. It should be noted that each experimental data point is obtained over a volume that is 4 mm in length axially. The measurements resemble the variation in total number density shown in figure 18(*a*). The agreement between the two data sets is remarkably good. Although the computed shock location is further from the nozzle exit, the peak value is well predicted. While difficult to discern in the experimental data, the secondary compression predicted

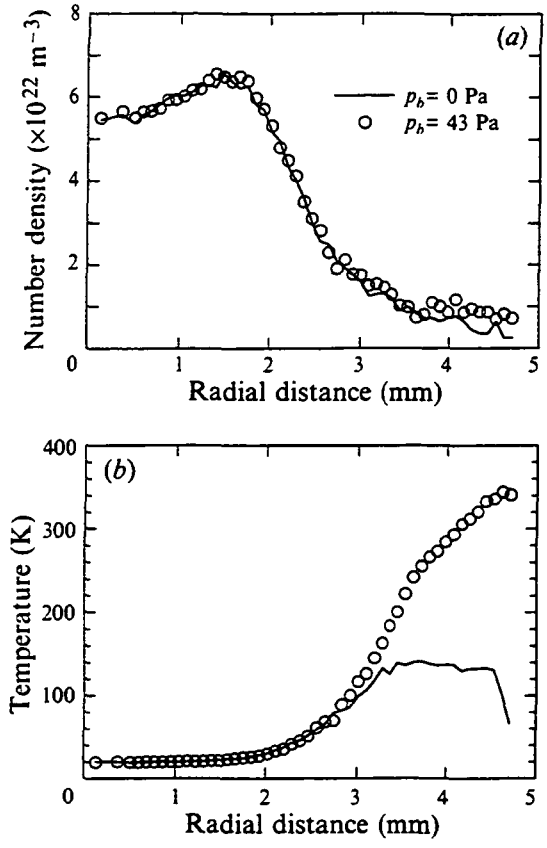

FIGURE 20. Comparison of radial profiles for (*a*) number density and (*b*) temperature, near the nozzle exit plane obtained in vacuum and at finite back pressure.

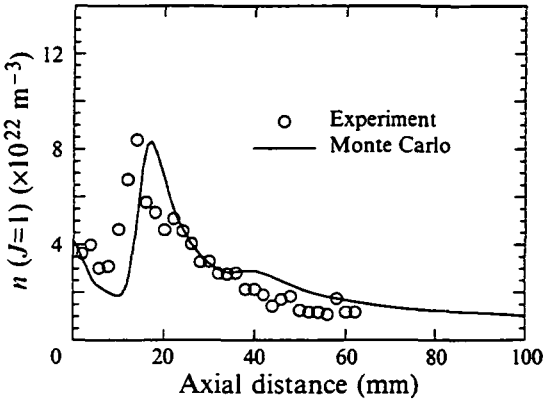

FIGURE 21. Comparison of measured and calculated data for the density of the $J = 1$ state along the plume centreline at a background pressure of 43 Pa.

numerically is not inconsistent with the measurements. Given the complicated fluid mechanics and physics of these flows, and the uncertainty in the spatial distribution of the residual pressure, this degree of agreement is very satisfying. The most obvious explanation for the difference in shock location is that the back pressure is higher at the DSMC boundaries than at the measuring point, which is further downstream. This

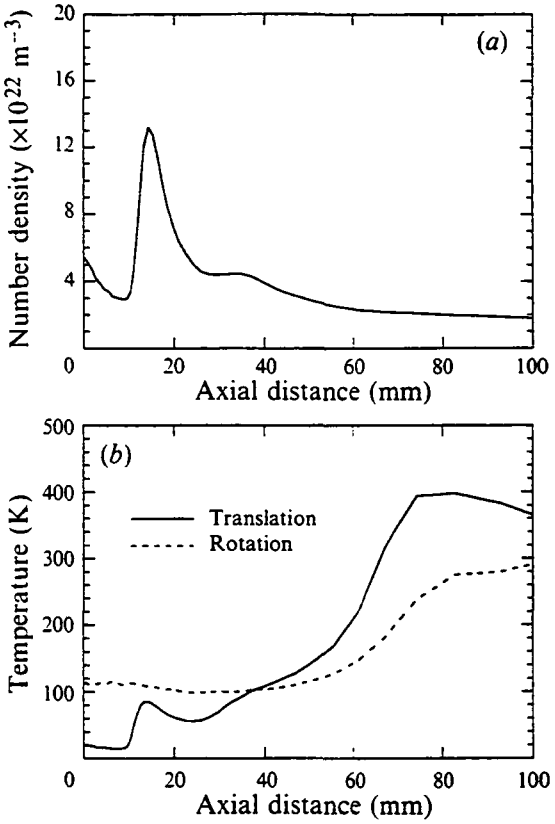

FIGURE 22. (*a*) Number density and (*b*) translational and rotational temperature, along the plume centreline computed with the DSMC method at a background pressure of 56 Pa.

difference would move the shock position back in the simulation slightly downstream of the measured position. It is certainly possible that, locally along the axis, the back pressure may be higher than the value measured experimentally, thus pushing the shock closer to the nozzle exit. It would be difficult to include this type of behaviour in the numerical analysis.

The results obtained at higher residual pressures in the test chamber are now considered. The density and temperature profiles for $p_b = 56$ Pa computed along the plume centreline are shown in figures 22(*a*) and 22(*b*). The results show the same trends as those obtained for the lower value of p_b. The shock is moved closer to the nozzle exit plane, and is now stronger. The peak in translational temperature is reached sooner. Comparison with the experimental data shown in figure 23 is once again very good. As before, the precise shock location is predicted slightly further downstream than that measured. Finally, the results obtained at the highest back pressure ($p_b = 67$ Pa) are shown in figures 24(*a*), 24(*b*), and 25. Comparison to the previous figures clearly illustrates the progressive increase in shock strength and movement of the shock closer to the nozzle exit plane as the back pressure is increased. In all these simulations, the DSMC shock-location prediction is slightly further from the nozzle than that observed experimentally. This gives a trend that is consistent with the idea proposed earlier that the pressure set at the DSMC boundaries may be too low since the chamber back pressure is actually measured further downstream of the nozzle. The general agreement between calculation and experiment is maintained. For the experimental data shown

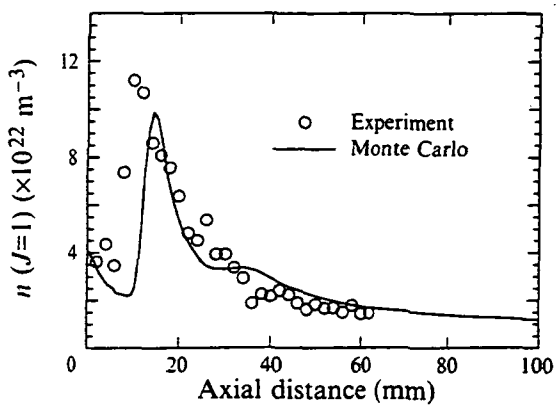

FIGURE 23. Comparison of measured and calculated data for the density of the $J = 1$ state along the plume centreline at a background pressure of 56 Pa.

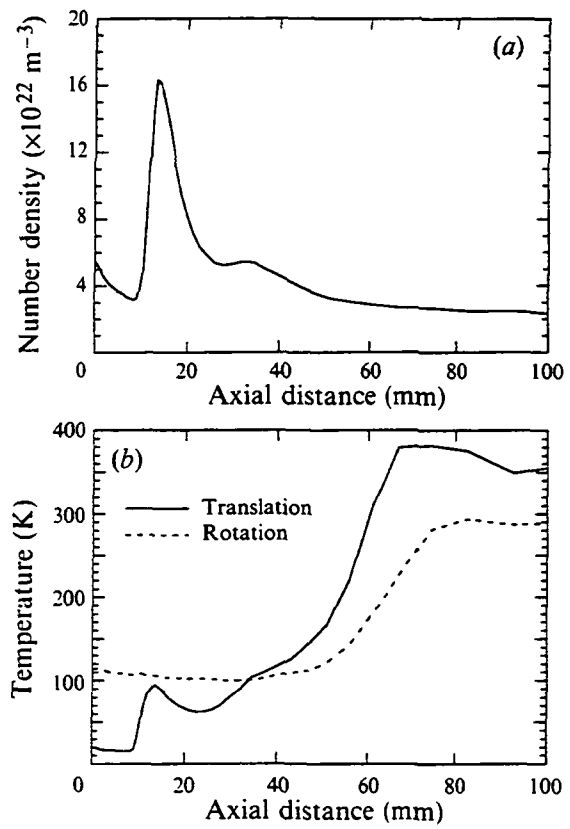

FIGURE 24. (*a*) Number density and (*b*) translational and rotational temperature, along the plume centreline computed with the DSMC method at a background pressure of 67 Pa.

in figure 25 it appears that the measurements at the nozzle exit plane are affected by the back pressure. Clearly, operation of the facility at higher pressures will produce a flow that is not anywhere representative of the plume expanding from the thruster under flight conditions. Simulation of flows at higher values of p_b would require

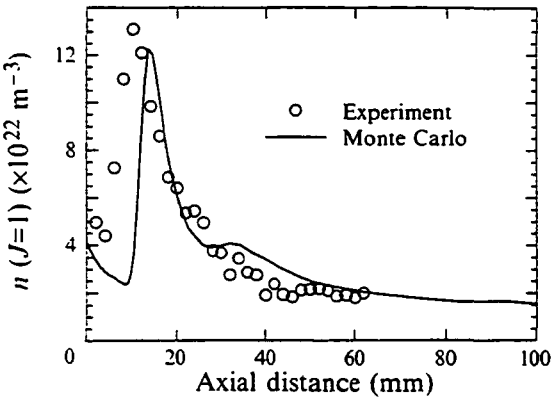

FIGURE 25. Comparison of measured and calculated data for the density of the $J = 1$ state along the plume centreline at a background pressure of 67 Pa.

Rankine–Hugoniot	$p_b = 43$ Pa	$p_b = 56$ Pa	$p_b = 67$ Pa
5.74	4.47	4.79	5.19

TABLE 3. Density ratio across first shock wave in jet expansion

simultaneous computation of the nozzle and plume flows. At $p_b = 67$ Pa, there is a small amount of flow of the residual gas into the nozzle. This is considered a second-order effect for the results presented. However, at higher pressure, this flow would become more significant and could lead to a region of separated flow inside the nozzle.

It is observed in the density profiles along the jet centreline that when the chamber pressure is increased the shock strength also increases. It is informative to compare the rise in density across the first shock wave predicted by the DSMC method for each value of p_b with the continuum Rankine–Hugoniot theory. At the point where the density first starts to rise in figures 18(*a*), 22(*a*), and 24(*a*), the local Mach number is about 10. The Rankine–Hugoniot theory predicts a density ratio (ρ_2/ρ_1) across a normal shock for a diatomic species of 5.74 at this condition. Each of the density rises obtained from the three DSMC simulations is listed in table 3. As the residual pressure is increased, the density ratio increases and approaches the theoretical value. The density rise in the expanding flow is lower than that predicted by theory owing to non-equilibrium and viscous effects. At the onset of the density rise, there is strong thermal non-equilibrium between the translational and rotational modes. Through the shock wave, low-density collisional effects give rise to non-continuum behaviour. While similar in nature, these flow-field structures are not Mach disks: the flow remains supersonic downstream of the maximum density.

A final note concerns the computational resources required to perform the plume simulations reported here. The solution times required by the DSMC method for the calculations with finite back pressures increase with p_b. For the most expensive case of $p_b = 67$ Pa, a total of 15 h on a work-station is required. The simulation of expansion into vacuum is the least expensive and requires about 3 h.

5. Conclusions

Advanced numerical and experimental methods were applied to investigate the low-density supersonic flow of a hydrogen jet. For the nozzle flow, it was found that the flow is in strong rotational non-equilibrium. A new rotational model was developed for the Monte Carlo method that was employed to compute the flow field. Computation of rotational temperature in the nozzle exit plane was found to be sensitive to the rate of rotational relaxation employed in the simulation. Comparison of the computed results with the experimental data was quite good and permitted the rotational relaxation time for hydrogen to be estimated. Fine details in the flow field, such as a small decrease in density and corresponding small increase in rotational temperature on the axis in the nozzle exit plane, were observed in both simulation and experiment. It was concluded that the Monte Carlo technique offers accurate prediction of the non-equilibrium flows produced in small nozzles used for low-thrust propulsion applications.

Detailed experimental and numerical results were also obtained for the interaction region of the hydrogen thruster plume expanding into a finite back pressure. Despite the low densities involved, the characteristic phenomena involving formation of shock and expansion waves were observed. Direct comparison of the experimental data and numerical results gave very good agreement along the plume centreline. There were two significant findings from this portion of the present study. First, for this particular facility, there was only a small region of the plume centreline that was unaffected by the back pressure. At the lowest pressures achieved, this region extended to 10 mm along the centreline: this was less than 3 nozzle diameters. It is likely that interference effects first occurred in the radial direction at a much shorter distance from the nozzle. The second important conclusion was that the DSMC method is a very useful technique for calculation of low-density expanding flows. The complex fluid mechanics combined with strong viscous and non-equilibrium effects makes modelling of these flows challenging. The direct comparisons made in this study with experimental measurements indicated that the DSMC technique is capable of accurately simulating such complicated phenomena. It therefore appears that the method is appropriate for assessing the important question of plume interference effects for similar experimental vacuum facilities.

Support by NASA Lewis Research Center for I.D.B. (Grant NAG3-1451) with Dr P. F. Penko as technical monitor is gratefully acknowledged. The work of D.R.B. and M.A.C. was supported in part by NASA Lewis Research Center with Dr F. M. Curran as technical monitor (Grant NAG3-1040), and by Norton Co. (Grant ACH-116820).

REFERENCES

BIRD, G. A. 1976 *Molecular Gas Dynamics*. Clarendon.

BIRD, G. A. 1981 Monte Carlo simulation in an engineering context. In *Rarefied Gas Dynamics*, Part 1, pp. 239–255. AIAA.

BOITNOTT, C. A. & WARDER, R. C. 1971 Shock tube measurements of rotational relaxation in hydrogen. *Phys. Fluids* **14**, 2312–2316.

BOYD, I. D. 1990 Analysis of rotational nonequilibrium in standing shock waves of nitrogen. *AIAA J.* **28**, 1997–1999.

BOYD, I. D. 1991 Vectorization of a Monte Carlo method for nonequilibrium gas dynamics. *J. Comput. Phys.* **96**, 411–427.

BOYD, I. D., JAFRY, Y. R. & VANDEN BEUKEL, J. 1994 Particle simulations of helium microthruster flows. *J. Spacecraft* **31**, 271–277.

BOYD, I. D., PENKO, P. F., MEISSNER, D. L. & DEWITT, K. J. 1992 Experimental and numerical investigations of low-density nozzle and plume flows of nitrogen. *AIAA J.* **30**. 2453–2461.

FORD, A. L. & BROWN, J. C. 1973 Rayleigh and Raman cross sections for the hydrogen molecule. *Atomic Data* 5, 305–313.

GALLAGHER, R. J. & FENN, J. B. 1974 Rotational relaxation of molecular hydrogen. *J. Chem. Phys.* **60**. 3087–3091.

JENNINGS, D. E., RAHN, L. A. & OWYOUNG, A. 1985 Laboratory measurement of the S(9) pure rotation frequency. *Astro. J.* **291**. L15–L18.

LAMBERT, J. D. 1977 *Vibrational and Rotational Relaxation in Gases*. Clarendon.

LENSCH, G. & GRONIG, H. 1977 Experimental determination of rotational relaxation in molecular hydrogen and deuterium. In *Proc. 11th Intl Symp. Shock Tubes and Shock Waves*. pp. 132–139. University of Washington Press.

LUMPKIN, F. E., HAAS, B. L. & BOYD, I. D. 1991 Resolution of differences between collision number definitions in particle and continuum simulations. *Phys. Fluids* A 3, 2282–2284.

MCQUARRIE, D. A. 1973 *Statistical Thermodynamics*, p. 107. University Science Books.

PARKER, J. G. 1964 Comparison of experimental and theoretical vibrational relaxation times for diatomic gases. *J. Chem. Phys.* **41**. 1600–1609.

PENKO, P. F., BOYD, I. D., MEISSNER, D. L. & DEWITT, K. J. 1993 Measurement and analysis of a small nozzle plume in vacuum. *J. Propulsion* **9**, 646–648.

VALENTINI, J. J. 1987 *Laser Spectroscopy and Its Applications*, p. 516. Marcel Dekker.

VIERS, D. K. & ROSENBLATT, G. M. 1987 Raman line positions in molecular hydrogen: H_2, HD, HT, D_2, DT, and T_2. *J. Mol. Spec.* **121**. 401–419.

WEBER, A. 1973 *The Raman Effect*, vol. 2, p. 732. Marcel Dekker.

WOLNIEWICZ, L. 1983 The $X^1\Sigma_g^+$ state vibration-rotational energies of the H_2, HD, and D_2 molecules. *J. Chem. Phys.* **78**, 6173–6181.

N15

AIAA - 95 - 1956

Raman Scattering Measurements of Molecular Hydrogen in an Arcjet Thruster Plume

D.R. Beattie and Mark A. Cappelli

High Temperature Gasdynamics Laboratory
Department of Mechanical Engineering
Stanford University
Stanford, California

26th AIAA Plasmadynamics and Lasers Conference
June 19-22, 1995/San Diego, CA

RAMAN SCATTERING MEASUREMENTS OF MOLECULAR HYDROGEN IN AN ARCJET THRUSTER PLUME

Doug R. Beattie* and Mark A. Cappelli**

High Temperature Gasdynamics Laboratory
Department of Mechanical Engineering
Stanford University
Stanford, CA 94305-3032

Abstract

Raman scattering measurements of molecular hydrogen density and temperature were made in the plume of a 1 kW-class hydrogen arcjet thruster. Pulsed-laser excitation was used to improve the signal-to-noise ratio in this high-background environment. Quantum-limited detection was achieved through the use of gated photon counting and a high-power Nd:YAG laser. Radial profiles of rotational temperature and density at the exit plane were measured for 5 power levels. In all cases the profiles were asymmetric about the arcjet centerline. The rotational temperatures were compared with the translational temperatures of atomic hydrogen from LIF studies and found to be significantly lower. This result suggests that this flow, like the cold flow, is not in translational-rotational equilibrium.

Introduction

Arcjet thrusters are a type of electric-powered rocket which can be used for propulsion of space vehicles. They offer higher exhaust velocities than conventional chemical rockets; hence they require less propellant mass to deliver a given impulse. For certain missions, arcjets offer a good compromise between the often conflicting requirements of small size and low mass for the thruster and propellant combined. They are now being commercially employed in station-keeping roles on communication satellites.

There is a desire to increase both the thermal efficiency and exhaust velocities of current designs in order improve cost effectiveness and allow for use in a wider range of missions. Furthermore, there is interest in developing higher thrust versions which could be used in applications such as orbit transfer. Such improvements will depend partly on a better understanding of the plasma and gas dynamic processes undergone in the arcjet nozzle.

Currently both numerical analysis and experimental studies are being used to investigate flow properties in low-power arcjet thrusters. Attempts at modelling the plasma flow in hydrogen arcjet thrusters use both continuum (Butler et al. 1994, Miller and Martinez-Sanchez 1993) and Monte Carlo techniques (Boyd et al. 1994). These models are useful in understanding the various loss mechanisms in an arcjet, including anode radiation, ionization, dissociation and other frozen-flow losses. Numerical models with accurate predictive capabilities will also be very helpful by allowing parametric studies to be performed much more easily than by testing prototypes in the laboratory. However, experimental measurements of relevant physical parameters in both the nozzle and plume are needed to validate these models. Of particular interest are density, temperature and velocity measurements of atomic hydrogen (H) and molecular hydrogen (H_2).

Recent studies have relied primarily on optical diagnostics such as emission, absorption, and fluorescence. Optical techniques have the potential advantages of high spatial resolution and minimal perturbation to the flow field and most efforts have probed atomic hydrogen because of the large number of transitions in the visible spectrum. These experiments have included measurements of: H velocity and translational temperature using laser induced fluorescence (LIF) of the H_α Balmer line (Liebeskind et al. 1993), H density using vacuum ultraviolet absorption (Manzella and Cappelli 1992) and multiphoton LIF (Pobst et al. 1995), and H temperature and electron density using emission (Storm and Cappelli 1994).

---

* Research Assistant

** Associate Professor, Member AIAA

Molecular hydrogen (like other homonuclear, diatomic molecules) does not undergo radiative transitions between rotational or vibrational levels in the ground electronic state since it does not have a dipole moment. As a result, one can not use emission, absorption or fluorescence techniques to study these energy states. Until now, measurements of H_2 properties have been limited to spatially averaged absorption measurements (Pollard 1992) and density and temperature measurements in the distant plume using mass sampling spectroscopy (Pollard 1993). However, numerical simulations (Butler et al. 1994) have predicted that ~95% of the mass flow at the exit plane is molecular hydrogen so it is important to have experimental data on H_2 exit-plane properties.

The research described in this paper involved making measurements of molecular hydrogen properties in the plume of a hydrogen arcjet thruster. Spontaneous Raman scattering was chosen as a suitable technique for making spatially resolved measurements of the ground electronic state of H_2. Raman scattering is a linear, inelastic, two-photon scattering process. It can be used to measure the density of various rotational and vibrational levels, allowing calculation of the total H_2 density and the rotational and vibrational temperatures. Measurements of the Doppler shift of the scattered light can provide the velocity distribution function, which gives both the bulk velocity and the translational temperature. The primary disadvantage of Raman scattering is the very low signal levels involved. Typical scattering cross sections are 10^{-33} m^2, or about 1000 times smaller than Rayleigh (elastic) scattering cross sections. As a result, the data collection process is generally very slow and it can be difficult to detect the signal in a luminous background, such as an arcjet thruster plume.

In this study, the population of various rotational levels was measured, giving the rotational temperature and density. Initial measurements (Beattie and Cappelli 1992) were made in the plume of a cold-flowing arcjet thruster. These flow conditions were well suited to developing both the experimental and numerical methods. Exit-plane profiles showed strong two-dimensionality in the flow, and also a moderate degree of asymmetry about the axis. The measured rotational temperatures on centerline were significantly higher than expected for isentropic flow, suggesting that the flow was not in rotational-translational equilibrium. Comparison of the results with Monte Carlo numerical simulations (Boyd et al. 1994) confirmed this result. Good agreement was obtained between experimental and modeling results for density and rotational temperature profiles by using a slightly lower value of the rotational relaxation rate than the accepted values. Axial profiles of density were also measured at various back pressures. Shock structure was visible downstream of the exit plane, and the shock behavior with changing pressure was consistent with gas dynamic theory and the simulation results.

Theory

The Raman effect is a linear, inelastic, two-photon scattering process. An incident photon of frequency v_0 scatters off a particle, causing a transition in the particle from the initial state i to a final state f. Since the system energy is conserved, the scattered photon must be shifted in energy correspondingly:

$$\begin{aligned} \varepsilon_{\mathrm{mol},i} + \varepsilon_{v,i} &= \varepsilon_{\mathrm{mol},f} + \varepsilon_{v,f} \\ \Delta\varepsilon_v &= -\Delta\varepsilon_{\mathrm{mol}}, \end{aligned} \tag{1}$$

where $\varepsilon_{\mathrm{mol}}$ and ε_v are the energy of the molecule and photon respectively. In the harmonic oscillator-rigid rotor approximation, the molecular energy can be written as:

$$\varepsilon_{\mathrm{mol}} = \varepsilon_{\mathrm{trans}} + \varepsilon_{\mathrm{rot}} + \varepsilon_{\mathrm{vib}} + \varepsilon_{\mathrm{elec}} + \varepsilon_{\mathrm{nucl}}. \tag{2}$$

The Raman transitions under consideration here all begin and end in the ground electronic state. Furthermore, changes in the translational and nuclear energy components as a result of the Raman scattering process are small. Hence the changes in $\varepsilon_{\mathrm{mol}}$ can be approximated as changes in the rotational and vibrational states, allowing Eq. (1) to be written as:

$$\Delta\varepsilon_v = -\Delta\varepsilon_{\mathrm{mol}}(v, J). \tag{3}$$

For a diatomic molecule, the selection rules are $\Delta J = 0, \pm 2$ and $\Delta v = 0, \pm 1$, where $\Delta J = J_f - J_i$ and $\Delta v = v_f - v_i$. The case of $\Delta J = 0$ and $\Delta v = 0$ is actually Rayleigh scattering. Scattering is designated as purely rotational when $\Delta J = \pm 2$ and $\Delta v = 0$, purely vibrational when $\Delta J = 0$ and $\Delta v = \pm 1$, and rotational-vibrational when $\Delta J = \pm 2$ and $\Delta v = \pm 1$.

Theoretical Raman spectra were calculated for H_2 in equilibrium at a given temperature and density. The Raman energy shifts were taken from the experimentally-measured values of Veirs and Rosenblatt (1987) for pure rotational, vibrational and rotational-vibrational transitions from $v_i = 0$ and $J_i = 0$ through $J_i = 5$ (6 for Q branch). These measurements are in excellent agreement with the quantum mechanical calculations of Wolniewicz (1983), differing by less than one part in 10^5.

The H_2 Raman line shape is primarily determined by Doppler and collisional effects (Rahn et al. 1991). At the low pressures in these experiments, the transitions will be primarily Doppler broadened. The Doppler width for Raman scattering is different than for emission or

absorption, since two photons are involved. By solving the equations of conservation of energy and momentum, Weber (1973) shows that the Doppler width is:

$$\Delta\nu_{\mathrm{FWHM}} = \frac{2}{c}\left(2\ln\frac{2kT}{m_{\mathrm{mol}}}\right)^{\frac{1}{2}}\left[4\left(\nu_0^2 + \nu_0\Delta\nu_{\mathrm{R}}\right)\sin^2\frac{\theta}{2} + \Delta\nu_R^2\right]^{\frac{1}{2}} \tag{4}$$

where θ is the angle between the incident and scattered light ($\theta = 180°$ implies forward scattering), $\Delta\nu_{\mathrm{R}}$ is the Raman frequency shift, and FWHM denotes the full-width at half maximum.

Raman cross sections for transitions from $v_i = 0$ and $J_i = 0$ through $J_i = 3$ were calculated by Ford and Browne (1973) using quantum mechanical evaluations of the dynamic polarizability. Their results are in good agreement with previous experimental measurements and calculations. The cross sections were obtained at the excitation wavelength of interest using their 8th order expansion in wavelength. Cross sections for states $J_i = 4$ and higher were not available, so they were estimated from the $J_i = 3$ value taking into account the ν_{R}^3 frequency dependence.

In a typical Raman experiment, the incident photons are provided by a laser beam at a rate $\dot{N}_{\mathrm{L}}$ and light scattered into a solid angle $d\Omega$ is collected from a beam segment of length l. The rate of Raman photons scattered for a transition from the initial state i to the final state f is:

$$\dot{N}_{i,f} = \dot{N}_L l n_0 \frac{n_i}{n_0}\left(\frac{d\sigma}{d\Omega}\right)_{i,f} d\Omega. \tag{5}$$

where $\dot{N}_{\mathrm{L}}$ is the incident laser photon rate, n_0 is the molecular number density, n_i/n_0 is the population fraction in the initial state, and $(d\sigma/d\Omega)_{i,f}$ is the differential Raman cross section for the transition from i to f.

The population fractions n_i/n_0 were calculated assuming the gas was in local thermodynamic equilibrium (LTE) with the molecules obeying Boltzmann statistics, in which case:

$$\frac{n_i}{n_0} = \frac{g_i e^{-\epsilon_i/kT}}{\sum_i g_i e^{-\epsilon_i/kT}} = \frac{g_i e^{-\epsilon_i/kT}}{q} \tag{6}$$

where q is the molecular partition function. Neglecting interactions between all energy modes except rotational and nuclear, the total molecular wavefunction for H_2 may be expressed as follows:

$$\psi_{\mathrm{total}} = \psi_{\mathrm{trans}}\psi_{\mathrm{vib}}\psi_{\mathrm{elec}}\psi_{\mathrm{rot,nucl}} \tag{7}$$

which implies:

$$\epsilon_{\mathrm{total}} = \epsilon_{\mathrm{trans}} + \epsilon_{\mathrm{vib}} + \epsilon_{\mathrm{elec}} + \epsilon_{\mathrm{rot,nucl}}. \tag{8}$$

Hence the partition function can be factored as follows:

$$q = q_{\mathrm{trans}}q_{\mathrm{elec}}q_{\mathrm{vib}}q_{\mathrm{rot,nucl}} \tag{9}$$

allowing the population fraction for a particular state of an energy mode to be calculated independently of the other modes. For example, the population fraction in the vibrational state v is:

$$\frac{n(v)}{n_0} = \frac{g_{\mathrm{vib}}(v)\,e^{-\epsilon_{\mathrm{vib}}(v)/kT}}{\sum_v g_{\mathrm{vib}}(v)\,e^{-\epsilon_{\mathrm{vib}}(v)/kT}} \tag{10}$$

which only requires knowledge of the vibrational energy levels and degeneracies. The vibrational populations were calculated using the harmonic-oscillator approximation with $\Delta\epsilon_{\mathrm{vib}}(v = 0 \rightarrow v = 1)$ from Wolniewicz (1983) used as the vibrational energy constant. The error introduced by making the harmonic approximation is small at the temperatures involved in this study, since most of the molecules are in the ground vibrational state (>95% at $T < 2000$ K). The rotational energies were taken from a 6 parameter fit to experimental data provided by Jennings et al. (1985). These energy levels agree to better than 1 part in 10^4 with the previously mentioned results of Veirs and Rosenblatt (1987) and Wolniewicz (1983). The electronic partition function was taken as unity. Furthermore, all measurements taken were integrated over essentially all translational velocities, so the translational partition function can be neglected.

Unlike the other energy modes, the rotational and nuclear modes interact, so their populations may not be calculated independently. A hydrogen nucleus (proton) is a fermion with spin of $I = 1/2$. As a result, the wavefunction of an H_2 molecule must be antisymmetric with respect to interchange of the two nuclei. This property results in a restriction on the symmetry of the rotational wavefunction. For H_2 in the ground electronic state, the electronic wavefunction is symmetric. In addition, the translational and vibrational wavefunctions are both symmetric. The only components of ψ_{total} which can be antisymmetric are ψ_{nucl} and ψ_{rot}. There are 4 possible nuclear spin states of the 2 nuclei: 3 symmetric states with parallel spins (often referred to as ortho-hydrogen), and 1 antisymmetric state with opposed spins (para-hydrogen). The rotational wavefunctions are symmetric for even J and antisymmetric for odd J. Hence there are only two ways of satisfying the antisymmetric constraint on the total wavefunction: (i) coupling a symmetric nuclear spin state (ortho) with an antisymmetric rotational state (odd J) or (ii) coupling the antisymmetric nuclear spin state (para) with a symmetric rotational state (even J).

The rotational-nuclear partition function is calculated as follows:

$$q_{\text{rot,nucl}} = \sum_{J=0}^{\infty} g_{\text{nucl}} g_{\text{rot}} e^{-\varepsilon_{\text{rot}}/kT} \qquad (11)$$

where g_{rot} is the rotational degeneracy $(2J + 1)$, g_{nucl} is the nuclear degeneracy (3 for odd J, 1 for even J), and the nuclear state energy $\varepsilon_{\text{nucl}}$ is neglected. The nuclear degeneracy ratio of 3:1 (ortho-para) results in a 3:1 statistical weighting of the odd-even J states. At temperatures above 300 K, the upper rotational states are sufficiently populated in equilibrium that the ortho-para ratio is in fact 3:1. At lower temperatures, the population increasingly fills the $J = 0$ state, and the equilibrium ortho-para ratio decreases. In the limit as T approaches 0, the equilibrium ortho-para ratio also approaches 0.

Using the previously outlined techniques, the predicted signal from H_2 at reference conditions (T = 300 K, P = 101 325 Pa) is shown in Figure 1 for various rotational and/or vibrational transitions from $v_i = 0$. The plot shows the intensity versus wavelength for excitation by a 2 W laser at 532 nm, with l = 2 mm, $d\Omega$ = 0.024 sr, and a detection system efficiency (detected photons per collected photon) of η_{sys} = 0.005. The Rayleigh line is shown for comparison, though it is ~1000 times more intense than the strongest Raman transition. The lowest 4 rotational states are shown, since they are the only ones with a significant population at this temperature. The pure rotational transitions, near the Rayleigh line, are the most intense at up to 6000 photon s^{-1}. However the slightly weaker pure vibrational transitions near 680 nm were used in these experiments for two reasons. First, they are well separated from the laser wavelength, which makes it easier to separate them from elastically scattered light due to both Rayleigh scattering and reflections off the arcjet and chamber walls. Second, since the various transitions are close together they can be measured in a single, short spectral scan. These transitions are shown in more detail in Figure 2. To indicate how these features might appear with typical instrument resolution, the spectrum was also convolved with a triangular function of 0.2 nm FWHM. Under these conditions, all the peaks are resolved except $J = 0$ and $J = 1$. However, only the wings of these two lines overlap and the centerline intensity is unaffected by the adjacent transition. Table 1 shows a summary of these calculations, including the transition wavelengths, cross sections and intensities. The Q-branch transitions are highlighted and Rayleigh scattering information is included for comparison.

In order to determine if Raman scattering is a feasible technique for use in the arcjet plume, Raman spectra were calculated for the estimated flow conditions. The average exit-plane density was estimated at 1×10^{22} m^{-3} using 6000 m s^{-1} as a typical mass-averaged

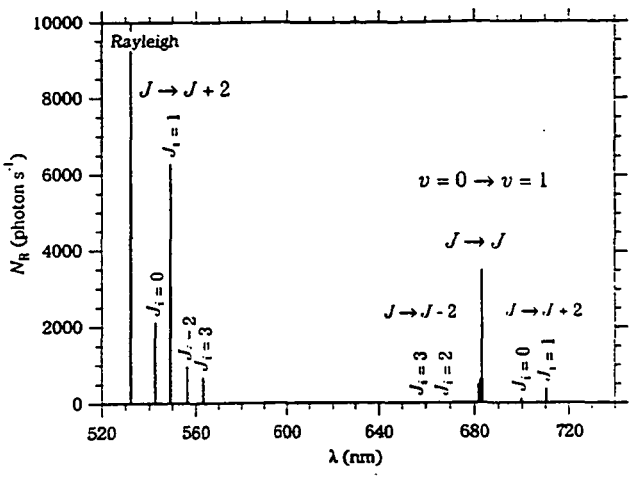

Figure 1 Raman intensity versus wavelength for various rotational and/or vibrational transitions from H_2 at reference conditions.

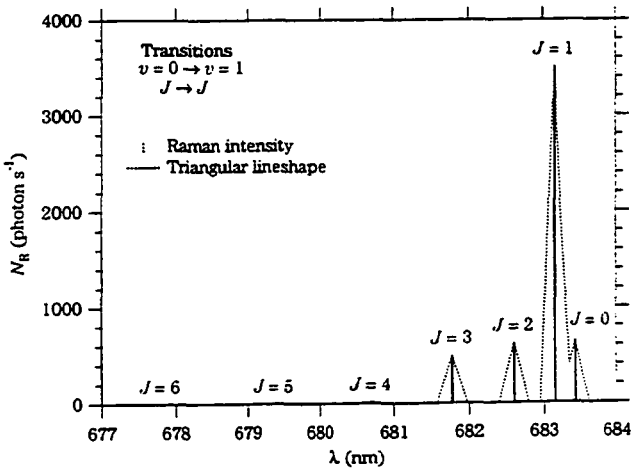

Figure 2 Raman intensity versus wavelength for pure vibrational transitions under the same conditions as Figure 1.

exhaust velocity. The rotational temperature was estimated to be 1500 K based on the absorption measurements of Pollard (1993). Using these conditions, the spectrum shown in Figure 3 was calculated using the same setup parameters as for the reference calculation. The maximum estimated signal level is 0.6 photon s^{-1} from the $J = 3$ transition. At these higher temperatures, the population is spread out over more rotational levels, with significant population in all 7 of the rotational states shown. The coupling of the rotational degeneracy to the nuclear spin degeneracy is evident from the alternating high-low intensity of the odd-even transitions. These very low signal estimates suggest that detection of the Raman scattering will be difficult, especially in the highly luminous background of the plume. Long collection periods will likely be required in order to accumulate statistically significant data.

Table 1 Summary of Raman transition data at reference conditions using an incident wavelength of 532.1 nm, with the Q-branch transitions highlighted.

v_i	v_f	J_i	J_f	λ (nm)	$\Delta\varepsilon_R/hc$ (m^{-1})	n_i/n_0	σ (10^{-33} m^2)	$\dot{N}_R$ (s^{-1})
0	0	0	2	542.326	35437	0.128	3.292	2115.4
0	0	1	3	549.258	58709	0.657	1.914	6295.7
0	0	2	4	556.204	81446	0.117	1.635	960.3
0	0	3	5	563.102	103470	0.092	1.485	682.5
0	1	0	0	683.421	416120	0.128	1.000	642.5
0	1	1	1	683.145	415528	0.657	1.067	3509.1
0	1	2	2	682.595	414349	0.117	1.065	625.7
0	1	3	3	681.777	412590	0.092	1.079	495.8
0	1	4	4	680.695	410259	0.004	1.084	23.1
0	1	5	5	679.359	407370	0.001	1.090	5.5
0	1	6	6	677.782	403945	0.000	1.098	0.1
0	1	0	2	699.515	449785	0.128	0.201	128.9
0	1	1	3	710.201	471294	0.657	0.117	383.6
0	1	2	4	720.646	491703	0.117	0.032	18.5
0	1	3	5	730.725	510842	0.092	0.021	9.9
0	1	2	0	667.263	380686	0.117	0.023	13.6
0	1	3	1	656.805	356824	0.092	0.032	14.6
0	0	0	0	532.100	0	0.128	109.403	70310.4
0	0	1	1	532.100	0	0.657	111.182	365710.2
0	0	2	2	532.100	0	0.117	111.462	65460.9
0	0	3	3	532.100	0	0.092	112.522	51714.8

Experiment

The arcjet thruster uses an electric arc to heat propellant to high temperatures, often 10 000 to 20 000 K. The hot gases are then expanded through a Laval nozzle. The arc passes from the cathode to the nozzle walls, which act as the anode. The arcjet nozzle is machined from a tungsten alloy containing 98% W and 2% Th. Both the converging and diverging sections are conical, with half angles of 30° and 20° respectively. The nozzle diverging section has a 225:1 area ratio relative to the 0.64 mm diameter throat. The cathode is machined from a rod of the same alloy, with a tip angle matching that of the converging section. The cathode is installed by placing it in contact with the converging section, then pulling it 0.7 mm back. A drawing of the nozzle is shown in Figure 4. The anode is held by a stainless-steel anode housing which is bolted to the anode body. The cathode is insulated from the housing with a boron nitride sleeve. The hydrogen is injected tangentially through two small passages in the injector disk upstream of the cathode tip. The swirl imparted by this injection mechanism is believed to help stabilize the arc, primarily during startup.

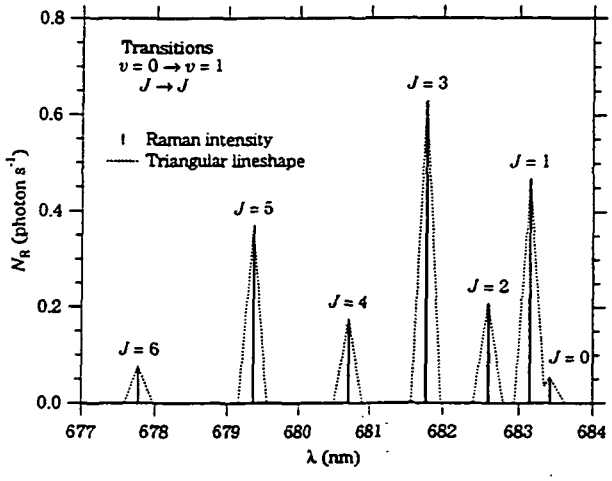

Figure 3 Predicted Raman intensity versus wavelength at the exit plane of the arc-ignited thruster.

The arcjet used for these experiments was a 1kW class NASA laboratory hydrogen thruster. The thruster was operated in a vacuum chamber 1.09 m long and 0.53 m in diameter with optical access through 75 mm diameter ports.It was mounted on a two-axis axial and radial translation stage. Twelve optical ports were located at 30° intervals around the circumference of the tank, with additional ports in the endwall. The tank was evacuated by two Roots blowers backed by mechanical roughing pumps with a total capacity of 1.2 m^3 s^{-1}. This system was capable of maintaining a back pressure of 43 ±2 Pa while flowing 13.3 mg s^{-1} hydrogen.

In the previous cold flow experiments (Beattie and Cappelli 1992, Boyd et al. 1994, Beattie 1995) a CW laser was used. However, in order to improve the signal-to-noise ratio (SNR), a pulsed laser excitation scheme was chosen here. The Nd:YAG laser used was a Spectra Physics DCR-1 flashlamp-pumped, solid-state model. The output was frequency doubled using a type II KDP crystal, and the 532 nm light was separated using two dichroic filters. When operating at a 10 Hz repetition rate, the laser was capable of producing 200 mJ pulses at 532 nm with a 10 ns length.

Initially, the laser beam was sent axially into the arcjet through a port in the chamber endwall, as in the cold-flow experiments. However, the beam intensity at nozzle was so high that each laser pulse created a tungsten plasma and after a relatively short period of time, the nozzle was visibly eroded by the laser. In order to allow full laser energy to be utilized, the setup was modified to send the laser beam radially into the arcjet plume. The laser was sent in through a port 30° from vertical and directly out through the opposite port (Figure 5).

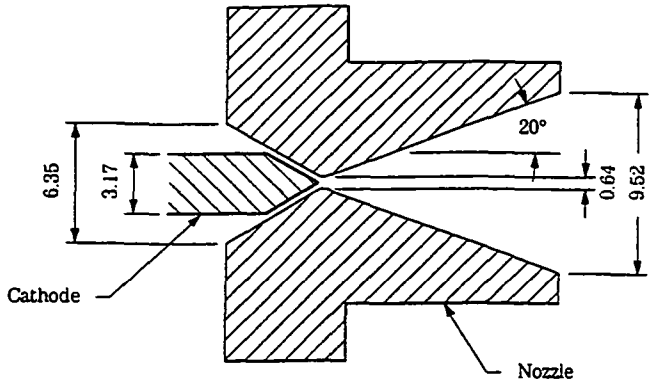

Figure 4 Drawing of the 1 kW-class arcjet nozzle and cathode, showing key dimensions in mm.

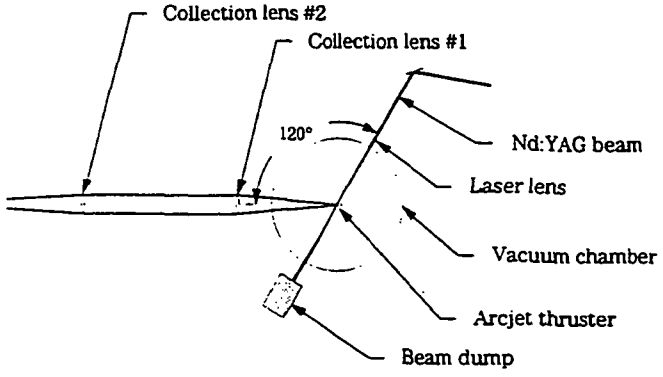

Figure 5 Schematic diagram of laser and collection optics (front view).

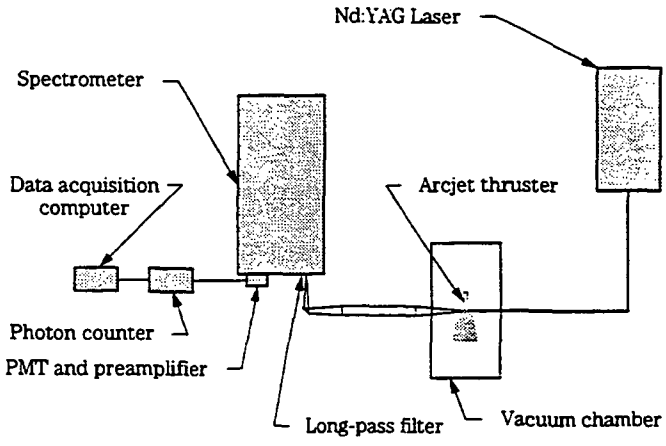

Figure 6 Schematic diagram of experimental apparatus (plan view)

The scattered light was collected at $\theta = 120°$ through a port located in the same circumferential plane as the laser at optical table level, and was focused onto a spectrometer entrance slit with an achromatic two-lens system as shown in Figure 6. The collection lens (f = +400 mm, d = 76 mm) was limited to f/5.7 by the port geometry. The focusing lens (f = +600 mm, d = 76 mm) was chosen to match the spectrometer f-number. The spatial resolution was 2 mm in the radial direction, determined by the slit height, and 0.25 mm in the axial direction, determined by the slit width. The spectrometer was a 1.0 m focal length f/8.7 single-pass Czerny-Turner design (Jarrell Ash 78-466).The grating was an 1800 line/mm holographic model with high efficiency from 400 to 1000 nm. A long-pass filter (Schott OG 590) was placed before the entrance slit to further reduce the intensity of collected laser light to negligible levels (10^8). The spectrometer slits were 400 μ m giving a spectral resolution of ~0.2 nm.

Light was detected at the exit slits with a Hamamatsu R928 photomultiplier tube (PMT) which had an efficiency of 6% at 680 nm and was operated at 1000 V. The output was amplified by an integral socket/preamplifier assembly (Hamamatsu C716-01) and sent to a photon counter (SRS 400). The counter was triggered by the laser using a photodiode. The 15 ns gate width was as narrow as possible to maximize the background rejection while still being wide enough to capture the peak of the signal pulse including jitter. The gate delay was first set approximately by simultaneously monitoring the counter input signal and the gate output on a two-channel oscilloscope. To set it more accurately, the count rate was recorded for a constant level of pulsed-light input to the detector. The delay was then scanned over the time-frame of interest and set at the position of the maximum count rate.

The counter was gated to the laser pulse using a photodiode. Counts are only accumulated when the counter is gated. The photon pulse height distribution peaked at ~300 mV and the lower level discriminator was set to 100 mV. The spectrometer was scanned over the spectral region of interest and the photon counter output was recorded on a 486 computer using SRS 440 software.

The system was calibrated for absolute efficiency by measuring the Raman scattering from stagnant H_2 at a known temperature and pressure. In order to account for the different efficiency at each transition, the relative efficiency versus wavelength was measured using a tungsten strip lamp. This second calibration was necessary since the transitions from J = 4 through 6 were too weak at room temperature to be accurately measured.

Results and Analysis

Given the low signal levels expected in the arc-ignited flow, it was feasible to make measurements at only a few spatial positions. Since arcjet performance is

determined entirely by the exit plane properties, data was collected as close to the exit as possible. Measurements were taken at 5 radial locations each 2 mm apart. With spatial resolution of 2 mm radially, this mesh covered the entire exit plane with no overlapping of segments. The arcjet was positioned at z = +4.0 mm and the data acquisition program was started. The signal was recorded for 4000 laser pulses (~400 s) at each of the 5 positions across the exit plane.

Radial profiles in the arcjet plume were taken at 5 power levels: 800, 900, 1000, 1200, and 1400 W. With the hydrogen mass flow at 13.3 mg s^{-1}, the corresponding specific power levels were from 60 MJ kg^{-1} to 106 MJ kg^{-1}. A plot of the Raman signal versus radial position for the 900 W case is shown in Figure 7. The signal levels ranged from under 300 photons (0.7 photon s^{-1}) from state J = 1 to 5 photons (0.01 photon s^{-1}) from J = 6. One notable feature is that the data is not symmetrical about z = 0. This asymmetry was observed at all power levels, although to varying degrees. In order to determine if this effect was systematic, one data set was taken by scanning the arcjet up for some J values and down for the others. However, there was no correlation between the scan direction and the asymmetry. Furthermore, the plume emission provided confirmation that the arcjet was properly centered. The plume emission that was measured simultaneously with the Raman scattering using the CW gate is shown in Figure 8 for the 900 W case. Gaussian curves were fitted to the emission to check the centering and in all cases the center of the fit was within 50 μm of z = 0. The emission intensity varied with J depending on whether the Raman transition wavelength coincided with any H_2 emission lines.

The first step in the analysis was to correct the data for possible saturation effects, which arise when consecutive photons overlap within the temporal resolution of the photon counting electronics (Beattie 1995). This correction was negligible except in the calibration scans, where the J = 1 peak was reduced ~20% by saturation. Next, the contribution of the CW signal to the gated counts was subtracted, using the measured CW rejection ratio of 6.4×10^6. This amount was no more than 4 counts at the 1400 W power level and less than 1 count at 800 W. With signal levels typically 40 to 200 counts, the largest source of error was the statistical variation in N_R, with the SNR equal to $\sqrt{N_R}$. The raw data was normalized by the laser power and relative efficiency at each transition. Then a best fit was performed to the corrected data using a function which assumed that the flow was in local thermodynamic equilibrium (LTE) with rotational population distributions dictated by a rotational temperature. The two parameters in this fit (LTE fit) were the H_2 tem-

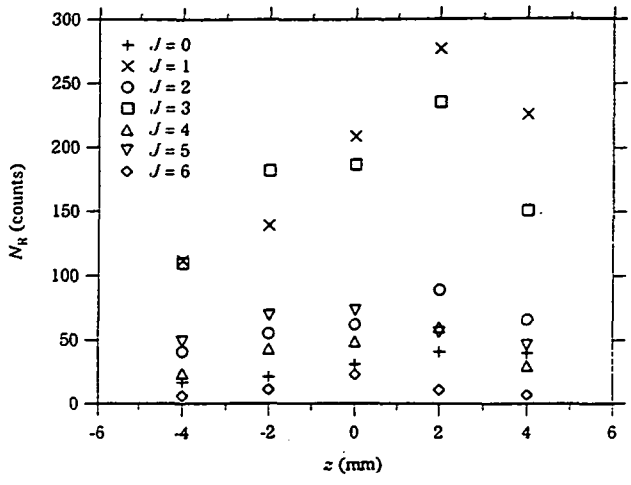

Figure 7 Raman signal versus radial position at 900 W power.

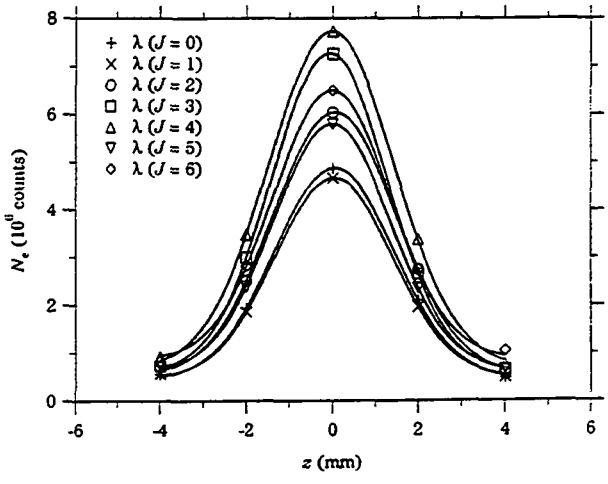

Figure 8 Plume emission signal measured simultaneously with the Raman signal shown in Figure 7.

perature and density. For the data presented here, states J = 0 through 3 were used for calibration and states J = 0 through 6 were used in the plume.

The corrected calibration data and LTE fit intensities are plotted as a function of wavelength in Figure 9 and in a Boltzmann plot in Figure 10. The data in Figure 9 is normalized by the laser pulse energy in Joules (J). The excellent agreement is primarily due to the good SNR afforded by the relatively high density at 100 Pa. The LTE fit temperature of 303 ± 9 K is consistent with the measured room temperature of 300 K. The intensity of the transitions from J = 4 through J = 6 are shown for the LTE fit, but were not measured because of their relative weakness at this temperature.

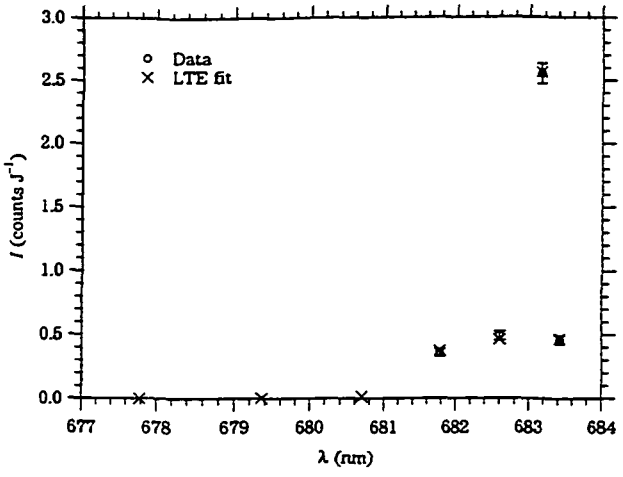

Figure 9 Normalized Raman signal versus wavelength from calibration data.

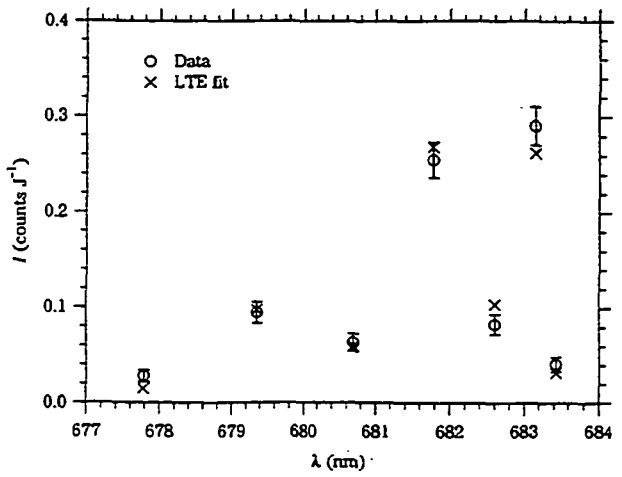

Figure 11 Normalized Raman signal versus wavelength measured at $x = 2$ mm and $z = 0$ mm while operating at $P = 900$ W.

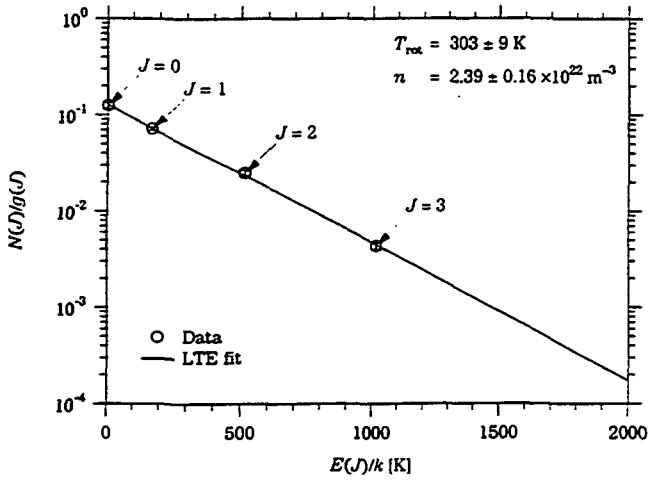

Figure 10 Boltzmann plot of rotational population fractions from Figure 9.

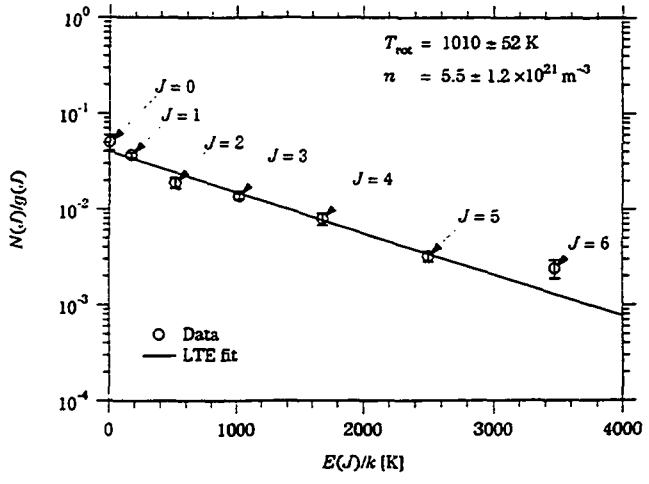

Figure 12 Boltzmann plot of data in Figure 11, showing the measured density and rotational temperature, along with the calculated pressure.

Figure 11 shows a plot of the corrected data from Figure 7 at $z = 0$ mm along with the results of the LTE fit. As an indication of how weak the scattering process is, the normalized peak signal of 0.3 photon J^{-1} corresponds to 1 detected photon for every 10^{19} laser photons. The corresponding Boltzmann plot of the data is shown in Figure 12. This data was typical in that all but 2 or 3 points fell within one standard error of the intensity fit. For data following a Poisson distribution, one would expect measurements to lie within one standard error 68% of the time (for large N). Thus the observed agreement of the data with the fit is quite reasonable.

The temperature profile across the arcjet exit plane is plotted in Figure 13 for the 900 W case. There is a relatively small variation in temperature across the exit plane, ranging from 750 to 1120 K. The asymmetry that was apparent in the raw data is also evident here, with the peak temperature located at $z = -2$ mm, rather than along the centerline as expected. The asymmetry appears again in the density profile shown in Figure 14, except that the peak density is located at $z = +2$ mm. The shape is more peaked than for temperature, with the maximum density slightly more than double the minimum.

The temperature profiles measured at the 5 power levels are plotted in Figure 15. Similar asymmetries are evident to varying degrees in all cases. The maximum temperature always occurs at either $z = -2$ or $z = -4$ mm. The temperatures generally rise across the entire exit plane as the power is increased. This behavior is illustrated in Figure 16, where the maximum measured

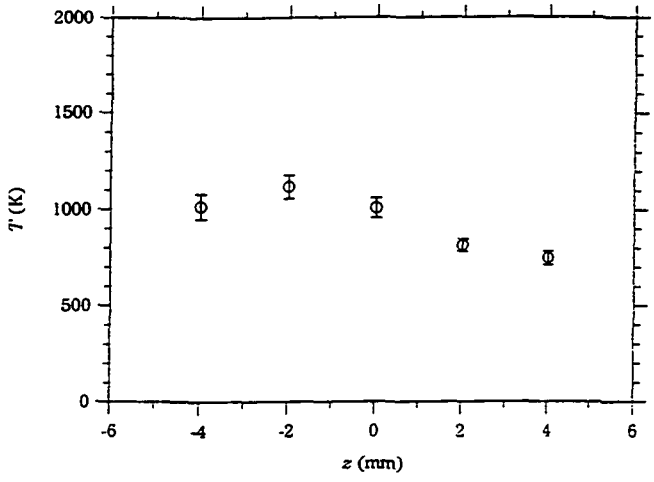

Figure 13 Rotational temperature versus radial position for the 900 W power level.

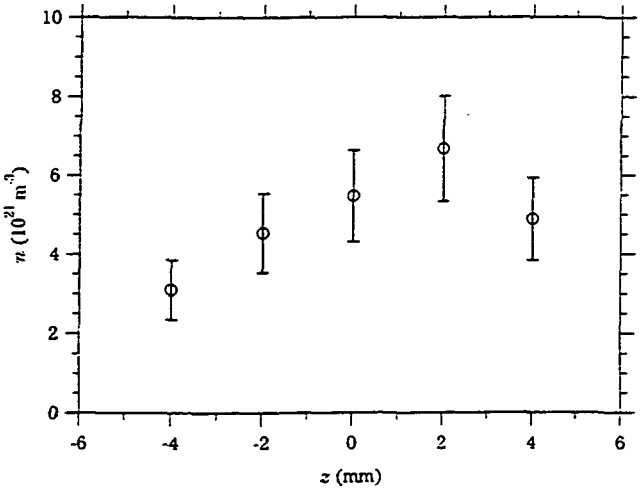

Figure 14 H_2 density versus radial position for the 900 W power level.

temperature is plotted as a function on arcjet power. The maximum temperature was chosen instead of the centerline temperature in order to allow a consistent quantity to be compared between profiles of varying shape. The results range from T_{max} = 960 K at 800 W to 1850 K at 1400 W, with a relatively smooth upward trend associated with increasing power.

The corresponding density profiles are plotted in Figure 17. Again, the profiles were all asymmetric, with the maximum density at z = +2 mm except for the 800 W power level. The densities range from 2.8×10^{21} to 8.8×10^{21} m^{-3}, all below the predicted value of 9×10^{21} m^{-3}. This difference is not surprising, since that prediction was based on the assumption that the exhaust was 100% H_2 at a uniform velocity.

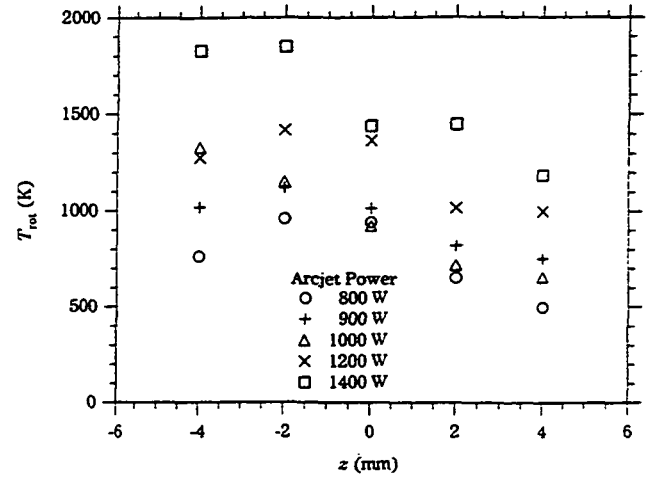

Figure 15 Rotational temperature versus radial positions for 5 power levels.

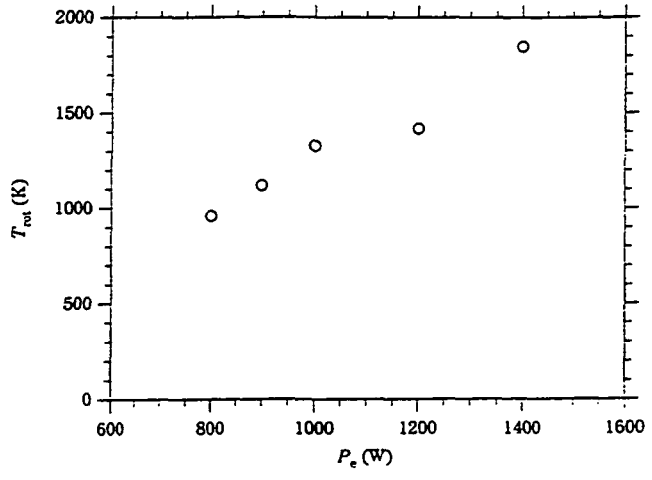

Figure 16 Maximum rotational temperature versus arcjet power level.

Discussion

The H_2 rotational temperatures were compared to previous experimental results. The H translational temperature was previously measured on the same facility using LIF and emission of the Balmer α line. In the LIF study (Liebeskind et al. 1993), the mass flow rate was reported as 13.7 mg s^{-1} (versus 13.3 mg s^{-1} here) and the power levels were 870, 1000, and 1500 W. This LIF data was re-analyzed to account for Stark broadening (Storm and Cappelli 1995) and the resulting temperatures are significantly lower than the originally published data. The emission spectra were collected with a flow of 13.3 mg s^{-1} and P = 1500 W, and were Abel inverted to give spatially resolved data. Figure 18 shows a comparison of the exit plane temperatures from Raman (1400 W), LIF (1500 W), and emission. The re-analyzed LIF results show the most peaked temperature distribution, reaching a maximum of 3400 K on axis, and in agreement with

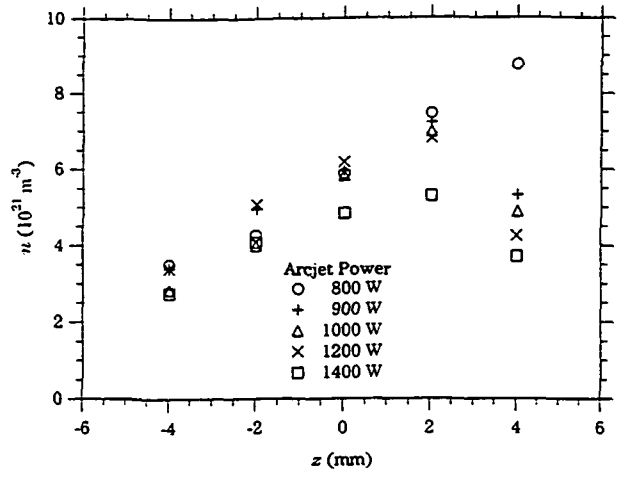

Figure 17 Density versus radial positions for 5 power levels.

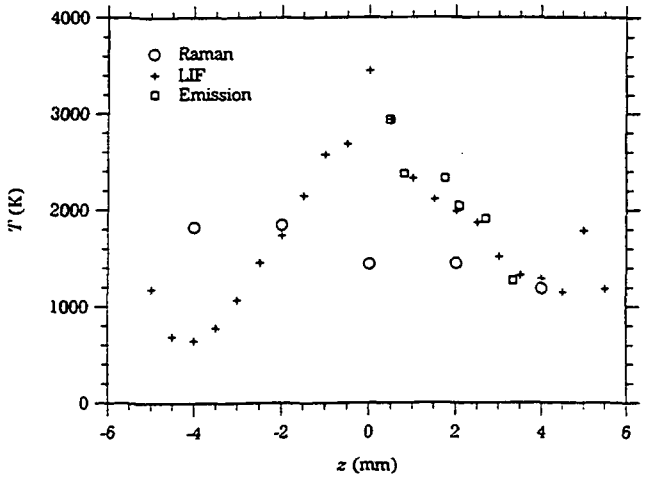

Figure 18 Comparison of temperature versus radial position from Raman scattering, LIF, and emission for $P \approx 1500$ W.

the more recent emission measurements of temperature. The Raman temperatures are the lowest of all, except near the edges, where all methods give similar values. However, the Raman temperatures are consistent with the absorption measurements of Pollard (1993) which gave T_{rot} = 1500 K averaged across the exit plane.

These temperature measurements suggest the arc-ignited flow is not in rotational-translational equilibrium. This result is not entirely unexpected, since the cold-flow also showed significant rotational non-equilibrium. At the higher temperatures in the arc-ignited case, the rotational collisional number Z_{rot} decreases which should bring the flow closer to equilibrium. However, the density is roughly an order of magnitude lower, which will have a counteracting effect by reducing the number of collisions. The lower rotational temperatures can potentially be explained by considering whether H_2 should be in rotational equilibrium as it diffuses to the centre. The number of collisions an H_2 molecule would undergo while moving from the nozzle wall to the center is proportional to Kn^{-1}. The mean-free path was estimated for H_2 in H_2 (since the flow is predominantly H_2) using the tabulated value at room temperature and scaling as n^{-1}. At the throat $\lambda \approx 0.6$ μm, so $Kn^{-1} \approx 500$. Since $Z_{rot} \approx 60$ at 2000 K, then $Kn^{-1} \gg Z_{rot}$ and the flow is likely near rotational equilibrium. However, at the exit plane $\lambda \approx 500$ μm and $Kn^{-1} \approx 10$, so $Kn^{-1} \ll Z_{rot}$. Hence near the exit plane the density is sufficiently reduced that H_2 molecules could be transported to the center without undergoing enough collisions to maintain rotational-translational equilibrium. Molecules colliding with the wall are expected to equilibrate at the wall temperature which has been estimated as ~1700 K (Butler et al. 1994). Hence the walls provide a source of H_2 with a rotational temperature comparable to that measured in the flow.

Summary

Raman scattering measurements of H_2 density and temperature were made at the exit plane of a 1 kW-class hydrogen arcjet thruster. Unlike in the cold-flow studies reported previously, pulsed-laser excitation was used in this study to improve the SNR in this high-background environment. Quantum-limited detection was achieved through the use of gated photon counting and a high-power Nd:YAG laser. Radial profiles of rotational temperature and density at the exit plane were measured for 5 power levels. In all cases the profiles were asymmetric about the arcjet centerline. The temperature profiles were compared with the translational temperatures of H from LIF studies and the bulk temperature from continuum simulations. The rotational temperatures were significantly lower than the other results, implying the flow is not in translational-rotational equilibrium. This finding is not so surprising, since results from the cold-flow studies and simple calculations indicate that rotational equilibrium is unlikely under cold-flow conditions. These results also suggest that the predictive capabilities of numerical simulations of such flows would be enhanced by incorporating a rotational energy transfer mechanism.

Acknowledgements

This research was supported by the Air Force Office of Scientific Research, with partial support from the Olin Aerospace Company and Norton Company. We would also like to acknowledge the NASA Lewis Research Center for providing the arcjet and power processing unit.

References

Beattie, D.R. "Raman scattering measurements of molecular hydrogen in an arcjet thruster plume." Ph.D. Thesis, Mechanical Engineering Department, Stanford University, 1995.

Beattie, D.R. and M.A. Cappelli. "Molecular hydrogen Raman scattering in a low power arcjet thruster." AIAA Paper, 28th AIAA/SAE/ASME/ASEE Joint Propulsion Conference, July 1992.

Boyd I.D., D.R. Beattie, and M.A. Cappelli. "Numerical and experimental investigations of low-density supersonic jets of hydrogen." *Journal of Fluid Mechanics*, **V 280**, P 41-67, 1994.

Butler G.W., A.E. Kull, and D.Q. King. "Single fluid simulations of low power hydrogen arcjets." AIAA Paper 94-2870, 30th AIAA/ASME/SQE/ASEE Joint Propulsion Conference, June 1994a.

Ford A.L. and J.C. Browne. "Rayleigh and Raman Cross Sections for the hydrogen molecule." *Atomic Data*, **V 5**, P 305, 1973.

Jennings D.E., L.A. Rahn, and A. Owyoung. "Laboratory measurement of the S(9) pure rotation frequency." *Astrophysical Journal*, **V 291**, L 15-L 18, 1985.

Liebeskind J.G., R.K. Hanson, and M.A. Cappelli. "Laser-induced fluorescence diagnostic for temperature and velocity measurements in a hydrogen arcjet plume." *Applied Optics*, **V 32**, P 6117-6127, 1993.

Manzella D.H. and M.A. Cappelli. "Vacuum ultraviolet absorption measurements in a hydrogen arcjet." AIAA Paper 92-3564, 28th AIAA/SAE/ASME/ASEE Joint Propulsion Conference, July 1992.

Miller, S. and M. Martinez-Sanchez. "Non-equilibrium numerical simulation of radiation-cooled arcjet thrusters." Paper IEPC 93-218, 23rd International Electric Propulsion Conference. September 1993.

Pobst, J., I. Wysong, and R. Spores,. "Laser induced fluorescence of ground state hydrogen atoms in an arcjet plume." Paper AIAA-95-1973, 26th Plasmadynamics and Lasers Conference, June 1995.

Pollard, J.E. "Arcjet diagnostics by XUV absorption spectroscopy." AIAA Paper 92-2966, 23rd AIAA Plasma Dynamics and Lasers Conference. July 1992.

Pollard, J.E. "Arcjet plume studies using molecular beam mass spectrometry." Paper IEPC 93-132, 23rd International Electric Propulsion Conference. September 1993.

Rahn L.A., R.L. Farrow, and G.J. Rosasco. "Measurement of the self-broadening of the H_2 Q(0-5) Raman transitions from 295 K to 1000 K." *Physical Review A*, **V 43**, N 11, P 6075-6088, 1991.

Storm P.V. and M.A. Cappelli. Private communication, 1994.

Veirs D.K. and G.M. Rosenblatt. "Raman line positions in molecular hydrogen: H_2, HD, HT, D_2, DT and T_2." *Journal of Molecular Spectroscopy*, **V 121**, P 401-419, 1987.

Weber, A. "High resolution Raman studies of gases." *The Raman Effect: Vol. 2*, edited by A. Anderson. Marcel Dekker, New York, 1973.

Wolniewicz, L. "The $X^1\Sigma_g^+$ state vibration-rotational energies of the H_2, HD, and D_2 molecules." *Journal of Chemical Physics*, **V 78**, P 6173-6181, 1983.